Master's thesis

NTNU
Norwegian University of Science and Technology
Faculty of Information Technology and Electrical Engineering
Department of Engineering Cybernetics

Lars C. M. van der Lee

Online Tyre Parameter Estimation for a 4WD Formula Student Racecar

Master's thesis in Cybernetics and Robotics
Supervisor: Ole Morten Aamo
May 2021

(C)FSG - Jonas Haertl.

NTNU
Norwegian University of Science and Technology

NTNU revolve

Lars C. M. van der Lee

Online Tyre Parameter Estimation for a 4WD Formula Student Racecar

Master's thesis in Cybernetics and Robotics
Supervisor: Ole Morten Aamo
May 2021

Norwegian University of Science and Technology
Faculty of Information Technology and Electrical Engineering
Department of Engineering Cybernetics

NTNU
Norwegian University of
Science and Technology

Abstract

The tyres of a racing car are one of it's most important parts. As all forces that accelerate the car have to be induced in the tyre contact patch, extensive knowledge of the tyre's performance is key to maximise performance. Models for tyre performance have been extensively researched, and are able to accurately describe the tyre behaviour. The properties of a tyre, used in tyre models, are highly dependent on external factors like the road surface, tyre and tarmac temperature, tyre compound, weather conditions and tyre wear. These parameters vary from day to day, and can even change over the course of a race. Therefor, an online estimation scheme for the tyre parameters was developed.

The equations of motion for the race car are derived, and were used to implement a Kalman Filter. The Kalman Filter estimates the longitudinal and lateral tyre forces using measurements from the motor encoders and INS. The longitudinal tyre force estimates are then used to estimate the parameters for two tyre models. The chosen tyre models are the brush tyre model and the magic formula tyre model. They have different amount of parameters, and are based on different simplifications. In order to ensure that the estimation scheme was excited enough, an online data selection algorithm was designed.

The results show that both tyre models were able to identify the friction coefficient, with the magic formula being the most accurate, during straight line acceleration and braking. The friction coefficient was underestimated during experiments where combined tyre behaviour is present, as the implemented tyre models only model pure longitudinal forces. The online estimator proved to be able to accurately identify the full tyre models when run during a straight line acceleration experiment.

Sammendrag

Dekkene til en racerbil er en av dens viktigste deler. Siden alle kreftene som akselererer bilen virker i dekkets kontaktflate med asfalten, er kunnskap om dekkets ytelse essentiell for å maskimere bilens ytelse. Modeller for dekk-krefter har blitt mye forsket på, og er egnet til å nøyaktig beskrive dekkets oppførsel. Dekkets parametere, som inngår i modellene, er avhengig av eksterne faktorer som veioverflaten, temperatur på asfalten og dekket, dekkets sammenstilling værforhold og dekkslitasje. Disse parametere kan variere fra dag til dag, og kan til og med endre seg under en Formula Student konkurranse. Derfor har en online estimator for dekkparametere blitt utviklet.

Bevegelseslikningnene for en racerbil har blitt brukt for implementasjonen av et Kalman Filter. Filteret estimerer både longitudinelle og laterale krefter fra dekket, ved hjelp av målinger fra motorens enkodere og INS'en. Estimerte longitudinale krefter er så brukt til å estimere parametere for to rent longitudinelle dekkmodeller. De valgte dekkmodeller er en brush modell og en magic formula modell, som har forskjellige forenklinger og antall parametere. For å forsikre seg om at estimatoren blir ekstitert tilstrekkelig har en online dataseleksjonsalgoritme blitt utviklet.

Resultatene viser at begge dekkmodellene klarer å identifisere friksjonskoeffisienten, der magic formula modellen presterer best, under et eksperiment der bilen akselererer og bremser i en rett linje. I scenarioer der bilen opplever kombinerte longitudinelle og laterale krefter i dekkene blir friksjonskoeffisienten underestimert fordi modellene kun inkluderer longitudinell oppførsel. I tillegg viser resultatene at den online estimatoren klarer å nøyaktig identifisere parametere for en full longitudinell dekkmodel under kjøring på rette strekker.

Preface

This thesis marks the end of six years at NTNU, of which three as a member of Revolve NTNU. The experience I have built up during my period at Revolve NTNU has been invaluable. I have developed myself a lot, both technical and on the personal plane during these years. I would like to thank the NTNU administration, at the IE and IV faculties and MTP and ITK institutes, for supporting Revolve NTNU, and providing me with an arena where my practical engineering can be challenged! A special thanks goes to Per Schjølberg, for his immense dedication to always helping and promoting Revolve NTNU, wherever he goes! Revolve NTNU has enabled me to chase my motorsport dreams, and to work with a group of highly motivated and skilled team members, who always push each other to the limit! I would like to thank everyone involved at Revolve NTNU, especially Team 2019, 2020 and 2021 for their support, during highs and lows, when winning and when losing.

I would also like to thank my supervisor Ole Morten Aamo, and team mate and good friend Marius Hamre Nordrik for the weekly meetings, where we had fruitful discussion and got to exchange many ideas for the work presented in this thesis!

At last, but not least, I would like to thank family and friends for all support. Especially my parents, who are always there to listen to my stories, whether they are good or bad, are about life, school or Revolve.

Lars C. M. van der Lee

Trondheim, May 31, 2021

Contents

List of Tables

List of Figures

Nomenclature

Tyres

α	Tyre slip angle	rad
δ	Wheel angle, relative to vehicle x-axis	rad
κ	Tyre slip ratio	$\%$
μ	Tyre-road friction coefficient	$-$
ω	Tyre rotational velocity	rad/s
F_x	Longitudinal tyre force, acting on the road surface	N
F_y	Lateral tyre force, acting on the road surface	N
F_z	Vertical tyre force, also called the normal load.	N
I_z	Inertia around the vertical axis	$kg \cdot m^2$
I_ω	Inertia around the rotational axis	$kg \cdot m^2$
i_{gear}	Gear ratio	$-$
M_b	Applied braking torque	Nm
M_m	Applied motor torque	Nm
M_R	Torque from rolling-resistance	Nm
R_e	Effective tyre radius	m
R_l	Loaded tyre radius	m

R_u	Unloaded tyre radius	m
$v_{x_{wheel}}$	Longitudinal velocity in tyre frame	m/s
$v_{y_{wheel}}$	Lateral velocity in tyre frame	m/s

Vehicle

ψ	Yaw angle	rad
a_x	Longitudinal acceleration	m/s^2
a_y	Lateral acceleration	m/s^2
A_{ref}	Frontal area	m^2
C_d	Drag coefficient	$-$
C_l	Lift coefficient	$-$
F_d	Aerodynamic drag force	N
F_l	Aerodynamic lift force	N
h_{cg}	Height of center of gravity	m
I_z	Inertia around the vertical axis	$kg \cdot m^2$
l_f/l_r	Vehicle wheelbase front/rear. Distance from wheel axle to center of gravity.	m
m	Mass	kg
r	Yaw rate	rad/s
t_f/t_r	Vehicle track (Distance between wheel centers) on the front and rear axle	m
v_x	Longitudinal velocity	m/s
v_y	Lateral velocity	m/s

Acronyms

4WD Four-wheel drive. 6, 13

CAN Controller Area Network. 45

FWD Front-wheel drive. 6

HIL Hardware-in-the-loop. 44, 45

LTI Linear time-invariant. 31

MF Magic Formula. xii, 2, 22

PCB Printed Circuit Board. 44, 45

QP Quadratic Programming. 4

TV Torque Vectoring. 2, 4, 5, 30, 38, 41, 44, 45, 64, 81

VCU Vehicle Control Unit. 44, 45

Chapter 1

Introduction

1.1 Background

This thesis is written in cooperation with Revolve NTNU, a Formula Student team. Every year, a new prototype single-seater race car is designed, manufactured, assembled, tested, and raced against student teams from universities around the world. Revolve NTNU's vision is to educate world class engineers, by developing high performance race cars.

The tyres of a race car are one of the most important systems on the car. The tyres are the only interaction between the car and the track, that can accelerate the car. All of the available acceleration forces have to go through the tyres, therefore extensive knowledge about the tyre behaviour is key to a high performing race car.

Figure 1.1: NOVA, the 2019 Revolve NTNU race car, used for simulations in this thesis

1.2 Motivation

Revolve NTNU's race cars are equipped with an electrical powertrain, consisting of four hub-mounted motors. The individual control of the motor output on each wheel opened the door for implementation of a Torque Vectoring (TV) control system. The controller aims to utilize all available tyre grip for each wheel. The latest generation of TV has used tyre models supplied from the tyre manufacturer, to estimate the available grip and optimal motor output. These tyre models are modeled from test data on tyre testing machines, often called flat track test-beds. This season Revolve NTNU seeks to improve the performance of the next race car by switching to a new tyre. The switch to a new tyre will require a new approach to the estimation of available tyre grip, as there is no tyre model available. Using a simplified version of the semi-empirical Magic Formula (MF) tyre model, we want to estimate the model parameters online, using the sensors available on the 2021 race car. By switching from a pre-fitted tyre model, to a model that is estimated online, we want to allow the car to better react to changing road surfaces. The interaction between the tyre compound and the road varies on several factors that pre-fitted models are unable to adapt to. These factors include, but are not limited to:

- Road surface roughness and temperature
- Tyre temperature and wear
- Ambient temperature
- Weather conditions and precipitation
- Suspension setup

Figure 1.2: The Continental tyres used by Revolve NTNU, and their replacement Hoosier tyre

1.3 Thesis outline

This thesis consists of 9 chapters. The first chapter give a short introduction to the motivation behind the thesis, the state of the art and the status of the task after the work performed in the project thesis preceding this thesis. Chapter 2 contains relevant theory for the thesis, while Chapters 3, 4 and 5 cover the design and implementation of the Kalman filter and estimation scheme. The testing and simulation setup is explained in Chapter 6. The results of the Kalman filter are presented and discussed in Chapter 7, while the online parameter estimation results are presented and discussed in Chapter 8. A final conclusion is presented in Chapter 9, along with suggestions for future work.

1.4 System overview

The estimation scheme that will be developed for this thesis aims to improve the performance of the torque vectoring control system in Revolve NTNU. This is an already complex system, that finds optimal motor setpoints that attempt to utilize the available tyre grip and provide the driver with a predictable vehicle behaviour. This section will introduce the systems closest to the torque vectoring to provide context.

1.4.1 Race car

Revolve NTNU's race cars are built to compete in the Formula Student competitions. The race car used as a basis for the simulations in this thesis was built in the 2019 season, called NOVA. It weighs 162.5 kg, features a full aerodynamic package. Both the aerodynamics, suspension arms, rims and chassis are made of carbon fiber to reduce weight. Every wheel is equipped with a planetary gearbox with a gear ratio of $i_{gear} = 14.38$ and a hub mounted motor, driven by four in-house developed inverters. The control system that provide the setpoints for the inverters is a torque vectoring algorithm. The data flow, from sensors to motor output is shown in Figure 1.3. A short introduction to the state estimation and torque distribution modules is given in this section

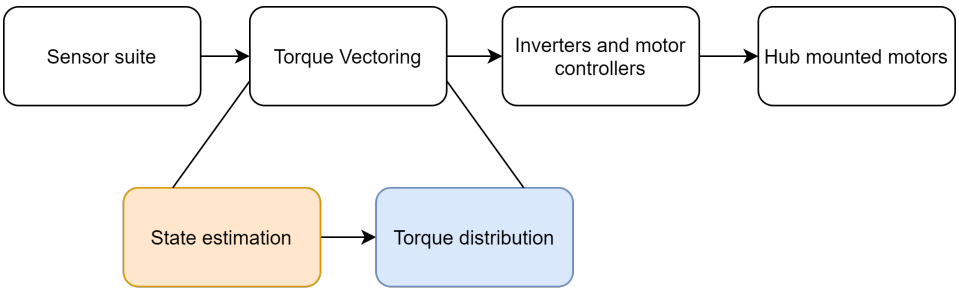

Figure 1.3: System overview

1.4.2 Torque vectoring

The four hub-mounted motors are controlled by the torque vectoring algorithm. The goal of the TV algorithm is to find the optimal torque setpoints for each motor to achieve the acceleration requested by the driver, and maintain a neutrally steered behaviour. The control system consists of two modules: State estimation and torque distribution.

1.4.2.1 State estimation

The state estimation module uses the available sensor measurements to estimate the conditions the tyres are experiencing. As the motors output act on the ground through the tyres, it is important to understand the state the tyres are in to set the optimal motor output. There are three parameters that are especially important, tyre load and longitudinal and lateral tyre slip. These are used by the torque vectoring system to find optimal setpoints.

Tyre load

The maximum force a racing tyre can exert on the ground is limited by the normal load on the tyre. The tyre load is dependent on the vehicle acceleration, velocity and mass due to load transfer, aerodynamics and gravity respectively.

Tyre slip

The rubber compound of the tyre is stretched and compressed during driving. This is the source of the force exerted by the tyres. The stretching is quantified by the state estimation module, and is referred to as tyre slip. For longitudinal forces, the slip is called the slip-ratio, while lateral forces are generated by the tyre slip angle.

1.4.2.2 Torque distribution

The output of the state estimation module is used to find the optimal torque setpoints for the motors. This is done with a Quadratic Programming (QP) optimisation problem. The driver input from the steering wheel and pedals are used to generate references for the vehicle behaviour. The pedal input is used to determine the total force in the longitudinal direction, while the steering wheel input is used to determine the request moment around the vehicle z-axis.

Tyre limit constraints

The QP problem has linear constraints that are related to the estimated tyre state. The estimated tyre load, combined with the friction coefficient between the tyre and the road surface make up the maximum force possible to be generated by the tyre. In order to prevent overloading the tyre, the torque cannot lead to a force above the limit. The tyre-road friction coefficient is dependent on the tyre and track conditions, and can vary from day to day or even over the course of a race. Therefor this thesis aims to estimate the friction coefficient online, to ensure the TV algorithm always can operate at peak performance.

1.4.3 Racing track

Revolve NTNU designs race cars that will compete in Formula Student competitions. The tracks are marked with cones on either side of the road, and are laid out on open tarmac areas. This makes for tight, twisty tracks, with lots of corners and few straight sections. The average track width is around three meters, meaning that even small errors can cause cones to be hit. Hitting a cones will be punished with a 2 second penalty, which rules out a top position immediately.

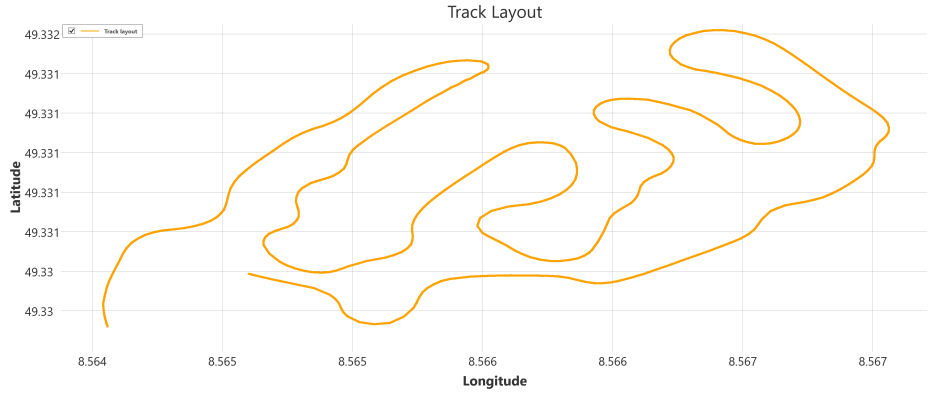

Figure 1.4: Track layout at Formula Student Germany

1.4.3.1 Tarmac conditions

The tracks can be laid out on everything from empty parking lots to actual racetrack sections meaning that the track surface varies a lot throughout the season. The tyre-road friction will vary between all tracks, based on track temperature, tarmac roughness, rubber from cars that have driven over it and precipitation. If not found online, the friction coefficient used to find the tyre limits needs to be adjusted to each track, taking valuable time.

1.5 Goal and scope

This thesis has one primary goal, and a secondary goal. The primary goal is to design and implement an online estimation scheme that can estimate the friction coefficient between the tyre and road surface during racing conditions. The friction estimate is important for the TV control system, as it is a constraint for the motor output, that prevents wheel-spin.

The secondary goal is a system identification goal for the tyre itself. Tyre models are an important tool when designing a race car, and an accurate tyre model is very useful for the design of future Revolve NTNU race cars. So in addition to the estimate of the friction coefficient, the remaining tyre model parameters will also be estimated.

The state estimation of tyre loads and slips are not a part of this thesis. Previously imple-

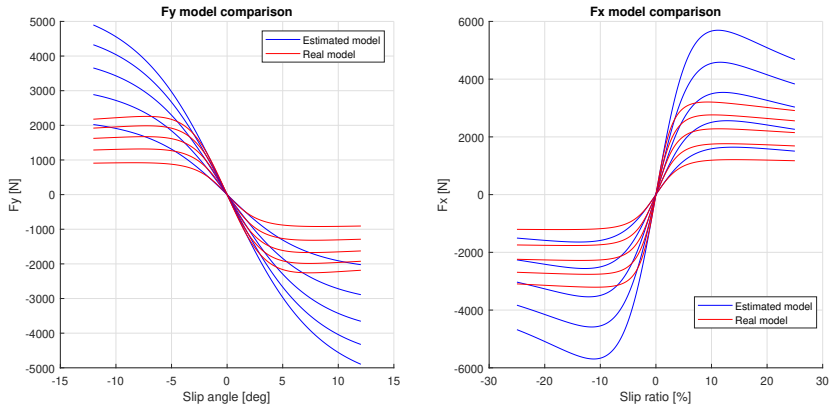

Figure 1.5: Estimated vs. true model from Project Thesis [12]

mented schemes for the estimation of these states have been developed by Revolve NTNU, and they are used for results presented in Chapter 7. Their limitations will be explained in Chapter 5, to give an insight in their performance and how that can influence the results for this thesis.

1.6 Literature review

This thesis is a continuation of the work presented in the Project Thesis [12]. A gradient descent method was implemented, that aimed to minimise the difference between INS measurements of lateral and longitudinal acceleration and a theoretical sum of forces, expressed with a simplified tyre model. The presented results failed to give an accurate estimate of the tyre-road friction, in addition to a poor estimate of the tyre model. A lack of model excitation, and a gradient with a high complexity were identified as two causes for the inaccuracy. The estimated tyre model, and the true model are shown in Figure 1.5. None of the two goals were achieved with great success. The friction coefficient was overestimated with a factor of 2, while the final model shape also failed to match the actual tyremodel.

Even though the goal is to identify the friction coefficient and model parameters for the longitudinal tyre forces, the approach taken in the project thesis[12] required an estimation scheme for the lateral forces as well, because the full vehicle dynamics were incorporated into the cost function. Since the vehicle dynamics are known, these could be used to simplify the optimisation problem, and focus fully on the longitudinal dynamics. An approach where the dynamics are used to design a Kalman Filter is presented by Choi et. al [8]. The method was applied to a FWD vehicle, and estimated the longitudinal tyre forces for each wheel with great success. The method will need to be adjusted to account for the 4WD properties of the Revolve NTNU race car. The Kalman Filter will provide an estimate of the longitudinal tyre forces, meaning that these can be used directly in the simplified cost

function of the optimisation problem: $(F_x - \hat{F}_x(\theta))^2$.

Another issues discovered in the project thesis was the lack of system excitation during regular driving. Most existing friction estimation schemes described in the literature use a predefined sequence to ensure the model is excited enough. [8], [13] As the goal of this thesis is to develop a scheme that can be used during a race, where the track mandates the driver input, a solution that ensures excitation has to be designed.

There are several approaches to solving the optimisation problem. Midtskogen[10] and the project thesis[12] both utilised a gradient descent method. This is a rather simple solver, which has no stability or convergence guarantees. However, the non-linear nature of the problem, combined with it's highly non-convex cost function landscape means there are no simple estimation schemes that can ensure convergence. Choi et. al presented the use of a linearised recursive least squares solver[8]. An attempt to implement this solver was made for this thesis, but was discarded as it proved to be hard to get parameter convergence. As the gradient descent method proved to be able to converge, given that it is tuned carefully, this solver will be used for this thesis as well.

Chapter 2

Theory

2.1 Notation

The vehicle described in this thesis has two axles, with two tyres each. To increase readability, these are abbreviated to two letter combinations. The abbreviations are shown in Table 2.1.

Axle/Tyre	Abbreviation
Front axle	f
Rear axle	r
Front left tyre	FL
Front right tyre	FR
Rear left tyre	RL
Rear right tyre	RR

Table 2.1: Axle and tyre abbreviations

When specific forces, slips or angles are referred to for a single tyre, they will use the format specified in Equation 2.1, using the longitudinal tyre force for the rear left tyre as an example.

$$F_{x_{RL}} \tag{2.1}$$

2.2 Vehicle Dynamics Fundamentals

The Kalman Filter designed in this thesis and the tyre estimator have been developed using equations from Vehicle Dynamics. This field of study aims to describe the dynamics of

cars. This ranges everything from aerodynamic forces acting on the vehicle, to forces generated by tyres and rotational dynamics of entire vehicles. The following section will give a short introduction to the parts of vehicle dynamics that are relevant for this thesis.

2.2.1 Load transfer

This section is adapted from project thesis

During operation, a race car experiences longitudinal and lateral acceleration. These develop reactionary forces in the form of a centrifugal force in the lateral direction and inertial force in the longitudinal direction. This changes the distribution of the vehicle weight over the four tyres causing the F_z of each tyre to change [2, Chapter 18].

2.2.1.1 Lateral load transfer

In a steady-state turn, the outer wheels get an increased load. We can derive the equation for load transfer by taking the moments around the outer wheel's contact patch. For simplification, we assume a 50/50 weight balance, meaning we can merge the four wheels to one axle as seen in Figure 2.1. The centrifugal force F is defined as $m \cdot a_y$.

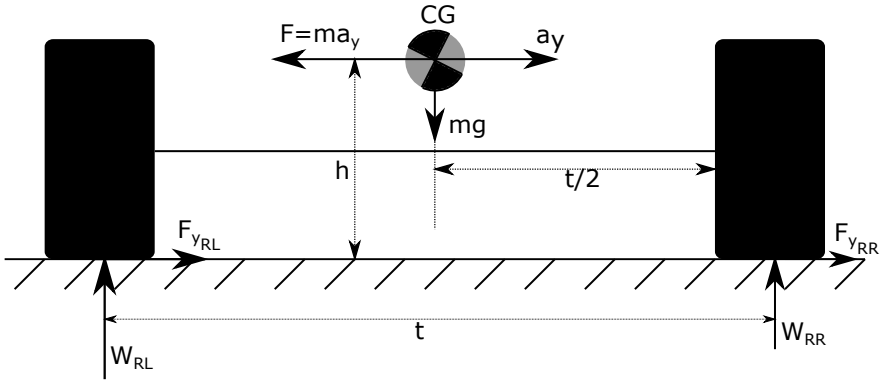

Figure 2.1: Free body diagram in steady state cornering, seen from the rear.

Taking the moments about the inner wheel, in this case the right, we get Equation 2.2.[2, Chapter 18]

$$W_{RL} \cdot t = mg \cdot \frac{t}{2} + ma_y \cdot h \tag{2.2a}$$

$$W_{RL} = \frac{mg}{2} + \frac{ma_y \cdot h}{t} \tag{2.2b}$$

$$\Delta W_{RL} = \frac{ma_y \cdot h}{t} \tag{2.2c}$$

Where h is the height of the center of gravity, and t is the vehicle's track width.

2.2.1.2 Longitudinal load transfer

In a steady-state acceleration, the rear wheels get an increased load. Using the diagram in Figure 2.2, the equation for load transfer is derived by taking the moments around the front wheel's contact patch. For simplification, we assume a 50/50 weight balance, meaning we can use half the wheelbase in our calculations, $\frac{l}{2} = l_f = l_r$. The force F, causing the load transfer is defined as $m \cdot a_x$, giving us Equation 2.3 for steady-state longitudinal load transfer [2, Chapter 18]. In a braking scenario, the same equation can be used, with a negative sign on a_x. In this case, the load on the front tyres will increase.

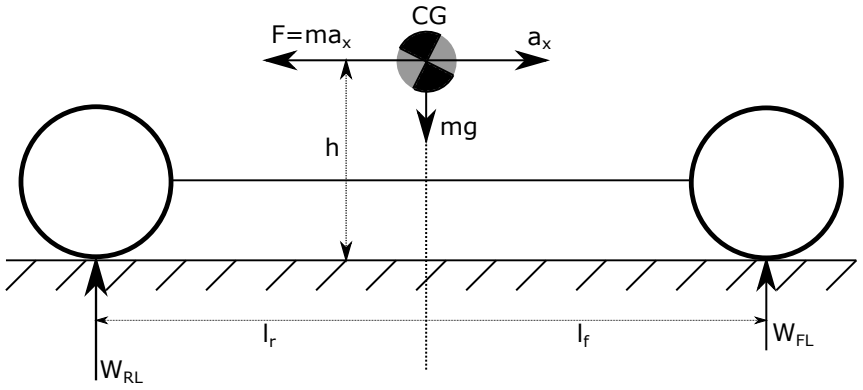

Figure 2.2: Free body diagram in steady state longitudinal acceleration, seen from the side.

Taking the moments about the front wheel, we get Equation 2.3 [2, Chapter 18].

$$W_{RL} \cdot l = mg \cdot \frac{l}{2} + ma_x \cdot h \tag{2.3a}$$

$$W_{RL} = \frac{mg}{2} + \frac{ma_x \cdot h}{l} \tag{2.3b}$$

$$\Delta W_{RL} = \frac{ma_x \cdot h}{l} \tag{2.3c}$$

Where h is the height of the center of gravity, and l is the vehicle's wheelbase.

2.2.2 Aerodynamics

This section is adapted from project thesis

The race car is equipped with an aerodynamic package. This is a combination of aerofoils and flow-manipulating devices that manipulate the air flowing over the vehicle body and around the tyres to generate as much downforce as possible, with as little drag as possible. The aerodynamic force is decomposed into drag and downforce. The drag is an unwanted

effect generated by the chassis, wheels and aerodynamics disturb the flow around the vehicle, slowing down the car. The downforce is generated by a pressure difference between the top and bottom surface of the wind elements, pressing the car into the road. This additional normal load on the car is distributed between the 4 wheels by the aerodynamic balance. This balance is highly sensitive to the vehicle motion and changes with velocity and orientation. This is due to how the airflow interacts with the foils and the ground effect under the vehicle. The decomposed aerodynamic forces are defined in Equations 2.4 and 2.5. In the vehicle model, they are assumed to be working in one point, on the center axis of the race car.

$$F_d = \frac{1}{2} C_d A_{ref} \rho v_x^2 \tag{2.4}$$

$$F_l = \frac{1}{2} C_l A_{ref} \rho v_x^2 \tag{2.5}$$

2.2.3 Single track vehicle model

The single track model, also referred to as the bicycle model, is a simplified model of a race car. The two wheels on each axle have been approximated with one wheel, where only the front wheel can be steered. Figure 2.3 shows the simplified vehicle model. As only the front wheels can be turned, the rear longitudinal forces have no moment around the center of mass, causing no contribution to the rotational dynamics of the vehicle. The lateral forces still have an arm in the wheelbase of the vehicle.

2.2.3.1 Longitudinal dynamics

As the front wheel can be steered, both the lateral and longitudinal tyre force will contribute to the longitudinal dynamics. On the rear wheel, only the longitudinal tyre force will contribute. This gives the equation of motion in Equation 2.6.

$$\sum F_x = m \cdot a_x = F_{x_f} \cos \delta_f - F_{y_f} \sin \delta_f + F_{x_r} \tag{2.6}$$

2.2.3.2 Lateral dynamics

Just like for the longitudinal dynamics, the front wheel will contribute with both tyre forces, while the rear wheel only contributes with the lateral force. This gives the lateral equation of motion in Equation 2.7.

$$\sum F_y = m \cdot a_y = F_{x_f} \sin \delta_f + F_{y_f} \cos \delta_f + F_{y_r} \tag{2.7}$$

2.2.3.3 Yaw dynamics

The yaw dynamics of the single-track model are given in Equation 2.8, as the equation of motion around the z-axis of the vehicle.

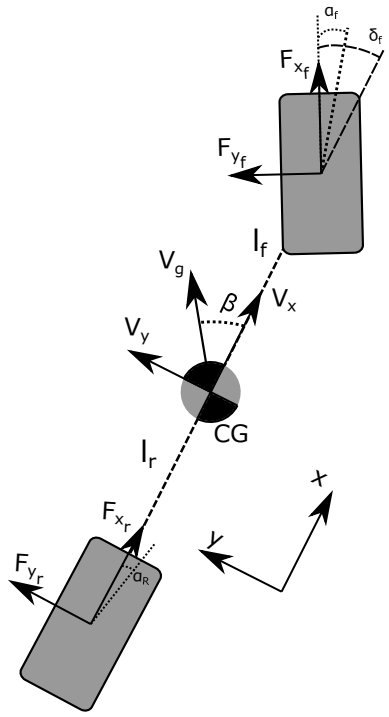

Figure 2.3: Single track vehicle model, with front wheel steering and two driven wheels

$$\sum \tau_z = I_z \cdot \dot{r} = l_f \cdot (F_{x_f} \sin \delta_f + F_{y_f} \cos \delta_f) + l_r \cdot F_{y_r} \tag{2.8}$$

2.2.4 Double track vehicle model

The dynamics of a 4WD vehicle can be modelled using a double track vehicle model, shown in Figure 2.4. This model takes into account the aerodynamic drag, front-wheel steering, and 4 driven wheels. The front wheels have an Ackermann-steering geometry, meaning the wheel angle is not identical for both wheels when they are turned.

Using the balance equations for forces and torques, a mapping from translational and rotational acceleration to tyre forces can be derived in the form of the equations of motion.

2.2.4.1 Longitudinal dynamics

All four tyres contribute with a force in the longitudinal direction of the race car. The rear wheels, directly contribute to the x-direction of the vehicle. The front tyres can be turned, meaning both the x- and y-directional force in the contact patch will contribute. Equation

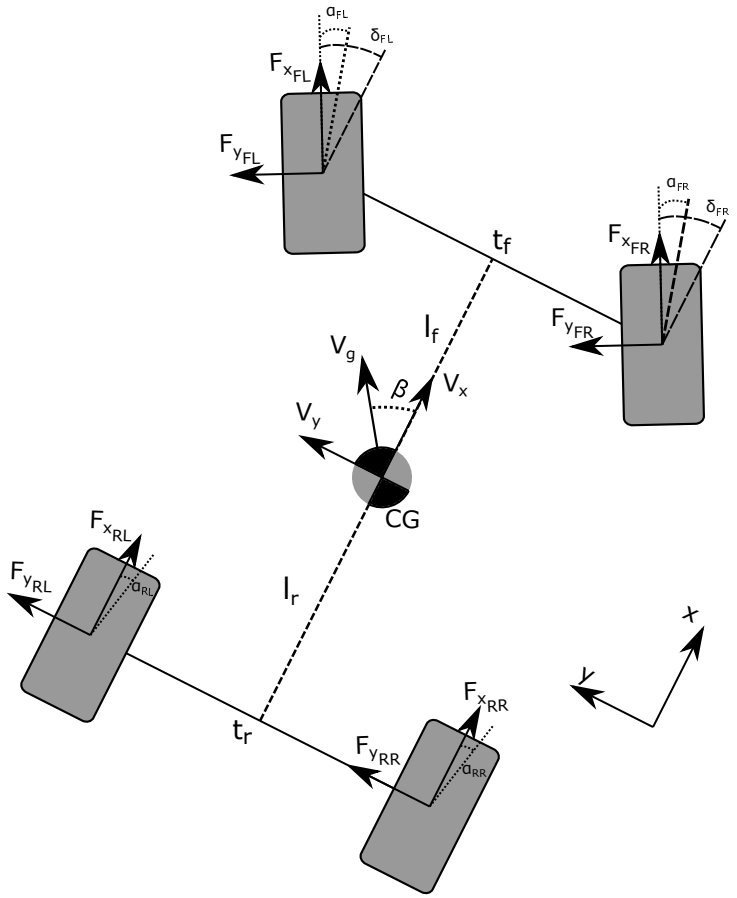

Figure 2.4: Vehicle model with front wheel steering and 4 driven wheels

2.9 shows the equations for the balance of forces in the x-direction.

$$\begin{aligned}\sum F_x = m \cdot a_x = F_{x_{FL}} \cdot \cos\delta_{FL} + F_{x_{FR}} \cdot \cos\delta_{FR} + F_{x_{RL}} + F_{x_{RR}} \\ -F_{y_{FL}} \cdot \sin\delta_{FL} - F_{y_{FR}} \cdot \sin\delta_{FR} - F_d\end{aligned} \tag{2.9}$$

Simplifying with force vectors gives the expression in Equation 2.10, representing the equation of motion in the x-direction.

$$m \cdot a_x + F_d = \boldsymbol{F}_x \cdot \begin{bmatrix}\cos\delta_{FL} \\ \cos\delta_{FR} \\ 1 \\ 1\end{bmatrix} - \boldsymbol{F}_y \cdot \begin{bmatrix}\sin\delta_{FL} \\ \sin\delta_{FR} \\ 0 \\ 0\end{bmatrix} \tag{2.10}$$

2.2.4.2 Lateral dynamics

All four tyres contribute with a force in the lateral direction of the race car. Even though the rear wheels cannot be turned, they will still have a slip angle as the car is turning. The front tyres can be rotated around their z-axis, and when rotated, both the longitudinal and lateral forces generated in the tyre contact patch will contribute to the lateral acceleration off the vehicle.

$$\begin{aligned}\sum F_y = m \cdot a_y = F_{y_{FL}} \cdot \cos\delta_{FL} + F_{y_{FR}} \cdot \cos\delta_{FR} + F_{y_{RL}} + F_{y_{RR}} \\ + F_{x_{FL}} \cdot \sin\delta_{FL} - F_{x_{FR}} \cdot \sin\delta_{FR}\end{aligned} \tag{2.11}$$

Simplifying with force vectors gives the equation of motion in Equation 2.12, which will be used for the Kalman Filter design in Chapter 3.

$$m \cdot a_y = \boldsymbol{F}_x \cdot \begin{bmatrix} \sin\delta_{FL} \\ -\sin\delta_{FR} \\ 0 \\ 0 \end{bmatrix} + \boldsymbol{F}_y \cdot \begin{bmatrix} \cos\delta_{FL} \\ \cos\delta_{FR} \\ 1 \\ 1 \end{bmatrix} \tag{2.12}$$

2.2.4.3 Yaw dynamics

All lateral and longitudinal tyre forces contribute to a moment around the z-axis of the vehicle. The balance equation for the moments around the z-axis can be used to describe the acceleration of the yaw angle of the vehicle.

Equation 2.13 shows the moment of each tyre force around the z-axis.

$$\begin{aligned}\sum \tau_z = I_z\dot{r} = F_{x_{FL}}(-\frac{t_f}{2}\cos\delta_{FL} + l_f\sin\delta_{FL}) + F_{x_{FR}}(\frac{t_f}{2}\cos\delta_{FR} + l_f\sin\delta_{FR}) \\ + \frac{t_r}{2} \cdot (-F_{x_{RL}} + F_{x_{RR}}) \\ + F_{y_{FL}}(l_f\cos\delta_{FL} + \frac{t_f}{2}\sin\delta_{FL}) + F_{y_{FL}}(l_f\cos\delta_{FR} - \frac{t_f}{2}\sin\delta_{FR}) \\ - l_r \cdot (F_{y_{RL}} + F_{y_{RR}})\end{aligned} \tag{2.13}$$

This equation can also be simplified using force vectors for the lateral and longitudinal tyre forces, giving the equation of motion in Equation 2.14.

$$I_z\dot{r} = \boldsymbol{F_x} \begin{bmatrix} (-\frac{t_f}{2}\cos\delta_{FL} + l_f\sin\delta_{FL}) \\ (\frac{t_f}{2}\cos\delta_{FR} + l_f\sin\delta_{FR}) \\ -\frac{t_r}{2} \\ \frac{t_r}{2} \end{bmatrix} + \boldsymbol{F_y} \begin{bmatrix} (l_f\cos\delta_{FL} + \frac{t_f}{2}\sin\delta_{FL}) \\ (l_f\cos\delta_{FR} - \frac{t_f}{2}\sin\delta_{FR}) \\ -l_r \\ -l_r \end{bmatrix} \tag{2.14}$$

2.3 Tyre fundamentals

Besides aerodynamic elements, the four tyres are the only parts of the vehicle that can exert a force on the surrounding. All acceleration, both longitudinal and lateral come from forces generated in the tyre contact patch, the area where the tyre is in contact with the road surface. There are different standards in use regarding the coordinate system for the tyres. This thesis uses the ISO 8855 standard, which defines the axes as shown in Figure 2.5 [18]. The forces in the contact patch do not act exactly in the center of the contact patch, however this assumption has been made for this thesis to reduce model complexity.

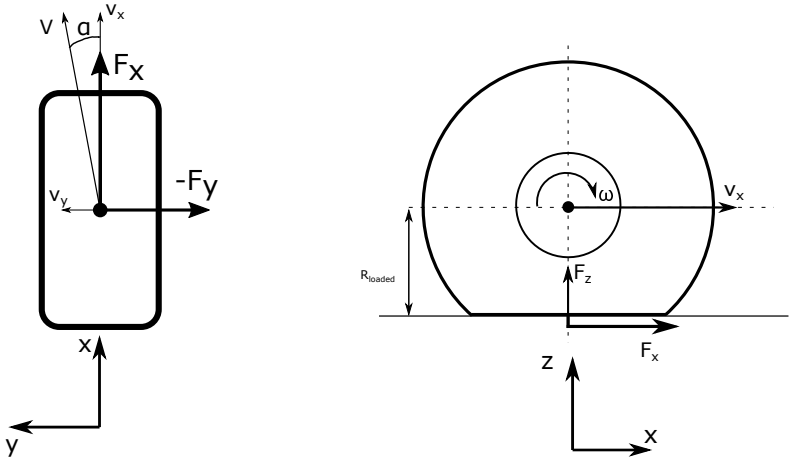

(a) Top-down view of the tyre.

(b) Side view of the tyre.

Figure 2.5: Tyre coordinate system used in thesis.

2.3.1 Tyre slip

As the tyres are operating, they experience compression and stretching of the tyre compound. The manipulation of the rubber generates tyre slip, which is the source of the contact patch forces. Slip can occur both longitudinal, through the application of a motor or braking torque on the wheel, and lateral through steering input.

2.3.1.1 Longitudinal slip

The longitudinal slip is referred to as the slip ratio of a tyre. Like the tyre coordinate system, there is no universally agreed-upon definition, and multiple definitions are used in the automotive industry. In this thesis, the SAE J670 definition is used. The slip ratio can be described as the ratio between the slip velocity, and the angular velocity of a free-rolling wheel with the same longitudinal translation velocity. The slip velocity is defined as $\Omega - \Omega_0$, where Ω is the driver wheel's angular velocity and Ω_0 the angular velocity of a free-rolling wheel. A free-rolling wheel is a wheel without driving- and/or braking torque applied to it. [2, Chapter 2] The free-rolling angular velocity of a tyre is defined in

Equation 2.15, where v is the translational velocity of the tyre and α the tyre slip angle. The slip angle will be discussed in detail in Section 2.3.1.2. [3, Chapter 1]

$$\Omega_0 = \frac{v \cos \alpha}{R_{eff}} \tag{2.15}$$

The effective radius of a tyre, denoted as R_{eff}, is the radius required for the translational velocity and angular velocity for a free-rolling tyre to match. The difference in loaded tyre radius and effective tyre radius originates from the deformation of the tyre in the contact patch. The effective rolling radius lies between the loaded and unloaded radius, as shown in Figure 2.6 [3, Chapter 1].

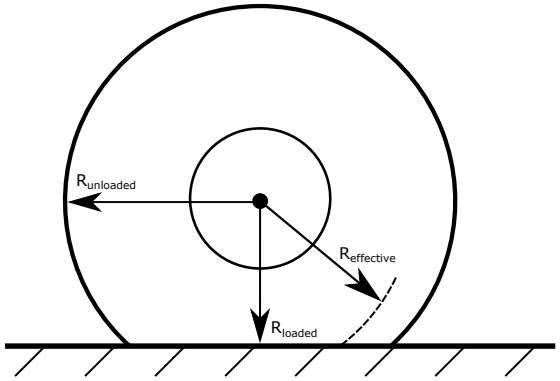

Figure 2.6: Loaded, effective and unloaded tyre radius

The tyre slip ratio is defined as the ratio between the slip velocity and the free-rolling velocity, as in Equation 2.16. Substituting in Equation 2.15 gives us the SAE J670 definition for slip ratio.

$$\kappa = \frac{\Omega - \Omega_0}{\Omega_0} \tag{2.16a}$$

$$\kappa = \frac{\Omega}{\Omega_0} - 1 \tag{2.16b}$$

$$\kappa = \frac{\Omega R_{eff}}{v \cos \alpha} - 1 \tag{2.16c}$$

For a free-rolling tyre, Ω is equal to Ω_0, and κ will be zero. For a situation where the wheel is locked during braking, Ω is zero, and κ will be -1. For a tyre that is in full spin, the slip ratio will be 1. [2, Chapter 2].

2.3.1.2 Lateral slip

The lateral slip of a tyre is referred to as the slip angle. Unlike the definition of slip ratio, the slip angle is more intuitive to understand. Simply explained, the slip angle is the angle

between the tyre heading and tyre velocity vector. This is shown is Figure 2.5 as α. The slip angle is defined in Equation 2.17 [2, Chapter 2].

$$\tan(\alpha) = \frac{v_y}{v_x} \tag{2.17}$$

2.3.2 Tyre forces

There are three main tyre forces acting in the tyre contact patch. The tyre load, originated from the vehicle weight and aerodynamic downforce, and the longitudinal and lateral forces from the tyre slip ratio and angle respectively. These three forces are closely related, and are limited by the magnitudes of each other.

2.3.2.1 Tyre load

The vertical force on the tyre is referred to as F_z, or tyre load. The tyre load limits the total magnitude of the combined longitudinal and lateral forces, as they are both frictional forces. The maximum tyre force, also referred to as grip, is defined in Equation 2.18. [2, Chapter 2]. μ is the friction coefficient between the tyre and the road surface. The tyre load is a dynamic load. In addition to the mass of the vehicle and driver, the tyre load is affected aerodynamic forces pressing the race car down and longitudinal and lateral acceleration as described in Sections 2.2.2 and 2.2.1.

$$F_{max} = \mu F_z \tag{2.18}$$

2.3.2.2 Longitudinal and lateral forces

The longitudinal and lateral forces are bound by the constraint from Equation 2.18. A tyre that is exerting a lateral force, will have a lower maximum longitudinal force, and vice-versa. This is commonly illustrated with a friction ellipse [2], [3]. A friction ellipse is shown in Figure 2.7. The friction ellipse illustrates that the maximum force F, defined as $F = \sqrt{F_x^2 + F_y^2}$ is bounded. It is important to note that the maximum lateral force does not have to be identical to the maximum longitudinal force. This is tyre-dependent, but most tyres have a different friction coefficient in the x- and y-direction.[3]

2.3.3 Rotational dynamics

The wheels are subject to torques from motors, brakes, tyre rolling resistance and the longitudinal tyre forces. Figure 2.8 show the different torques/forces and their respective arms. The rotational dynamics of the wheel are given in Equation 2.19.

$$I_\omega \dot{\omega} = M_m - M_b - R_l F_x - M_R \tag{2.19}$$

The motor torque can be both positive and negative. As the Revolve NTNU race car is equipped with electric motors, kinetic energy recovery is achieved by applying a negative

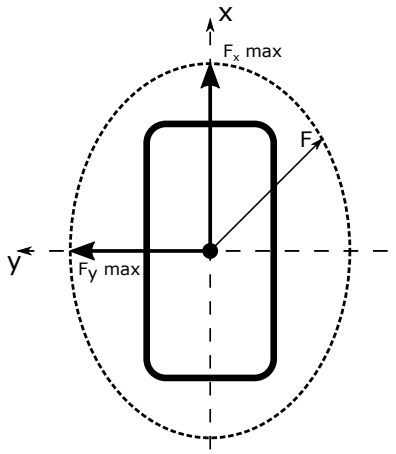

Figure 2.7: Friction ellipse for a tyre

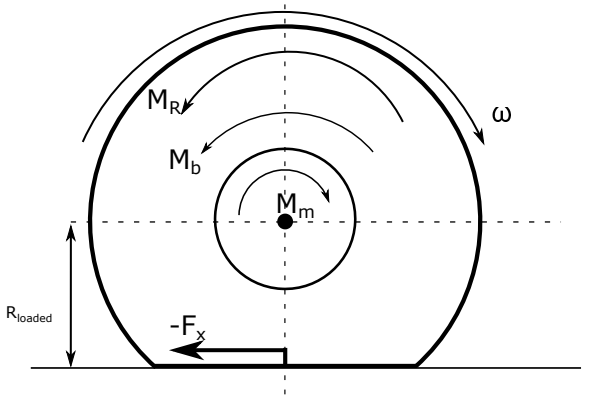

Figure 2.8: Rotational dynamic for a single wheel

motor torque. The braking torque only includes the torque from the hydraulic braking system. The reactionary force of the longitudinal tyre force generates a negative torque.

The compression and stretching of the rubber in the contact patch causes a rolling resistance. This torque is defined as $\mu_R F_z$, where μ_R is the rolling friction coefficient. This is a small, tyre dependent coefficient, usually of magnitude 10^{-2}.

2.3.4 Tyre models

Tyre models have been extensively researched throughout the years, not only for racing purposes but also for safety features for trucks and road cars. There are several models, varying from simplified static models, semi-empirical models and full transient models. In this thesis, the brush tyre model, and a simplified semi-empirical model will be used. The most simple tyre models are defined using only the tyre stiffness and slip[3, Chapter 1]. This is shown in Equation 2.20, and is valid for small slip angles, where the tyre is not sliding. As the goal is to find a longitudinal tyre model online, only pure longitudinal models are presented.

$$F_x = C_x \kappa \tag{2.20}$$

2.3.4.1 Brush Model

The brush model is derived by Pacejka in [3, Chapter 3], but a short introduction will be given here. The brush tyre model uses small brushes, with a stiffness c_{px}, to model the behaviour of the rubber as it traverses the contact patch. Figure 2.9 shows the concept, where the tyre carcass has been drawn as brushes. The tyre creates a pressure distribution q_z on the road surface, under the contact patch. The contact patch has a length of $2a$ and the tyre load is given as F_z. When the tyre is driven, the brushes stretch, resulting in a longitudinal force in the contact patch.

The definition of slip, σ_x, used in the brush model differs from the definition introduces in 2.3.1.1. They are however compatible using Equation 2.21.

$$\sigma_x = \frac{\kappa}{1 + \kappa} \tag{2.21}$$

An expression for the longitudinal force can be derived taking the integral of the deformation, defined as $u = (a - x)\sigma_x$, where x is the distance along the contact patch, over the contact patch is taken, shown in Equation 2.22.

$$F_x = c_{px} \int_{-a}^{a} u dx = 2 c_{px} a^2 \kappa \tag{2.22}$$

Comparing 2.22 and 2.20 we can derive the longitudinal stiffness as in Equation 2.23.

$$C_x = 2 c_{px} a^2 \tag{2.23}$$

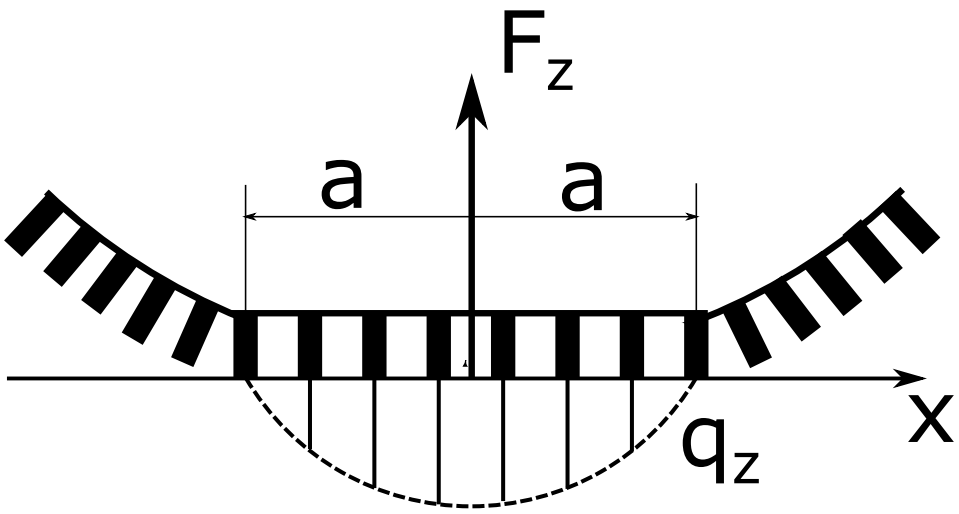

Figure 2.9: Illustration of the brush tyre model

Further, the maximum longitudinal force can be expressed using a friction coefficient μ and the pressure distribution q_z, originating from the stretching of the brushes, as shown in Equation 2.24.

$$F_{x_{max}} = \mu q_z \tag{2.24}$$

The stiffness and friction parameters have now been introduced, and the rest of the derivation of the brush model is explained in detail in [3, Chapter 3]. The final expression for the longitudinal tyre force is given in Equation 2.25.

$$f(C_x, \kappa) = C_x \frac{\kappa}{1+\kappa} \tag{2.25}$$

$$F_x(\kappa, C_x, F_z) = min(\mu F_z, f(C_x, \kappa) - \frac{f^2(C_x, \kappa)}{3\mu F_z} + \frac{f^3(C_x, \kappa)}{27\mu^2 F_z^2}) \tag{2.26}$$

The brush model simplifies the effects of sliding, and instead of a drop in longitudinal force for excessive slip ratios it stays level at μF_z. This means that the model is less accurate for high slip ratios than for example the semi-empirical Magic Formula model.

2.3.4.2 Magic Formula Models

This section is adapted from project thesis

As rubber tyre behaviour is hard to model accurately theoretically, semi-empirical models have been developed over the years. A commonly used family of tyre models is the Magic

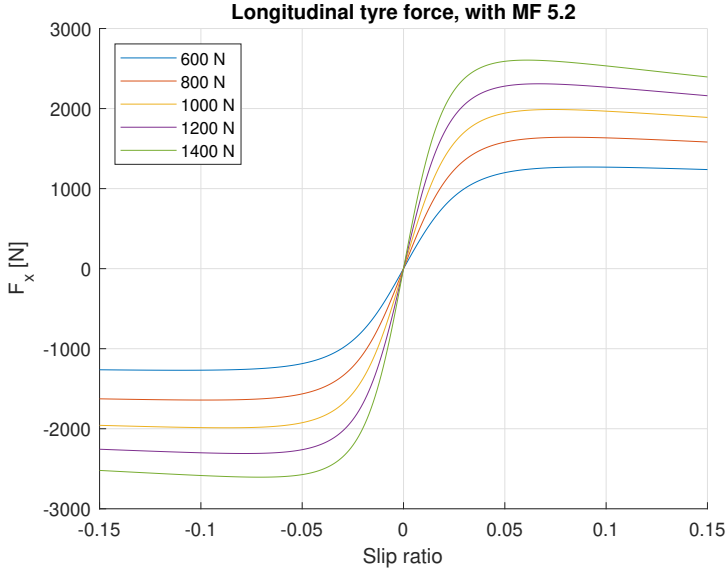

Figure 2.10: Example of a MF tyre model for longitudinal tyre forces

Formula family [3]. Each version tries to model more of the tyre dynamics including load sensitivity, camber angle and temperature[11]. The most basic form of a MF is defined in Equation 2.27 [3]. Figure 2.10 shows an example of the force-slip curve of a MF model.

$$F(\kappa) = D \cdot \sin\left(C \cdot \arctan\left(B\kappa - E \cdot B\kappa - \arctan\left(B\kappa\right)\right)\right) \tag{2.27}$$

The MF models can be used to model several of the forces and moments in a tyre. In this thesis, it will be used to model the longitudinal tyre forces. The coefficients B, C, D and E are fitted to tyre data, often from a flat-track testing session. These four coefficients can be further broken down into sub-equations, with more parameters. This is how more detailed models are designed. As these models are semi-empirical, the coefficients are not directly transferable to physical properties. However, each coefficient controls a different section of the curve, which can be summarized as follows:

- B: Stiffness coefficient
- C: Shape coefficient
- D: Scaling coefficient
- E: Peak coefficient

A commonly used Magic Formula variant is the Magic Formula 5.2. This model includes load sensitivity and camber effects and is shown in Appendix A. One common drawback of the Magic Formula family of tyre models, is the high number of parameters, often causing complex cost function landscapes when used for parameter estimation [4], [13].

To approximate the effects of tyre load sensitivity, the B, D and E parameters can be defined as linear or quadratic dependencies of F_z, as shown in Equations 2.28 [1], where F_{z_0} is a design parameter to scale the F_z steps. The effects of lateral tyre slip and tyre inclination angle are neglected in order to reduce the amount of parameters.

$$f_z = \frac{F_z}{F_{z_0}} \tag{2.28a}$$

$$C = C_a \tag{2.28b}$$

$$D = D_a + D_b f_z \tag{2.28c}$$

$$B = \frac{B_a + B_b f_z}{CD} \tag{2.28d}$$

$$E = E_a + E_b f_z + E_c f_z^2 \tag{2.28e}$$

2.4 Discrete Kalman Filter

The Kalman filter is a recursive filter, able to estimate the state of linear dynamic systems based on noisy measurements. With the use of a Kalman filter, both measured and unmeasured states can be estimated. The filter can be expressed for discrete-time and continuous-time systems.[5, Chapter 11]

2.4.1 State space

In this thesis, a discrete-time Kalman filter was designed for the estimation problem. The discrete-time Kalman filter is defined as a discrete linear time-varying state space model, as shown in Equation 2.29. The $\boldsymbol{A}$ and $\boldsymbol{B}$ matrices model the system behaviour, while the C matrix maps the measurements y to the system states x. In addition to the measurements and modelled dynamics, process and measurement noise are also accounted for in the model. The noise is denoted as $\boldsymbol{w}$ and $\boldsymbol{v}$ for the process and measurement noise respectively.

$$\begin{aligned} \boldsymbol{x}_{k+1} &= \boldsymbol{A}_d(k)\boldsymbol{x}_k + \boldsymbol{B}_d(k)\boldsymbol{u}_k + \mathbf{w}_k \\ \boldsymbol{y}_k &= \boldsymbol{C}_d(k)\boldsymbol{x}_k + \boldsymbol{v}_k \end{aligned} \tag{2.29}$$

The process noise $\boldsymbol{w}$ is assumed to be a zero-mean Gaussian white noise process, with a covariance matrix $\boldsymbol{Q}$. The measurement noise $\boldsymbol{v}$ is also assumed to be zero-mean Gaussian white noise process, with the covariance given in $\boldsymbol{R}$. Both matrices are given in Equations 2.30

$$\boldsymbol{Q} = \boldsymbol{Q}^T > 0 \tag{2.30a}$$

$$\boldsymbol{R} = \boldsymbol{R}^T > 0 \tag{2.30b}$$

2.4.2 Kalman filter algorithm

The Kalman filter has two design matrices, given in Equations 2.30. In most cases these are kept constant [5]. The initial conditions of the filter are defined in Equations 2.31.

$$\bar{\boldsymbol{x}}(0) = \boldsymbol{x}_0 \tag{2.31a}$$

$$\bar{\boldsymbol{P}}(0) = \boldsymbol{P}_0 \tag{2.31b}$$

The first step is updating the Kalman gain matrix $\boldsymbol{K}_k$, state estimate $\hat{\boldsymbol{x}}$, and error covariance $\hat{\boldsymbol{P}}$. This is done using the prediction from the previous time-step and the new measurement. The new measurement is used to correct the prediction. These steps are given in Equations 2.32.

$$\boldsymbol{K}(k) = \bar{\boldsymbol{P}}(k)\boldsymbol{C}_d^T(k)[\boldsymbol{C}_d(k)\bar{\boldsymbol{P}}(k)\boldsymbol{C}_d^T(k) + \boldsymbol{R}(k)]^{-1} \tag{2.32a}$$

$$\hat{\boldsymbol{x}}(k) = \bar{\boldsymbol{x}}(k) + \boldsymbol{K}(k)[\boldsymbol{y}(k) - \boldsymbol{C}_d(k)\bar{\boldsymbol{x}}(k)] \tag{2.32b}$$

$$\hat{\boldsymbol{P}}(k) = [\mathbb{I} - \boldsymbol{K}(k)\boldsymbol{C}_d(k)]\bar{\boldsymbol{P}}(k)[\mathbb{I} - \boldsymbol{K}(k)\boldsymbol{C}_d(k)]^T + \boldsymbol{K}(k)\boldsymbol{R}(k)\boldsymbol{K}^T(k) \tag{2.32c}$$

The Kalman gain, calculated in Equation 2.32a, serves as a weighting matrix for the prediction and the new measurement. By manipulating Equation 2.32b, which updates the state estimate this can be made clear. Equation 2.33 shows how the Kalman gain works as a weighting matrix.

$$\hat{\boldsymbol{x}}(k) = [\mathbb{I} - \boldsymbol{K}(k)\boldsymbol{C}_d(k)]\bar{\boldsymbol{x}}(k) + \boldsymbol{K}(k)\boldsymbol{y}(k) \tag{2.33}$$

As the state estimates and error covariance is updated, the predictions $\bar{\boldsymbol{x}}$ and $\bar{\boldsymbol{P}}$ are updated for the next step. This is shown in Equation 2.34

$$\bar{\boldsymbol{x}}(k+1) = \boldsymbol{A}_d(k)\hat{\boldsymbol{x}}(k) + \boldsymbol{B}_d(k)\boldsymbol{u}(k) \tag{2.34a}$$

$$\bar{\boldsymbol{P}}(k+1) = \boldsymbol{A}_d(k)\hat{\boldsymbol{P}}(k)\boldsymbol{A}_d^T(k) + \boldsymbol{Q} \tag{2.34b}$$

2.4.3 Observability

The key assumption when designing a Kalman filter is that the system model is observable[5, Chapter 11]. Observability is necessary in order to obtain convergence of the estimated state $\hat{x}$ and it allows to recursively reconstruct the state with the measurement vector y and input vector u from 2.29.

Observability can be interpreted as a measure of how well the internal states of a system can be inferred with the knowledge available from external outputs u and y. This means that the behaviour of the system can be determined using only the information provided by the external outputs of the system. If a system is not observable, the value of some

or all states cannot be determined by the controller, and it will be unable to meet the requirements set for it.[9]

For linear time-invariant systems, with state and output matrices A and H, the system is observable if the observability matrix is of full column rank. The observability matrix is defined in 2.35.

$$\mathcal{O} = \begin{bmatrix} \boldsymbol{C}^T & | & \boldsymbol{A}^T\boldsymbol{C}^T & | & \dots & | & (\boldsymbol{A}^T)^{n-1}\boldsymbol{C}^T \end{bmatrix} \tag{2.35}$$

For time-varying systems, there are no simple checks available for the observability of the system. There have been developed techniques to determine the observability of such systems, like uniform observability [9] or the use of an instantaneous observability matrix [19].

2.4.4 Euler discretisation

As finding the exact discretisation of a system involves complex calculations, the Euler method is used. The Euler method approximates the discretised system, using the equations given in Equation 2.36, where $\boldsymbol{A}$ and $\boldsymbol{B}$ are the continuous system matrices and ΔT is the discrete time-step. [7].

$$\boldsymbol{A}_d = \mathbb{I} + \Delta T \boldsymbol{A} \tag{2.36a}$$

$$\boldsymbol{B}_d = \Delta T \boldsymbol{B} \tag{2.36b}$$

2.5 System identification

System identification uses a reference model and available measurements to identify the properties of a system or plant. There are various methods that can be used to achieve this. For this thesis, an online parameter estimation scheme is developed, that identifies tyre model parameters, θ using a cost function and minimization algorithm. [6]

2.5.1 Gradient method

The gradient method, or "Method of steepest descent" is a method used to solve the unconstrained minimization problem, described in Equation 2.37. The method is one of the most basic solvers and is an iterative solver, computing the gradient of the cost function J at each time step. [6]

$$\begin{aligned} &\min \quad J(\theta) \\ &s.t \quad \theta \in \mathbb{R}^n \end{aligned} \tag{2.37}$$

The gradient method starts with an initial estimate, θ_0. The gradient is then used to traverse the cost function landscape to find the minimum solution θ^*. By using the negative

gradient, the steps are taken in the steepest direction, towards a local minimum using linear search d_k where

$$d_k = -\lambda \nabla J(\theta_k) \tag{2.38}$$

and

$$\nabla J(\theta) = \begin{bmatrix} \frac{\partial J}{\partial \theta_1} \\ \frac{\partial J}{\partial \theta_2} \\ \vdots \\ \frac{\partial J}{\partial \theta_n} \end{bmatrix} \tag{2.39}$$

Here, $\lambda \in \mathbb{R}$ is the step size of the method, which is a design parameter. The step size along the gradient can additionally be scaled with another design parameter Γ. Γ is a positive definite, diagonal matrix, and is defined as $\Gamma = \Gamma_1 \Gamma_1^T$, where Γ_1 is a $n \times n$ non-singular matrix. Γ allows for a different step size for each of the n parameters in θ. Adding the scaling factor gives us the final update law for the gradient method, defined in Equation 2.40 [6][20].

$$\theta_{k+1} = \theta_k - \lambda \Gamma \nabla J(\theta_k) \tag{2.40}$$

2.5.2 Convergence

The gradient method requires the cost function to be a convex function for a global minimum to be found. As the method traverses down the steepest direction at each time step, it has no opportunity to climb smaller hills in the landscape to approach a global minimum. This is illustrated in Figure 2.11a. With tuning of initial estimates, illustrated in Figure 2.11b or running several solvers in parallel and choosing the solver with the lowest value for J, a more optimal solution can be found, but not guaranteed.[20]

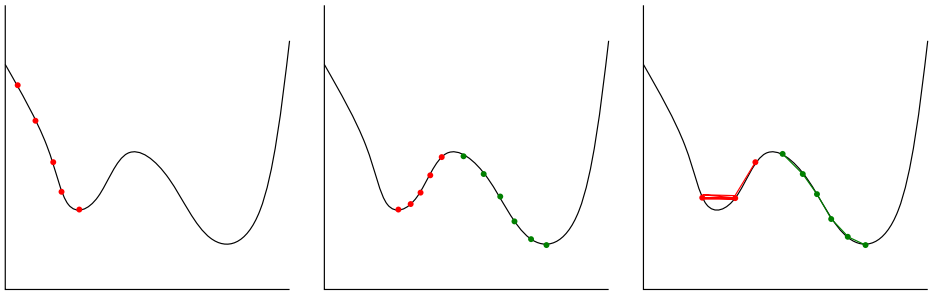

(a) Gradient method caught in a local minimum

(b) Initial estimate can guide the method to a local (red) or global (green) minimum

(c) Big step-sizes can prevent convergence to the minimum

The design parameters for the step size of the method also affect the convergence. Figure 2.11c illustrates how the step size can hinder convergence by stepping hovering over the

optimal solution. A smaller step size can increase accuracy, but also decrease how fast the solution can converge. For very steep gradients, a large step size can even step over local or global minimums. [20].

The estimation scheme in this thesis has a cost function that is time-varying. In order for the solver to converge to a solution, there has to be a θ_k that minimises the cost function $J(\theta, t)$ for any time t. If there is no such θ_k, the method will not converge, and the parameter estimation will not succeed.

2.5.3 Excitation

In order for a system identification scheme to successfully identify the reference model parameters, it needs to acquire information about the behaviour of the plant. If not enough information of the behaviour of the plant is fed to the scheme, it can converge to parameter values that do not fit the entire operating range of the plant.[6] It is therefore important to provide sufficient information to the estimation scheme, for example through the use of specific experiments.

2.6 Error metrics

The accuracy of the estimates can be analyzed using error metrics. For this thesis, two error metrics are used.

2.6.1 Root-mean-square error

The root-mean-square-error is useful to identify is an estimator has big outliers. As the error is squared before division, big outliers are weighted heavier than small errors. The error metric is defined in Equation 2.41.

$$RMSE = \sqrt{\frac{\Sigma_{t=1}^{T}(\hat{y}_t - y_t)^2}{T}} \tag{2.41}$$

2.6.2 Mean absolute error

The mean absolute error is defined in Equation 2.42. The main difference between the MAE and RMSE is that the MAE weights all errors equally, meaning that outliers are not dominating the final outcome.

$$MAE = \frac{\Sigma_{t=1}^{T}|\hat{y}_t - y_t|}{T} \tag{2.42}$$

Chapter 3

Kalman Filter Design

As there are no sensors mounted on the racecar that can measure the forces acting on the road surface, an estimator is required. With the use of the vehicle models described in Sections 2.2.3 and 2.2.4 and the rotational dynamics of tyres presented in Section 2.3.3, a discrete-time Kalman filter was designed. The Kalman filter is the first step of the system designed in this thesis. Based on equations of motion, measurements from the INS and motor encoders and states estimated in the initial state estimation, an estimate of the tyre forces is obtained.

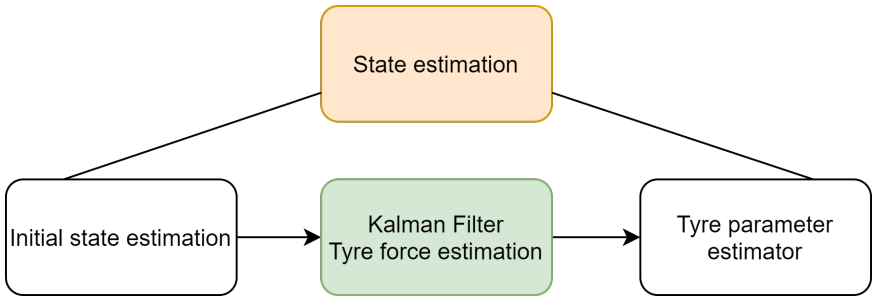

Figure 3.1: The Kalman filter is the second step in the tyre parameter estimation scheme

3.1 Discrete-time Kalman Filter

The discrete-time Kalman filter designed for the estimation of tyre forces uses measurements from the on-board INS and the wheel encoders located in the motors. Measurements for longitudinal and lateral acceleration and yaw rate are gathered from the INS, while motor RPM data is gathered from the encoders. The RPM measurements are converted to rotational velocity in rad/s using $\omega_i = RPM_i \frac{30\pi}{GearRatio}$. The states and measurement

vectors are defined in Equation 3.1.

$$\boldsymbol{x} = \begin{bmatrix} F_{x_{FL}} & F_{x_{FR}} & F_{x_{RL}} & F_{x_{RR}} & F_{y_f} & F_{y_r} & \omega_{FL} & \omega_{FR} & \omega_{RL} & \omega_{RR} & r \end{bmatrix}^T$$
$$\boldsymbol{y} = \begin{bmatrix} (m \cdot a_x + F_{drag}) & (m \cdot a_y) & \omega_{FL} & \omega_{FR} & \omega_{RL} & \omega_{RR} & r \end{bmatrix}^T \tag{3.1}$$

Besides the tyre forces, the remaining states are measured directly and have dynamics. The tyre forces are not measures, and no equations describing their dynamics exist. Instead, the equations of motion from Chapter 2 are used to map the INS measurements to the states. It is important to note that the lateral forces on each axle have been combined to one force. This is discussed more in detail in Section 3.2.

3.1.1 State Space model

The above described system can be implemented as a linear time-varying system, on the state space form described in Section 2.4, Equation 2.29.

As seen in Equation 3.1, the INS measurements are multiplied with the vehicle mass to get the overall equations on the form of Newtons second law $\sum F_x = m \cdot a_x$. As the drag experienced by the vehicle is not part of the states, this force is subtracted from the measurement of a_x. The drag force is estimated by the TV state estimation module.

3.1.1.1 Dynamics

The system matrix $\boldsymbol{A}$ is presented in Equation 3.2 and input matrix $\boldsymbol{B}$ in Equation 3.3. As mentioned, the dynamics for the tyre forces are unknown, and set to zero. For the rotational dynamics of the tyre, Equation 2.19 is used for each individual tyre. The longitudinal tyre forces have an arm of R_l, and are included in $\boldsymbol{A}$. The motor- and brake torque and rolling resistance are included in $\boldsymbol{B}$. The yaw dynamics are included in the final row of $\boldsymbol{A}$, using a combination of Equation 2.14 and Equation 2.8.

$$\boldsymbol{A} = \begin{bmatrix} & & \mathbb{0}_{11\times 6} & & & & \\ \frac{-R_{L_{FL}}}{I_\omega} & 0 & 0 & 0 & 0 & 0 & \\ 0 & \frac{-R_{L_{FR}}}{I_\omega} & 0 & 0 & 0 & 0 & \\ 0 & 0 & \frac{-R_{L_{RL}}}{I_\omega} & 0 & 0 & 0 & \mathbb{0}_{5\times 5} \\ 0 & 0 & 0 & \frac{-R_{L_{RR}}}{I_\omega} & 0 & 0 & \\ \frac{-t\cos\delta_L + l_f \sin\delta_L}{I_z} & \frac{t\cos\delta_R + l_f \sin\delta_R}{I_z} & \frac{-t}{I_z} & \frac{t}{I_z} & \frac{l_f \cos\frac{\delta_L+\delta_R}{2}}{I_z} & \frac{-l_r}{I_z} & \end{bmatrix} \tag{3.2}$$

$$\boldsymbol{B} = \begin{bmatrix} \mathbb{0}_{1\times 6} & \boldsymbol{B}_{\omega_{FL}} & \boldsymbol{B}_{\omega_{FR}} & \boldsymbol{B}_{\omega_{RL}} & \boldsymbol{B}_{\omega_{RR}} & 0 \end{bmatrix}^T \tag{3.3a}$$

$$\boldsymbol{B}_{\omega_i} = \frac{(\tau_{m_i} - \tau_{b_i} - R_{l_i} F_{z_i} \mu_R)}{I_\omega} \tag{3.3b}$$

The input vector $\boldsymbol{u}$ is a constant in the state space, defined in Equation 3.4.

$$\boldsymbol{u} = 1 \tag{3.4}$$

3.1.1.2 Measurements

The output matrix $\boldsymbol{C}$, mapping measurements to the states is given in Equation 3.5. The first row includes the longitudinal equation of motion, from Equation 2.10. Row two contains the lateral equations of motion, from Equation 2.12. The remaining states are measured directly, meaning that their $\boldsymbol{C}$ components are equal to 1.

$$\boldsymbol{C} = \begin{bmatrix} \cos\delta_L & \cos\delta_R & 1 & 1 & -\sin\frac{\delta_L+\delta_R}{2} & 0 & 0 & 0 & 0 & 0 & 0 \\ \sin\delta_L & \sin\delta_R & 0 & 0 & \cos\frac{\delta_L+\delta_R}{2} & 1 & 0 & 0 & 0 & 0 & 0 \\ & & \mathbb{0}_{5\times6} & & & & & & \mathbb{I}_{5\times5} & & \end{bmatrix} \tag{3.5}$$

3.2 Observability

As the system in not a LTI, the usual approach to checking the observability of a system through the observability matrix is not feasible. Looking at the equations of motion used for the state space model, it can be seen that the lateral forces on the same axle have the same arm and sign. For readability, the $\boldsymbol{F_y}$ terms for longitudinal, lateral and yaw dynamics are shown in Equations 3.6, 3.7 and 3.8 respectively.

$$-\boldsymbol{F}_y \cdot \begin{bmatrix} \sin\delta_l \\ \sin\delta_r \\ 0 \\ 0 \end{bmatrix} \tag{3.6}$$

$$\boldsymbol{F}_y \cdot \begin{bmatrix} \cos\delta_l \\ \cos\delta_r \\ 1 \\ 1 \end{bmatrix} \tag{3.7}$$

$$\boldsymbol{F_y} \begin{bmatrix} (l_f \cos\delta_L + \frac{t_f}{2}\sin\delta_L) \\ (l_f \cos\delta_R - \frac{t_f}{2}\sin\delta_R) \\ -l_r \\ -l_r \end{bmatrix} \tag{3.8}$$

The rear lateral tyre forces always have the same arm and direction. This means that there is no way for the Kalman filter to determine the individual magnitude of each. For the front tyres, the arm and magnitude are affected by the wheel angle δ. As long as the two wheel angles are sufficiently different, the front lateral forces could be observable. The racecar is equipped with an Ackermann steering geometry. This means that the two wheels do

not turn equal amounts when the steering wheel is turned. The wheel angles, for the entire steering wheel range is shown in Figure 3.2. For steering angles around -30 to 30 degrees, the wheel angles are identical. Beyond this, they diverge.

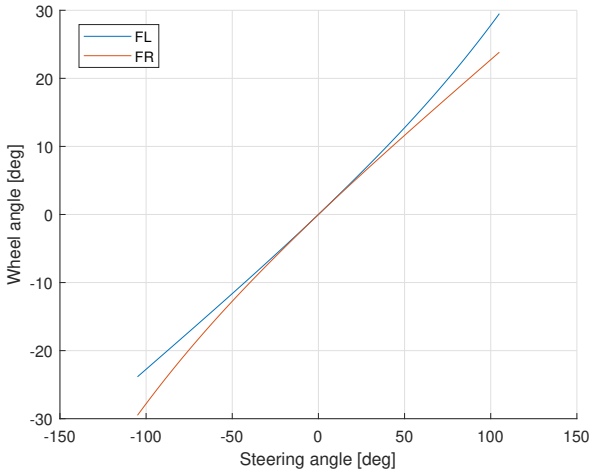

Figure 3.2: Wheel angles for steering wheel range

The steering wheel input from the Formula Student Germany competition in 2019 is shown in Figure 3.3. It shows that the steering input is mostly between -60 and 60, with some occasional spikes that go higher. Comparing the two wheel angles for this range shows that the difference in wheel angle is quite small.

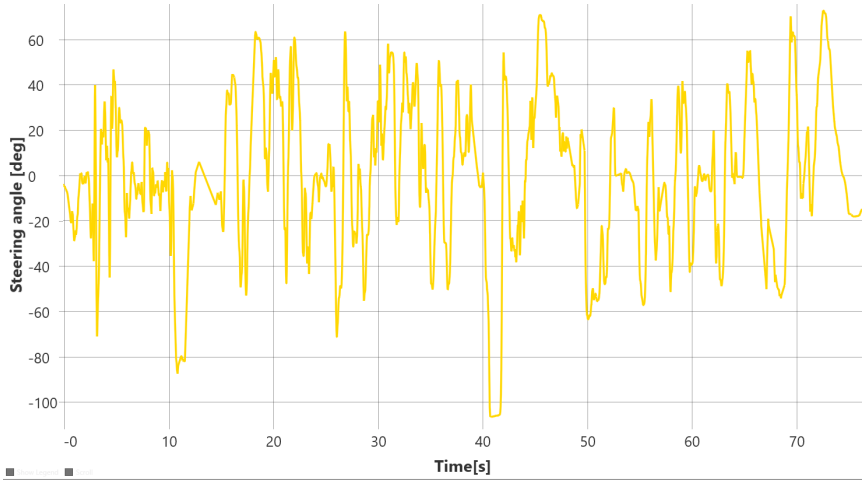

Figure 3.3: Wheel angles for steering wheel range

In order to improve the observability of the system, the lateral tyre forces on each axle are combined, as in Equation 3.9. The average wheel angle is used to model the lateral forces using the single track vehicle model described in Section 2.2.3. With the lateral forces combined for each axle, the singularity is primarily limited to the situation where the vehicle travels in a straight line. In this case, the front and rear axle contribute equally to the lateral acceleration as $\cos(\delta)$ will be 1, and against each other in the yaw acceleration as the front and rear wheelbase is identical. This will make the lateral force estimates unreliable, but since the longitudinal forces are the priority this will not be improved.

$$F_{y_f} = F_{y_{FL}} + F_{y_{FR}} \tag{3.9}$$

$$F_{y_r} = F_{y_{RL}} + F_{y_{RR}} \tag{3.10}$$

3.3 Co-variance matrices

The Kalman filter uses the co-variance matrices for the process noise and measurement noise in the update law. These are design parameters that can be seen as weighting parameters for the model and measurements. For example, a measurement with measurement noise with a high variance should be trusted less than the prediction with a low variance process noise. The variance of the measurement noise can be found from experimental data, gathered with the sensor in a known static position.

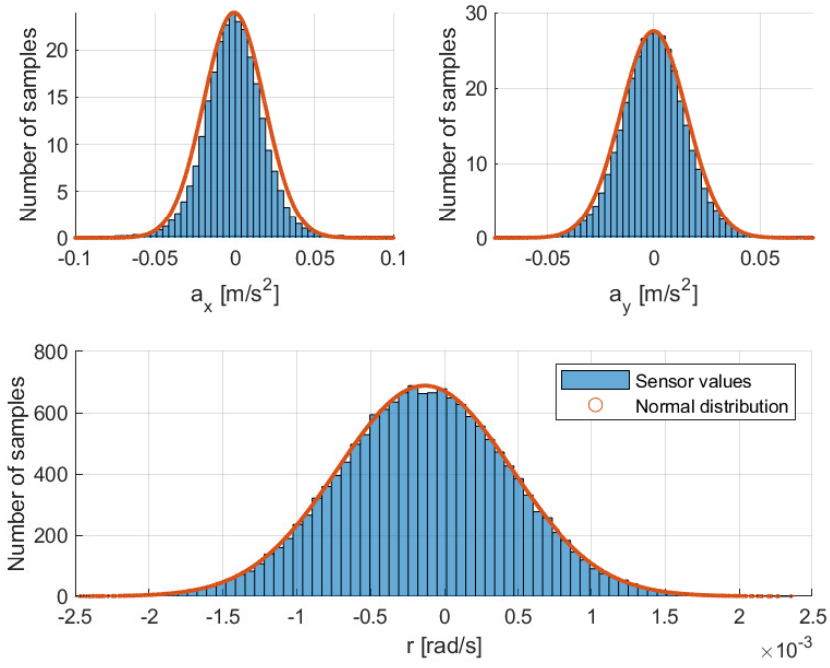

Figure 3.4: Sensor measurements and matching normal distribution

Measurement	Variance
a_x	$3.625 \cdot 10^{-4}$
a_y	$2.398 \cdot 10^{-4}$
r	$3.463 \cdot 10^{-7}$

Table 3.1: Sensor measurement variance

Figure 3.4 shows a histogram of the INS measurements with the racecar standing still. On top of the histograms, a normal distribution with the same variance is presented. The variance values are given in Table 3.1.

The rotational velocity of the wheels are measured with a digital sensor, meaning that an experimental approach to identifying the noise characteristics is unfeasible. Instead, the variance values need to be tuned experimentally on the racecar.

Using Matlab, the full covariance matrix for the data-set is found. The matrix $\boldsymbol{R}$ is given below, in Equation 3.11, where R_{ω_i} has to be found experimentally. The process noise is included in the Kalman equations via the $\boldsymbol{Q}$ matrix. This is a design variable that models the disturbances in the model. The filter used in this thesis has no model for the tyre forces, meaning that the model cannot be trusted. The values for the tyre forces in $\boldsymbol{Q}$ should therefor be large. The tyre rotational velocity and vehicle yaw rate dynamics are however modeled, therefor the corresponding values for $\boldsymbol{Q}$ can be small.

$$\boldsymbol{R} = \begin{bmatrix} 3.625 \cdot 10^{-4} & 1.282 \cdot 10^{-5} & 0 & 0 & 0 & 0 & 2.046 \cdot 10^{-7} \\ 1.281 \cdot 10^{-5} & 2.398 \cdot 10^{-4} & 0 & 0 & 0 & 0 & 0 \\ 0 & 0 & R_{\omega_{FL}} & 0 & 0 & 0 & 0 \\ 0 & 0 & 0 & R_{\omega_{FR}} & 0 & 0 & 0 \\ 0 & 0 & 0 & 0 & R_{\omega_{RL}} & 0 & 0 \\ 0 & 0 & 0 & 0 & 0 & R_{\omega_{RR}} & 0 \\ 2.397 \cdot 10^{-7} & 2.046 \cdot 10^{-7} & 0 & 0 & 0 & 0 & 3.463 \cdot 10^{-7} \end{bmatrix} \tag{3.11}$$

Chapter 4

Online Parameter Estimation

As different racetracks have different road surface properties, an online estimation scheme has been designed to update the tyre parameters during operation. This is achieved using the gradient descent method, using a simplified tyre model as reference model. The estimated tyre forces from the Kalman filter in Chapter 3 are used to identify the tyre parameters. This chapter will cover the design of the estimation scheme, and how data is selected for use in the update law.

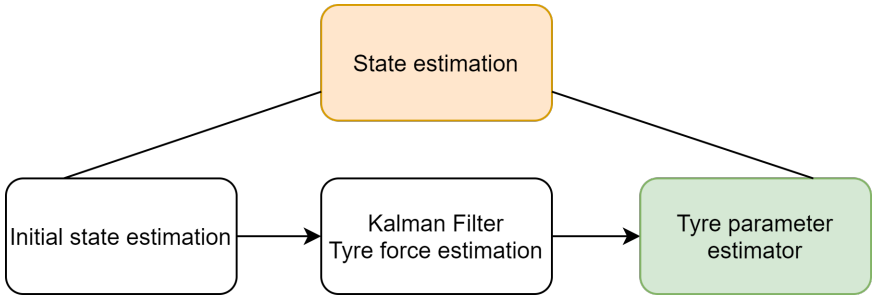

Figure 4.1: The tyre parameter estimator uses the output from the Kalman filter

4.1 Model excitation

As the race car will be driving in different conditions, like hard braking, cornering and acceleration, the model will experience various operating conditions. As an iterative solver is used to solve the optimisation problem, it is important to ensure that data from the entire operating range is used to update θ.

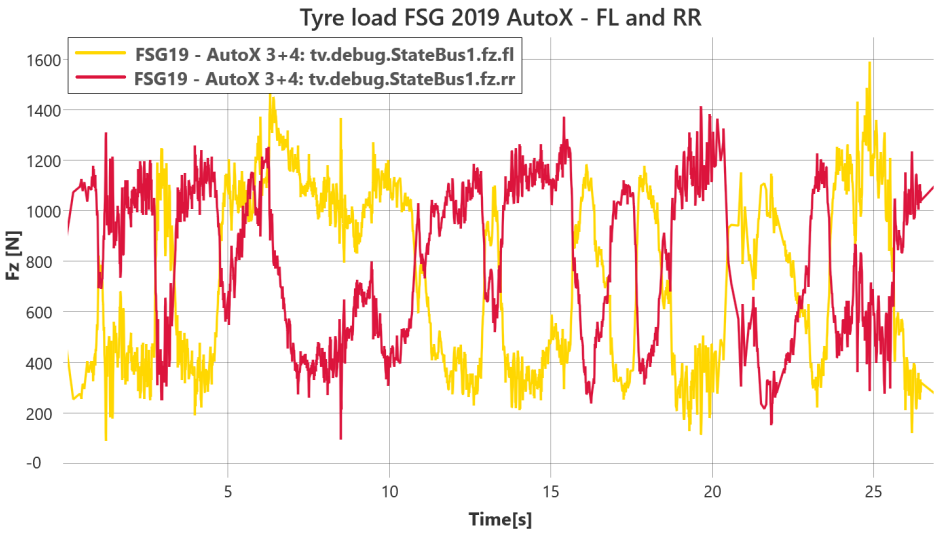

Figure 4.2: Tyre loads for the front left and rear right tyre

4.1.1 Operating conditions

The tyre model is dependent on two vehicle states, namely the tyre load and slip ratio. The slip ratio range used by race cars is ± 0.15, while the tyre load varies based on the vehicle type. To determine the range of F_z Revolve NTNU's race cars experience, data gathered in earlier seasons was analysed.

The loads on the front left and rear right tyre of the 2019 race car is shown in Figure 4.2. The tyres experience loads between $300N$ and $1300N$, with some rare peaks going as high as $1600N$.

4.1.2 Online data selection

To ensure the parameters are not over-fitted to the last conditions the race car has experienced, θ is updated using an average gradient for a set of datapoints. The goal is to include datapoints from the entirety of the operational range of the race car. This is done by creating a grid, with F_z on the y-axis, and κ on the x-axis. Whenever a new state is estimated four new datapoints are available, one for each tyre. These are then inserted into the corresponding bin. Each bin corresponds to an F_z and κ range, and can hold up to 2 datapoints. If a bin is full, the oldest data-point is discarded. Using Figure 4.2, we can see that the tyres is most often loaded with a force in the range of $300 - 500$ N or $1000 - 1200$ N. This, combined with general knowledge of slick racing tyres reaching peak performance in the range $0.04 - 0.1$, was used to design the grid, shown in Figure 4.3.

As each datapoint contains a slip ratio, longitudinal tyre force and a tyre load, the amount of floats needing to be processed by the micro-controller is given in Equation 4.1.

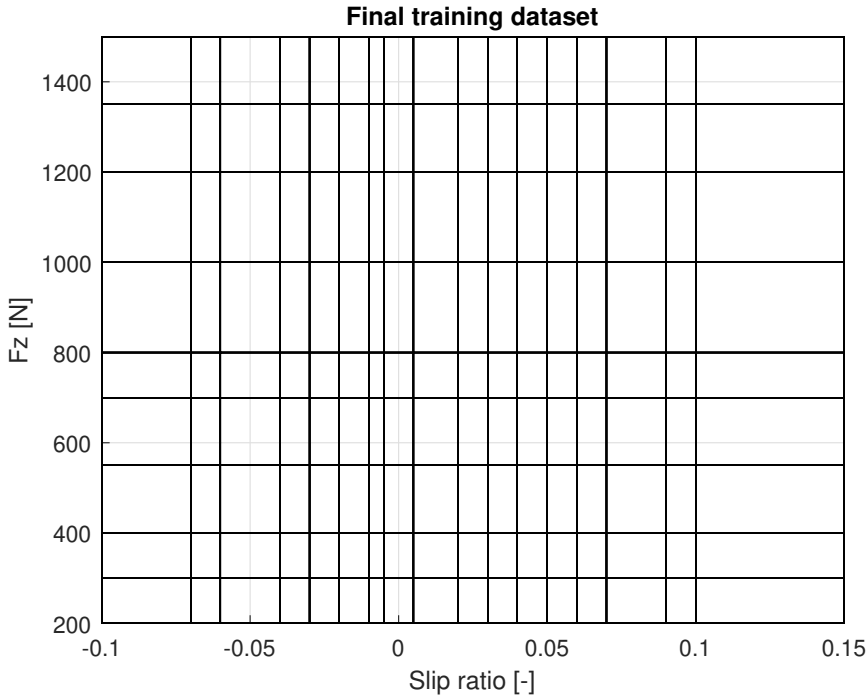

Figure 4.3: Grid showing the chosen borders. Each slot can hold 2 datapoints

$$N_{floats} = 3 \cdot N_{bins} \cdot N_{pointsperbin} \tag{4.1}$$

The final grid design includes 180 bins, with two datapoints per bin. This means that the maximum number of floats needing to be handled by the micro-controller per iteration is 1080. In most situation, the true amount of computation required is a lot less, as some of the extreme bins, especially for high tyre loads, are not filled during regular driving condition. These bins exist in order to reduce implementation complexity.

4.2 Cost function

The online parameter estimation scheme aims to minimise the value of a cost function, which is a function of the estimated tyre functions and θ. Calculating the gradient of the cost function allows for the use of the steepest descent method to find a local minimum. The cost function used is given in Equation 4.2. $\hat{F_x}$, F_z and κ are obtained from the Kalman Filter and the state estimation module of the TV system. $f(\theta, F_z, \kappa)$ represents the implemented tyre models, described in Sections 2.3.4.1 and 2.3.4.2, where θ are the model coefficients.

$$J_k(\theta_k, F_z, \kappa, \hat{F_x}) = (\hat{F_x} - f(\theta_k, F_z, \kappa))^2 \tag{4.2}$$

The gradient is then computed by differentiating J with respect to θ, as shown in Equation 4.3.

$$\nabla J_k(\theta_k, F_z, \kappa, \hat{F_x}) = \begin{bmatrix} \frac{\partial J_k(\theta_k, F_z, \kappa, \hat{F_x})}{\partial \theta_1} \\ \frac{\partial J_k(\theta_k, F_z, \kappa, \hat{F_x})}{\partial \theta_2} \\ \vdots \\ \frac{\partial J_k(\theta_k, F_z, \kappa, \hat{F_x})}{\partial \theta_n} \end{bmatrix}^T \tag{4.3}$$

4.2.1 Tyre model

Two tyre models are tested for the parameter estimation. The brush model is the simplest, only using four parameters while the magic formula model has eight. Both tyre models are on the form used in Equation 4.2, referred to as $f(\theta, F_z, \kappa))$. This gives two different θs, one for each model.

4.2.1.1 Brush tyre model

The brush tyre model, described in Section 2.3.4.1 is dependent on two parameters that are unknown and tyre dependent. These are the friction coefficient and the longitudinal tyre stiffness. These are to be estimated online. In order to improve the model, both parameters

are expanded to be dependent on tyre load. This is done in a similar manner as other semi-empirical tyre models, and is shown in Equation 4.4, where F_{z_0} is a design parameter, set to $800N$

$$f_z = \frac{F_z - F_{z_0}}{F_{z_0}} \tag{4.4}$$

$$C_x = C_{x_a} + Cx_b \cdot f_z \tag{4.5}$$

$$\mu = \mu_a + \mu_b \cdot f_z \tag{4.6}$$

This gives the final set of parameters for the brush model, denoted as θ for the estimation problem in Equation 4.7.

$$\theta_{brush} = \begin{bmatrix} C_{x_a} & Cx_b & \mu_a & \mu_b \end{bmatrix}^T \tag{4.7}$$

4.2.1.2 Magic Formula tyre model

The eight parameters of the magic formula are divided into four main parameters. B_a and B_b mode the load sensitive tyre stiffness, C models the overall curve shape, D_a and D_b model the load sensitive friction coefficient, just like the the brush model. The parameters E_a, E_b and E_c model the tyre drop-off, and is the only second order polynomial in the two tyre models. The θ used for the magic formula model estimator is given in Equation 4.8.

$$\theta_{mf} = \begin{bmatrix} B_a & B_b & C & D_a & D_b & E_a & E_b & E_c \end{bmatrix}^T \tag{4.8}$$

4.2.2 Normalisation

In order to get all parameters on the same order of magnitude, they are scaled before being used in the tyre model. This is to weight all parameters equally in the update law, and to prevent extreme steep gradients in single dimensions. Tables 4.1a and 4.1b show the scaling for each parameter.

Parameter	Scaling factor
C_{x_a}	10^4
C_{x_b}	10^5
μ_a	1
μ_b	1

(a) Brush model scaling factors

Parameter	Scaling factor
B_a	10^2
B_b	10^1
C	1
D_a	1
D_b	1
E_a	10^{-1}
E_b	10^{-1}
E_c	10^{-2}

(b) Magic Formula scaling factors

Table 4.1: Scaling factors for the normalisation of both model's parameters

4.3 Estimation update law

The data-set collected by the online data selection algorithm is then used to define the update law for the estimation scheme. The gradient, described in Section 4.1.2 is calculated for each valid datapoint in the bins. This results in a vector of gradients. The average of each column in the gradient vector is used to update $\hat{\theta}$. The full update law, for a data-set containing M datapoints, and a θ with N parameters is given in Equations 4.9 and 4.10, where Γ is a design parameter that control the step size in each dimension.

$$\boldsymbol{J}_k(\hat{\theta}_k, \boldsymbol{F_{z_k}}, \boldsymbol{\kappa_k}, \hat{\boldsymbol{F}}_{\boldsymbol{x_k}}) = \begin{bmatrix} \nabla J_1(\hat{\theta}_k, F_{z_1}, \kappa_1, \hat{F_{x_1}}) \\ \nabla J_2(\hat{\theta}_k, F_{z_2}, \kappa_2, \hat{F_{x_2}}) \\ \vdots \\ \nabla J_M(\hat{\theta}_k, F_{z_M}, \kappa_M, \hat{F_{x_M}}) \end{bmatrix} = \begin{bmatrix} \nabla J_{1_{\theta_1}} & \dots & \nabla J_{1_{\theta_N}} \\ \nabla J_{2_{\theta_1}} & \dots & \nabla J_{2_{\theta_N}} \\ & \vdots & \\ \nabla J_{M_{\theta_1}} & \dots & \nabla J_{M_{\theta_N}} \end{bmatrix} \tag{4.9}$$

$$J_{avg_k} = \frac{1}{M} \begin{bmatrix} \sum_{i=1}^{M} \nabla J_{i_{\theta_1}} & \sum_{i=1}^{M} \nabla J_{i_{\theta_2}} & \dots & \sum_{i=1}^{M} \nabla J_{i_{\theta_N}} \end{bmatrix}$$

$$\theta_{k+1} = \theta_k - \Gamma J_{avg_k} \tag{4.10}$$

4.3.1 Stability

The parameters are updated every time step, using the latest data-set. The design parameter Γ is used to determine the step size for each dimension along the final gradient. Tuning Γ is important for the rate of convergence, and for stability. The gradient descent method is only guaranteed to converge to a global minimum if the optimisation problem is linear and convex. In this case however, the problem is neither linear or convex. The complexity of the entire system makes a Lyapunov analysis of the estimation scheme infeasible. Instead, careful tuning of the initial estimate and step size Γ through experiments is required.

Chapter 5

Implementation

The kalman filter and tyre estimator have been implmeneted in the TV Simulink model. Both use input from the sensor bus and the initial state estimation. As the target hardware has a 32-bit architecture, as much as possible is implemented using single floating points. The only part of the system where doubles are used is the Kalman filter, as the block inputs require this.

5.1 Kalman filter

For each time-step, the system matrices have to be calculated. The various model inputs are gathered from the state estimation output and sensor readings to assemble the system matrices. As we are using a discrete-time Kalman filter, the system matrices are discretised using Euler discretisation, described in Section 2.4.4.

The system matrices are used as input to the Kalman Filter Simulink Block [15]. As the filter is discrete, rate transition blocks [17] are used to ensure the data is processed at the same rate. The state estimates output from the Kalman Filter are then broken down into F_x, F_y and vectors before being used by the Tyre Estimator. The subsystem is shown in Figure 5.1.

5.2 Online parameter estimation

The online parameter estimator uses the Kalman filter states and tyre load and slip ratio from the initial state estimation module. Both the brush and magic formula models are implemented in parallel, and use the same data-set for their iteration.

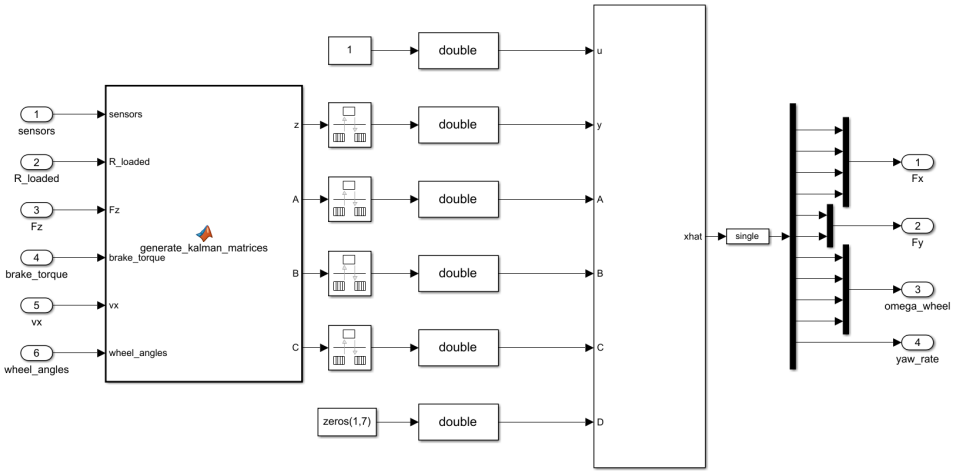

Figure 5.1: Kalman filter subsystem in Matlab Simulink

5.2.1 Data selection algorithm

For each time-step, the Kalman filter states and tyre load and slip ratio are evaluated. Datapoints outside the limits of the grid are discarded. The correct bin index is found using the tyre load and slip ratio. The oldest point is then replaced with the new datapoint. Each datapoint consists of an F_x, F_z and a κ. All empty bins are set to zero, and as the tyre load bins start at $200N$, this can be used to find the data-set size.

5.2.2 Gradient

The gradient is found using the Matlab Symbolic Toolbox[21]. The tyre models are implemented so that the input can be vectors with several datapoints. Using symbolic expressions and the tyre models, the cost function is defined. A function for calculating the gradient for a set of datapoints is then code generated, with the use of the Symbolic Toolbox.

5.2.3 Update law

The update law is implemented in a Matlab Function block, where θ is a persistent variable. For each time-step, the data-set size is checked, and once over the threshold the update law is evaluated. The gradient is calculated for all datapoints in the data-set, and the average gradient for each parameter is used to update θ.

Chapter 6

Simulation environment

6.1 Simulation environment

As the racecar is not finished before the middle of the 2021 summer, the results in this thesis are gathered in a simulation environment. Through the Formula Student program of IPG Automotive, access to their simulation environment IPG Carmaker was granted. IPG Carmaker allows for custom vehicle models and tyre models, and can run the system even with a human driver behind the wheel and running the control systems and estimators on the designated hardware.

6.1.1 Vehicle Model

A simplified vehicle model, based on the 2019 Revolve NTNU racecar is implemented in IPG Carmaker. The model includes a powertrain matching the 4WD electric powertrain of the real-life car, a fully modelled suspension, aerodynamics and a tyre model. This is to get a realistic as possible result for our simulations. There are however some limitations to the model that need to be considered. The mathematical models implemented in the simulation environment are highly simplified, meaning that the result are expected to be a lot better in the simulation than in the real world. Furthermore, the driver implementation is a limiting factor in pushing the vehicle limits. The complexity of the simulation environment also means that it can be seen as a black box, with limited knowledge of the internal workings. Results therefor need to be verified in real-life, through extensive track testing.

6.1.2 Tyres

The racecar in the simulation environment is equipped with a tyremodel provided by the tyre manufacturer of the Continental Formula Student tyres. These tyres have been used by Revolve NTNU since 2017, and we have adjusted the model using data gathered during the testing seasons. As we have no tyremodel for the new Hoosier tyres, the system is

simulated and tested on a vehicle with the Continental model. The tyremodel for the Hoosier tyres that is estimated during the summer of 2021 can then be imported into the simulation environment for the next seasons, in addition to being used online for traction estimation.

6.1.3 Data acquisition

IPG Carmaker gives access to all vehicle stats during a simulation. These represent the ground truth of the state value. In addition to logging the data for comparison with the estimator, it is also used as input to the system during simulation in the form of sensor measurements. To increase the realism of the simulation environment, Gaussian noise is added to all data before it is used by the TV system. The variance of the noise is determined like described in Section 3.3, based on data gathered in previous racing seasons.

6.2 Hardware-in-the-loop testing

As the control systems and state estimators are designed for use on a racecar, they need to be able to run on the on-board VCU. In order to eliminate issues with the software-hardware compatibility, HIL testing has been performed. The Matlab Simulink diagram is used to generate embedded C code, that can be executed on the racecar hardware.

6.2.1 Hardware

The Vehicle Control Unit is a in-house developed PCB, featuring a Xilinx's Zynq-7000 series System On Chip [14]. It includes a dual-core micro-controller on which the estimator will run. The TV systems, including the tyre parameter estimator run on the secondary core, while the vehicles state machine, data acquisition and safety monitoring tasks are performed on the primary core. The restriction of one core is one of the reasons that the optimisation problem in the online tyre parameter estimator is not running asynchronous of the rest of the TV systems. The VCU is designed by Sivaranjith Sivarasa from the Embedded Electronics group in Revolve NTNU and is shown in Figure 6.1.

6.2.2 Driver-in-the-loop testing

As the simulation-driver targets to operate the vehicle optimally, no information will be available to the estimation scheme of tyre behaviour outside the optimal range. In addition to this, the simulation driver also behaves very different from a human driver. Therefor Driver-in-the-loop testing has been used to gather more accurate driving data. Using a commercially available steering wheel and pedals, a human driver was given control of the vehicle in the IPG Carmaker simulation environment.

One downside of the use of a human driver is the inconsistency. Even though the driver got a few hours of practice driving, the runs were not as consistent as the simulation driver. This meant that more time had to be spent on the simulations to gather representative results.

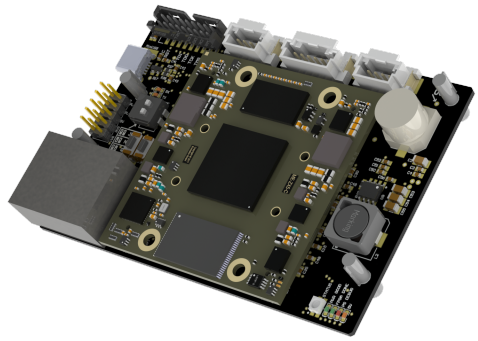

Figure 6.1: Render of the 2021 Vehicle Control Unit

6.2.3 Communication

All PCBs on the racecar are connected on a CAN network. This way the Sensor broadcasting systems can relay the sensor measurements to the VCU. In addition to communication between systems on the vehicle, the CAN network is also broadcast live to the crew monitoring and tuning the vehicle in real-time. Through this wireless link, the TV systems and state estimators can be tuned without having to reprogram the micro-controllers. For every iteration of the state estimator, the results are broadcast allowing for efficient tuning on track. During HIL testing, the flexibility of scoping signals in Simulink is lost, meaning all data that is interesting need to be extracted over the CAN bus.

The testing setup is shown in Figure 6.2, including the steering wheel, VCU and two computers. One for running the IPG Carmaker simulations and one for communication with the CAN bus that the VCU outputs the data too.

6.3 Track layout

Different track layouts, using elements as described in the Formula Student rules[16], were used for the simulations in this thesis. In addition to a simple straight track, a skidpad and a full circuit were used. A skidpad track is defined as a figure of eight, with a center-line radius of $18.25m$. A skidpad procedure first takes two turns in the right circle, and then two turns in the left circle.

The full circuit layout can be seen on Figure 6.3. It features a lot of tight curves, two hard braking zones at the end of the straights, and corners with a variety of radii. It is worth noting that the track is driven in a clockwise direction, meaning that there will be an overweight of right corners. This will affect the magnitude of the generated tyre forces on the left and right side of the racecar due to the affects of load transfer in cornering, described in Section 2.2.1.

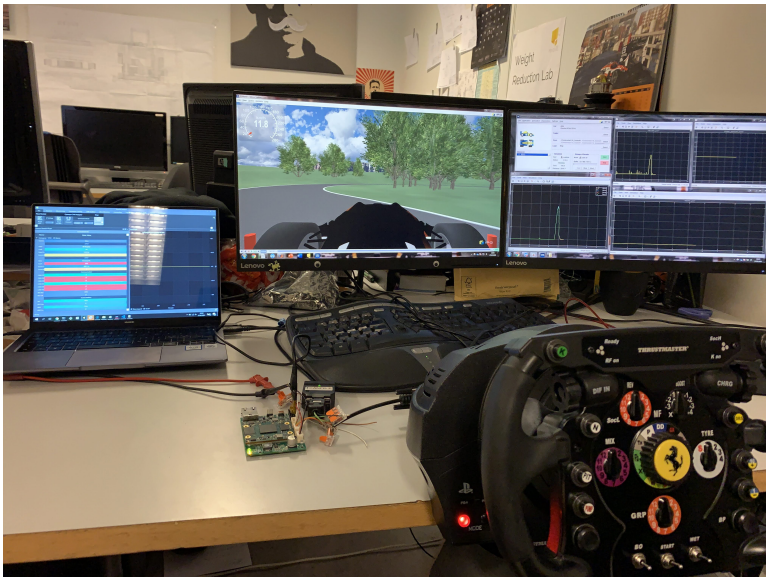

Figure 6.2: Testing setup, with hardware and driver controls

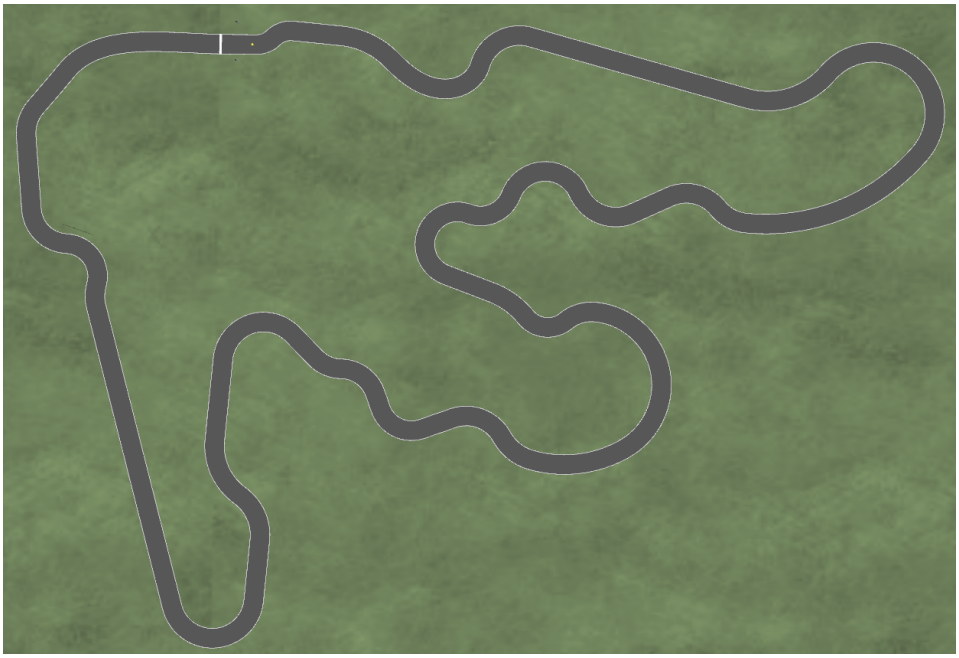

Figure 6.3: Simulation track layout

Chapter 7

Results and Discussion - Kalman Filter

The Kalman Filter designed in Chapter 3 is the first step of the tyre-road friction estimation scheme. The longitudinal tyre forces estimated by the filter will be the basis of the tyre estimation. Therefor, the estimate of the longitudinal tyre force is the most crucial to get accurate. Results for the lateral forces will also be presented in this section. To judge the performance of the Kalman filter, three cases will be studied: straight line acceleration, steady state cornering and a full circuit. Straight line acceleration consists of several acceleration phases up to top speed, followed by a hard braking. Steady state cornering is performed on a skidpad track, made up of two $360\,\mathrm{deg}$ turns, one to the left, and one to the right. The full circuit is described in Section 6.3.

7.1 Tuning

The covariance matrices were tuned experimentally using the estimated covariance presented in Section 3.3 as a starting point for $\boldsymbol{R}$. The RPM measurement noise was tuned experimentally. All $\boldsymbol{R}$ values should be recalculated using sensor readings once the 2021 race car is ready for testing. The final $\boldsymbol{R}$ matrix used for the simulations is given in Equation 7.1. The final $\boldsymbol{Q}$ matrix is presented in Equation 7.2. As there are no dynamics modeled for the tyre forces, the respective $\boldsymbol{Q}$ values were set high. The rotational dynamics for the wheel and yaw dynamics are modeled, so these values were set low. The final values were achieved by running several simulations and looking at transient and steady-state accuracy.

$$\boldsymbol{R} =$$

$$\begin{bmatrix} 3.83 \cdot 10^{-4} & 0 & 0 & 0 & 0 & 0 & 0 \\ 0 & 1.89 \cdot 10^{-4} & 0 & 0 & 0 & 0 & 0 \\ 0 & 0 & 5 \cdot 10^{-8} & 0 & 0 & 0 & 0 \\ 0 & 0 & 0 & 5 \cdot 10^{-8} & 0 & 0 & 0 \\ 0 & 0 & 0 & 0 & 5 \cdot 10^{-8} & 0 & 0 \\ 0 & 0 & 0 & 0 & 0 & 5 \cdot 10^{-8} & 0 \\ 0 & 0 & 0 & 0 & 0 & 0 & 3.23 \cdot 10^{-7} \end{bmatrix} \tag{7.1}$$

$$\boldsymbol{Q} = Diagonal(\begin{bmatrix} 100_{1\times4} & 350 & 350 & 2 \cdot 10^{-5}{}_{1\times4} & 1 \cdot 10^{-4} \end{bmatrix}) \tag{7.2}$$

7.2 Straight line acceleration

The straight line study is performed on a straight piece of road. During this experiment, there will be close to zero lateral forces on the vehicle, meaning that only the longitudinal dynamics of the vehicle model will contribute significantly to the states. The velocity profile for the described experiment is shown in Figure 7.1, which contains three acceleration zones, and three braking zones.

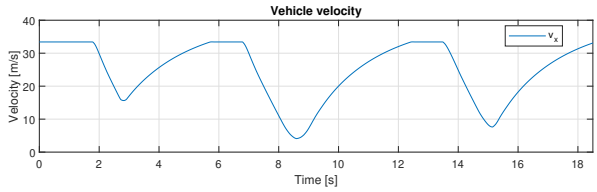

Figure 7.1: Velocity profile for straight line acceleration

7.2.1 Longitudinal forces

The actual longitudinal tyre forces for all four corners, and the Kalman Filter estimates are shown in Figure 7.2. The estimated longitudinal forces follow the true values closely. This is true for steady state acceleration while the transient between the acceleration and braking zones appears to have a small overshoot. It can be seen that the rear tyres have a small dip at the end of the braking zones, most likely caused by the simplified tyre load estimator that does not include transient behaviour.

The error metrics for the experiment are shown in Table 7.1. The results are very similar for tyres on the same axle, while the rear axle has a slightly higher error compared to the front axle. Figure 7.3 show the estimation error for the front left and rear right tyre. Both a stationary deviation is visible, as well as an increased error during braking and the transient dynamics. The stationary deviation is over twice as large for the rear tyre during

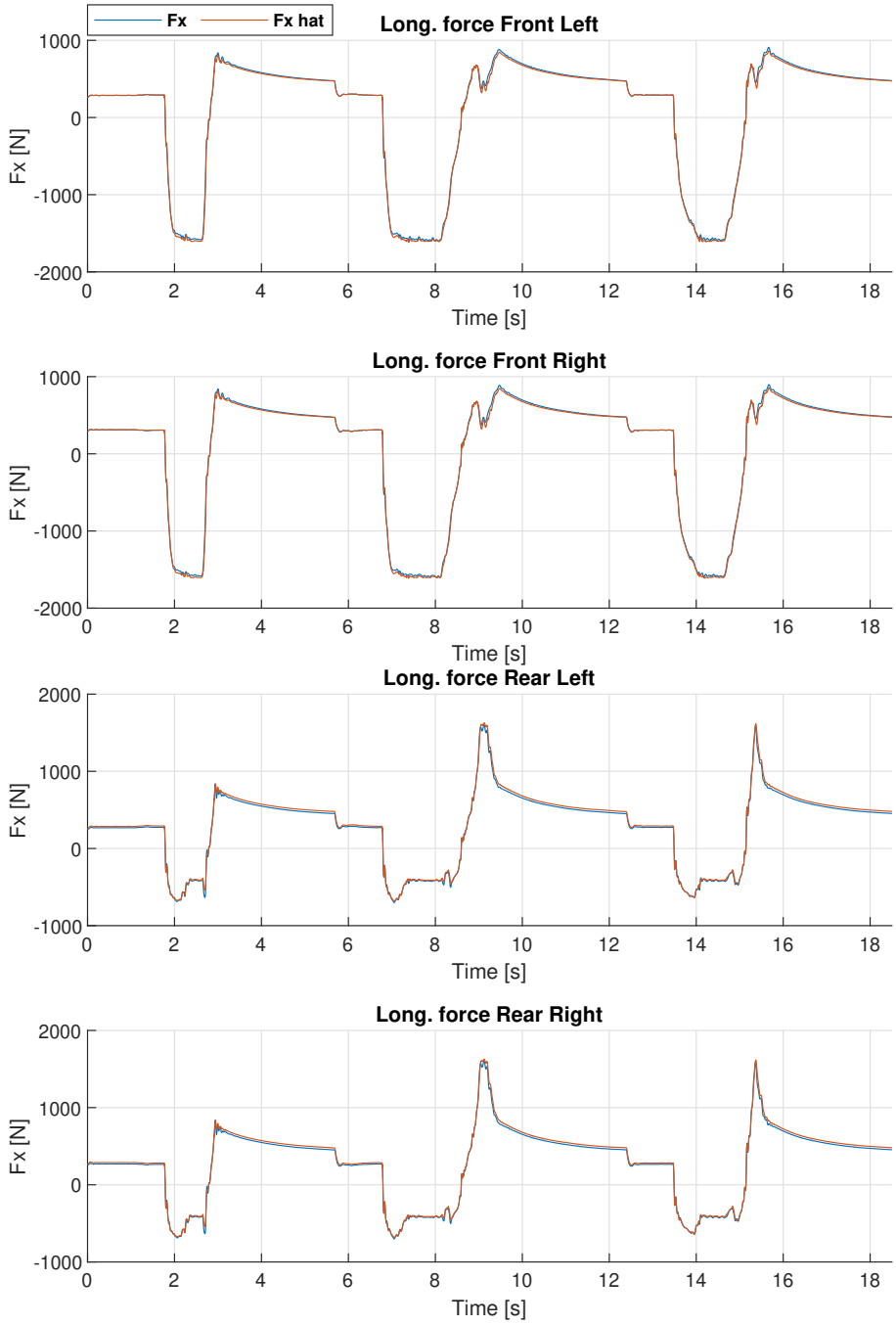

Figure 7.2: Actual vs. estimated longitudinal tyre forces

State	RMSE	MAE
F_x FL	21.7294	14.6695
F_x FR	21.8306	14.971
F_x RL	25.9837	22.2783
F_x RR	25.8237	22.1058
Total F_x	23.9309	18.5062

Table 7.1: F_x error metrics for each corner. [N]

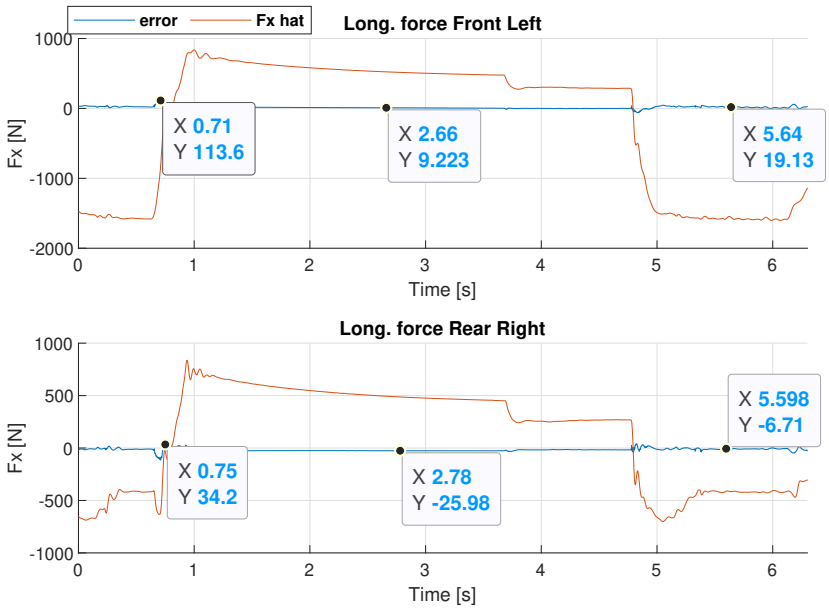

Figure 7.3: Estimation error of Fx for FL/RR diagonal - Straight line acceleration

acceleration, while the front error during braking is almost thrice that of the rear. During acceleration, the rear tyres have a higher tyre load, due to load transfer, while the front tyres experience a higher tyre load during braking. This might explain the different is absolute error in the two scenarios. The deviation around $t = 2.75s$ occurs with a similar F_x of around $500N$. As the resistance from rolling and aerodynamic drag are estimated online, these are not perfect, meaning that the sum of forces will not be accurate. This explains the small deviation for all tyres.

As the estimation error is relatively small, the straight line acceleration should be a feasible experiment for identification of parameters for a longitudinal tyre model. As there are no cornering forces involved, only a pure longitudinal tyre model should be considered.

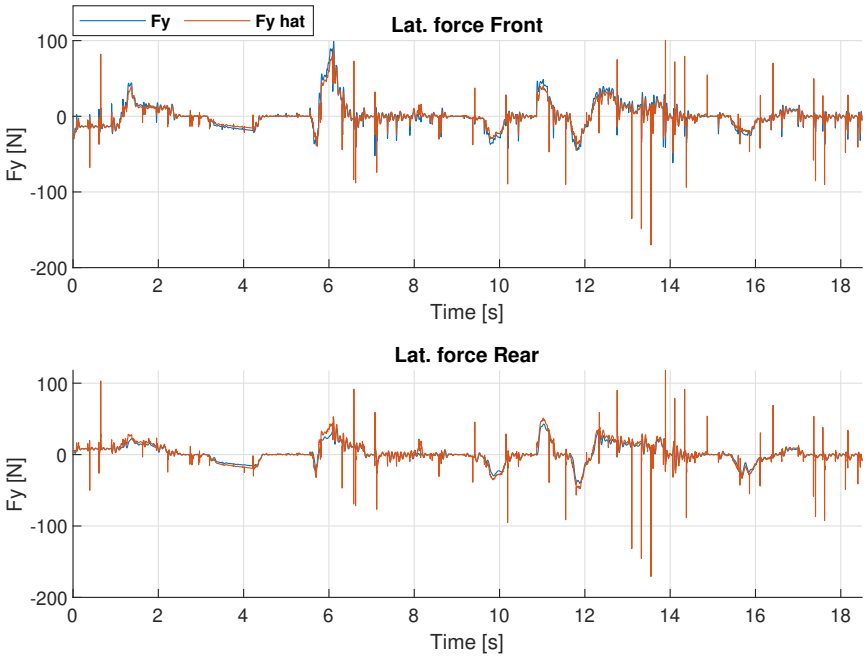

Figure 7.4: Actual vs. estimated lateral tyre forces - Straight line acceleration

7.2.2 Lateral forces

As this experiment does not involve any cornering, the actual lateral tyre forces are very small. Figure 7.4 shows the estimated lateral forces together with the actual forces for each axle. Even though the main dynamics are captured by the estimator, there are a lot of spikes with high amplitude that ruin the accuracy. This will be more closely discussed in Section 7.3.1 as the lateral dynamics are more dominant in the steady-state cornering experiment.

7.3 Steady state cornering

Steady state cornering is tested using a figure eight track. Each circle is driven twice, first two to the right, followed by two to the left. The lateral and rotational dynamics of the race car will be the dominant dynamics in this experiment, while the longitudinal dynamics contribute little.

7.3.1 Lateral forces

The actual and estimated lateral forces for the front and rear axle are shown in Figure 7.5. The estimated forces contain a lot of spikes, with high amplitudes. Even though the estimated force follows the main dynamics of the actual force, the spikes cause the estimated force to be unreliable.

State	RMSE	MAE
F_y front	349.2626	320.6796
F_y rear	366.8641	334.7578
F_y combined	277.4829	85.9255
Total F_y	358.1716	327.7187

Table 7.2: F_y error metrics. [N]

The error metrics for the lateral tyre forces are presented in Table 7.2. The large difference between the RMSE and MAE metrics, especially when combining the two axles, confirms that the estimate contains big overshoots. As the lateral forces are estimated per axle, instead of per tyre, a direct comparison with the longitudinal estimates in Table 7.1 is not possible, nonetheless it is safe to say that the lateral estimates are worse than the longitudinal estimates, and are unsuitable for identification of lateral tyre parameters before this has been improved.

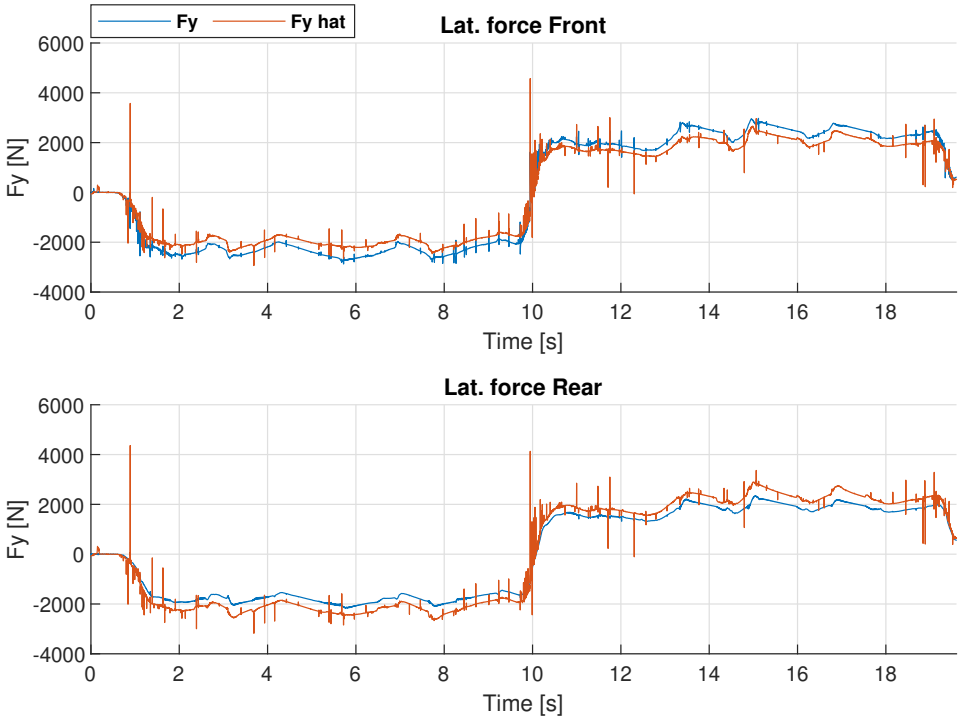

Figure 7.5: Actual vs. estimated lateral tyre forces - Steady state cornering

It is not trivial to pinpoint the cause of the poor estimates. The simplification of combining the two wheels on each axle will cause some of the estimation error, however the main contribution is thought to be the observability of the system. As the lateral tyre forces act with the same sign and arm on the available measurements, and the wheel angles are

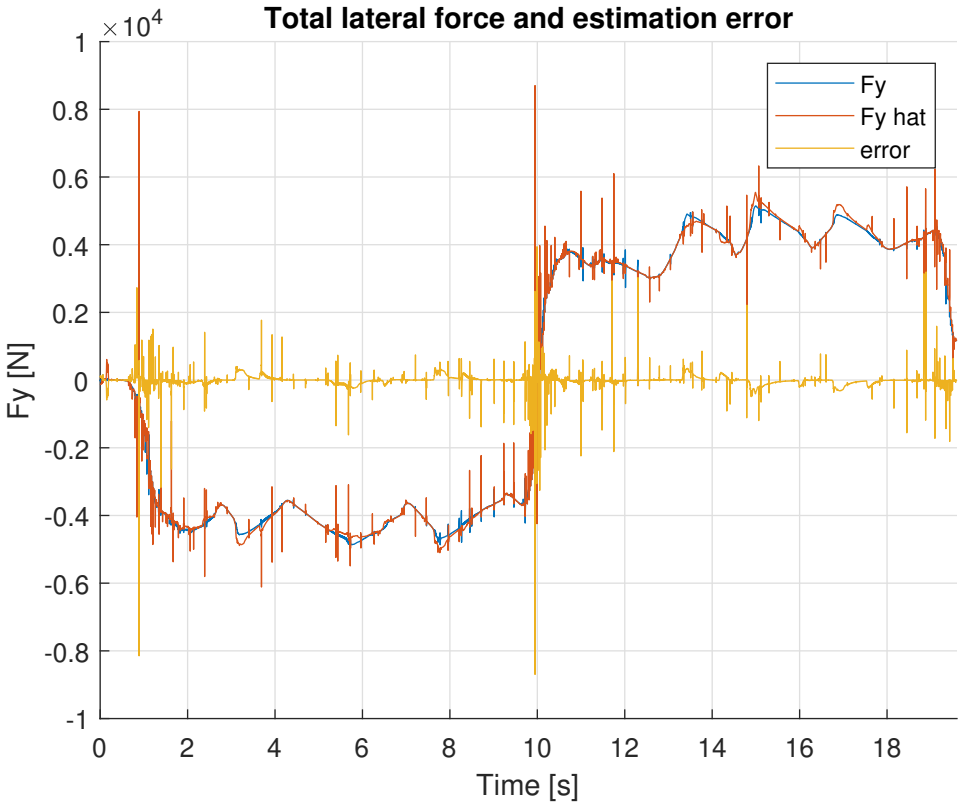

Figure 7.6: Total lateral force and estimation error - Steady state cornering

similar per axle, a singularity can occur causing a loss of observability. It can be seen from the graphs in Figure 7.5 that both the front and rear estimates have big spikes at the same time. This might indicate that the Kalman Filter is struggling observing the states.

The stationary deviation for the front and rear axle have different signs. This also indicates issues with the observability. The results shown in Figure 7.6 present the actual and estimated total lateral force, as well as the total error. It can be seen that the total lateral force is much more accurate than the two individual forces. Ignoring the spikes, we see that the stationary deviation is reduced significantly, indicating that the filter is unable to correctly distribute the lateral force between the two axles.

7.3.2 Longitudinal forces

As the lateral dynamics dominate the race car behaviour during the steady-state cornering, the longitudinal forces small. Figure 7.7 shows the estimated and actual forces during the experiment. The estimated values are accurate for most of the experiment. It can however be seen that the spikes found in the lateral forces also have propagated to the longitudinal estimates. The lateral estimates had big spikes in the time-frame between $t = 8s$ and

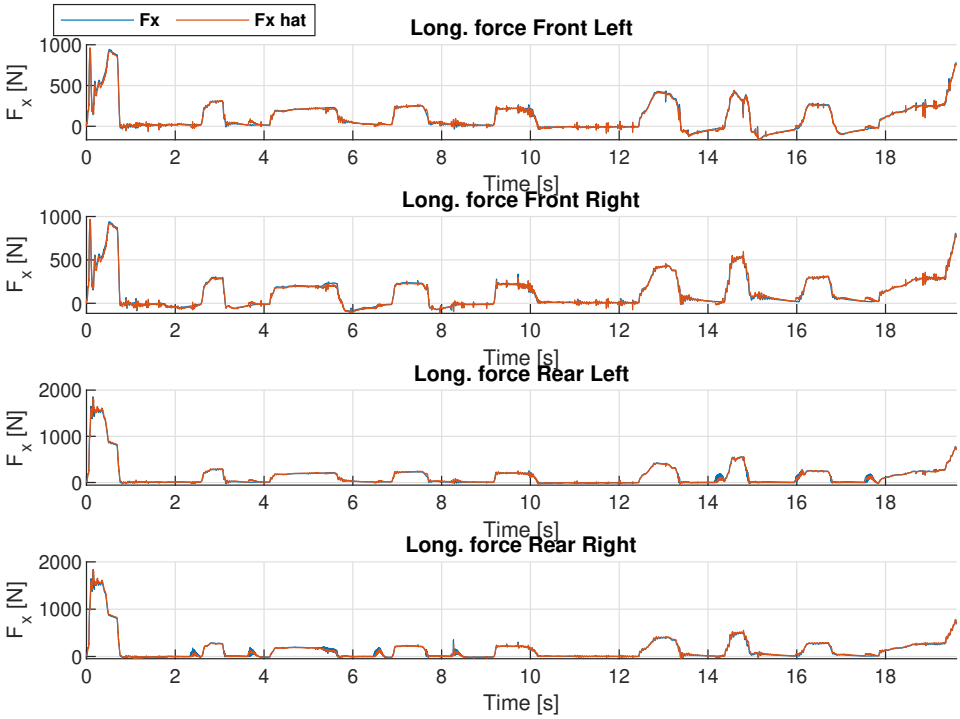

Figure 7.7: Estimated vs. actual longitudinal forces - Steady state cornering

$t = 12s$. These spikes can also be seen in the longitudinal estimates, although they are less extreme.

7.4 Full Circuit

The full circuit experiment tests the combination of all dynamics of the Kalman Filter. During the lap, the race car experiences various corner types, straight, trail braking and straight braking zones, meaning all dynamics will play an important role for the state estimation. The velocity profile of the circuit is shown in Figure 7.8. The experiment was carried out over several laps, where the second to last lap is used for the results in this section. The track layout is as described in 6.3.

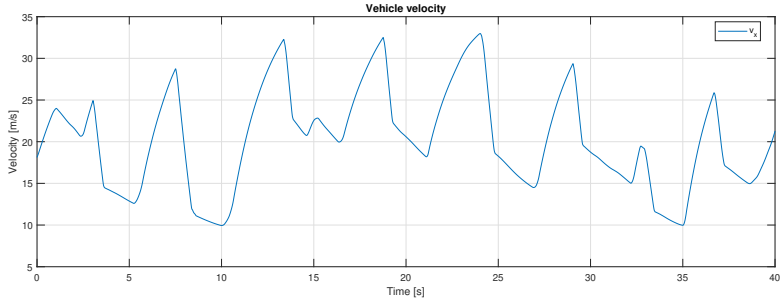

Figure 7.8: Velocity profile for the full circuit

7.4.1 Longitudinal forces

The estimated longitudinal forces for each tyre are shown in Figure 7.9. The results are very similar to the ones presented in Section 7.2.1. The estimated forces follow the true value closely. The error metrics are presented in Table 7.3. There is a small increase in both metrics compared to the straight line acceleration results. Looking at the rear tyres, it can be seen that the tyre behaviour during braking is less smooth. This is due to the load transfer unloading the rear tyres during braking. As braking on a full circuit usually happens into a corner, the tyre capacity is lower than in a straight line due to the friction circle. The slip angle from turning into the corner generates a lateral tyre force that uses tyre capacity. There are also some small spikes visible on the rear tyres at the end of each braking zone.

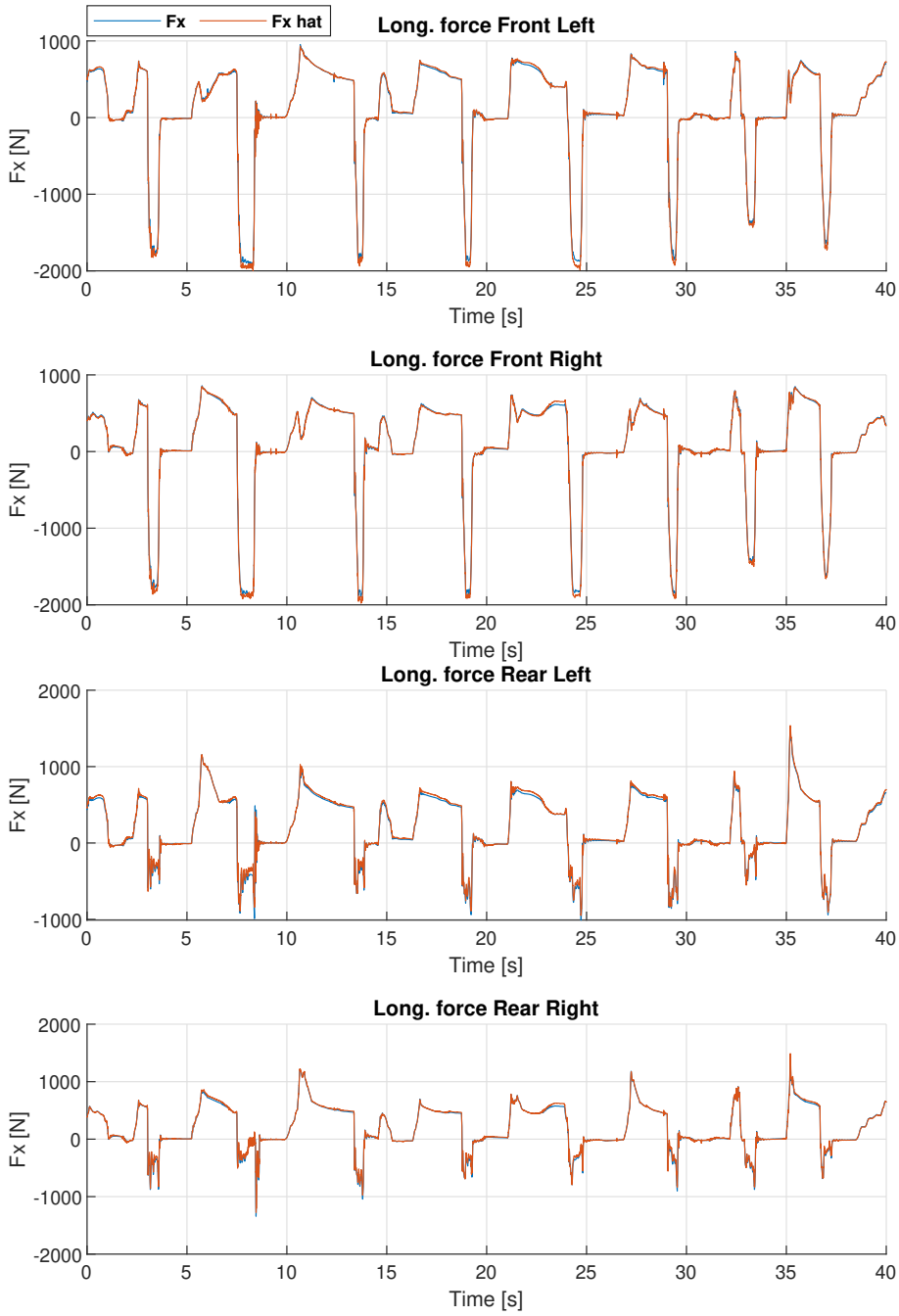

Figure 7.9: Actual vs. estimated longitudinal tyre forces

State	RMSE	MAE
F_x FL	25.2721	15.5521
F_x FR	22.777	13.7675
F_x RL	26.7065	17.8886
F_x RR	27.6674	14.6271
Total F_x	25.6719	15.4588

Table 7.3: F_x error metrics for each corner. [N]

7.4.2 Lateral forces

The estimated lateral forces are presented in Figure 7.10. A visual comparison with the results from the steady state cornering experiment show an improvement in the lateral estimates. The amount of spikes has been reduced significantly. The full circuit experiment has all dynamics present, meaning that there is more information available to the filter. In addition to the yaw and lateral acceleration, the longitudinal acceleration can now also be used to estimate the lateral tyre forces. There are still some spikes present, with extreme high amplitudes.

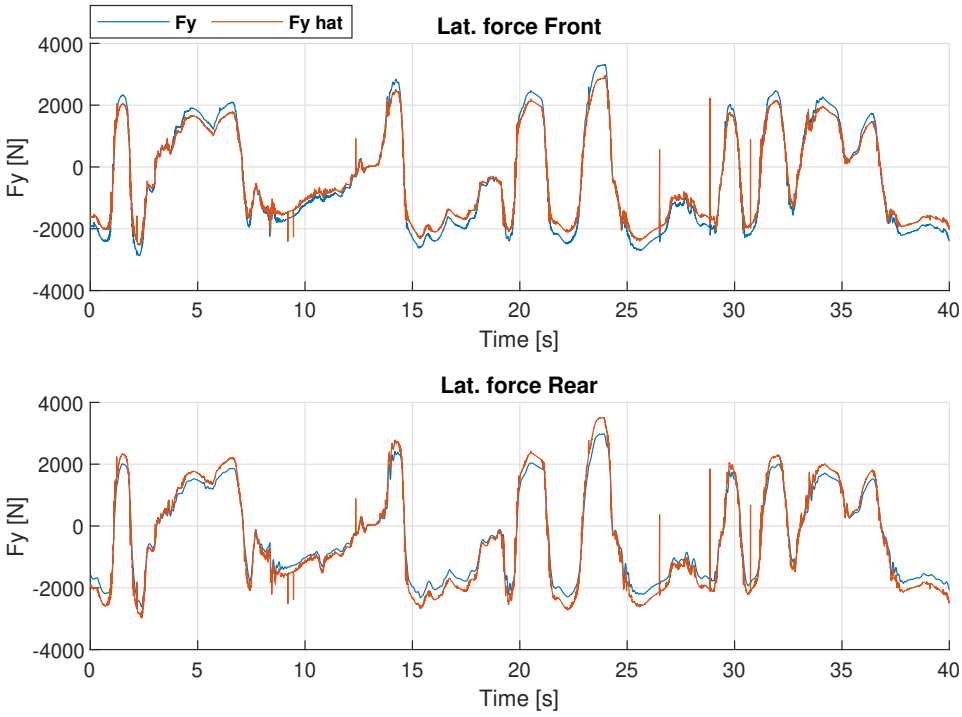

Figure 7.10: Actual vs. estimated lateral tyre forces - Full circuit

The error metrics for the lateral tyre forces are presented in Table 7.4. A comparison

State	RMSE	MAE
F_y front	252.748	222.7022
F_y rear	264.8218	233.3897
F_y combined	128.5651	39.201
Total F_y	258.8553	228.046

Table 7.4: F_y error metrics. [N]

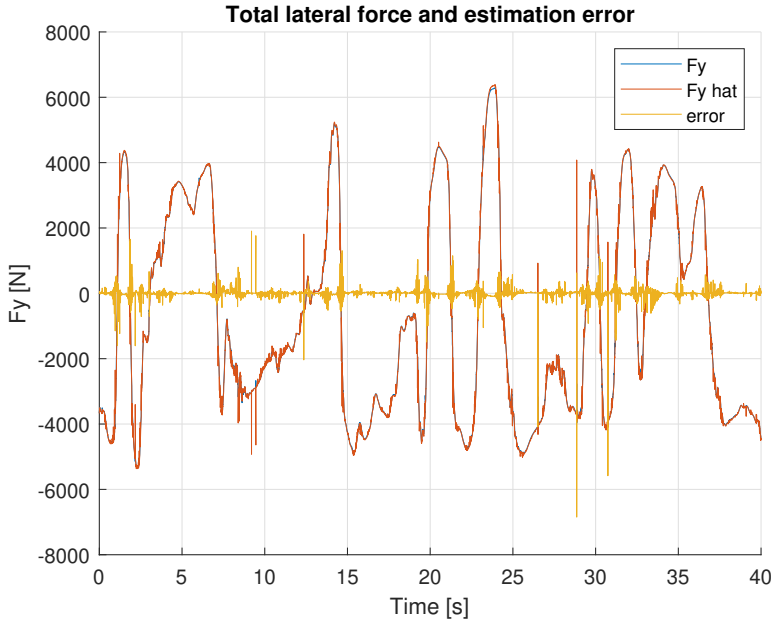

Figure 7.11: Total lateral force and estimation error - Full circuit

with Table 7.2 confirms that the lateral estimates have improved. The estimation error for the front and rear axle follow the same pattern as during the steady state cornering, where the front and rear are under- and overestimated respectively. Figure 7.11 shows the combined lateral force from both axles, and the estimation error. Just like in the steady state cornering experiment, the total lateral force follows the true value closely, besides the spikes occurring at certain intervals. The estimated lateral forces can not be used directly for tyre model estimation, as the spikes will have to be handled first.

Chapter 8

Results and Discussion - Parameter estimation

The results of the online tyre parameter estimation is presented in this chapter. This includes the results from the data-selection algorithm and the parameter estimation for both the brush tyre model and the magic formula tyre model. The parameter estimation will be evaluated for the accuracy of the tyre-road friction estimate, and the overall tyre model accuracy. First, the results of a straight line acceleration experiment will be presented, as the pure longitudinal nature of this experiment makes it the most suitable for the estimation of parameters for a pure longitudinal tyre model. The last sections of this chapter will present and discuss the results of a full circuit experiment, where an increase in friction is simulated, using the straight line acceleration results as an initial guess. This simulates the events of a competition, and can give insight into the online grip estimation.

8.1 Data selection algorithm

The goal of the data selection algorithm is to ensure that the estimation scheme has sufficient knowledge of the tyre behaviour to reliably estimate the tyre parameters. Figure 8.1 shows the distribution of the final data-set of a straight line acceleration experiment. Over the course of the experiment, the selection algorithm has managed to find datapoints for most of the bins. As expected, the high tyre load bins are empty for negative slip ratios, as there is to much grip at high tyre loads to lock the wheels. The final bin distribution is able to capture datapoints for most of the vehicles operating conditions.

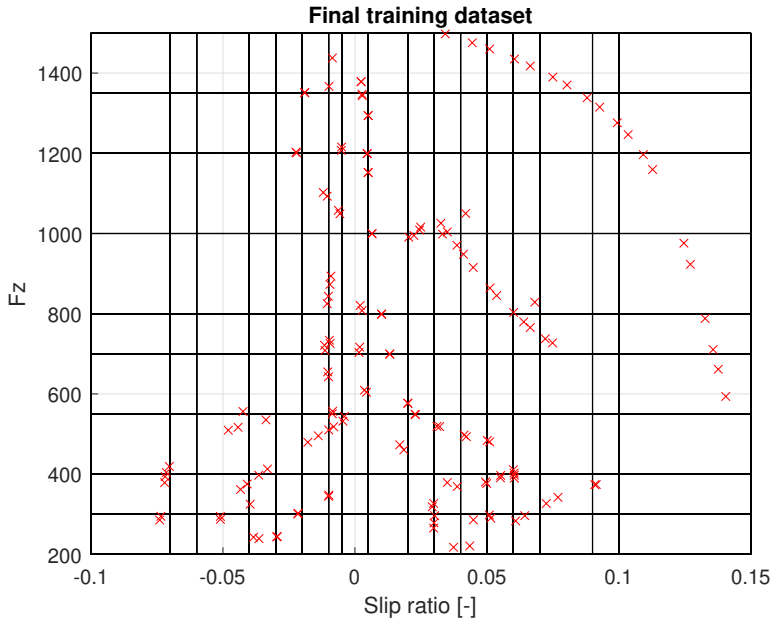

Figure 8.1: Final distribution of training data after simulated straight line accelerations

In order to help prevent the solver from converging to a sub-optimal solution due to a lack of excitation, a minimum amount of datapoints need to be collected before the solver is started. Figure 8.2 shows the accumulation of datapoints, and the velocity of the vehicle during the simulation. The results in this chapter used a threshold of 100 datapoints, which is reached at $t = 12.75s$. The threshold needs to be balanced, in such a way that it is reached relatively quickly without converging to a sub-optimal solution. A high threshold might mean that it won't be reached, while a low threshold can lock the solver in an early local minimum that does not match with later encountered tyre behaviour. During the simulation not all bins were filled, and the last new bin was filled at $t = 42.9s$. The simulation ended with 153 datapoints in the data-set.

8.2 Tuning

There are two parameters that can be tuned for the gradient method solver. The step-size Γ and the initial estimate θ_0. The tuning was done experimentally, looking at convergence rate and stability. Just as in the project thesis, the gradients are very steep, meaning that a very small step-size was requires. The final Γ values, for both the brush and magic formula are given in Equations 8.1 and 8.2.

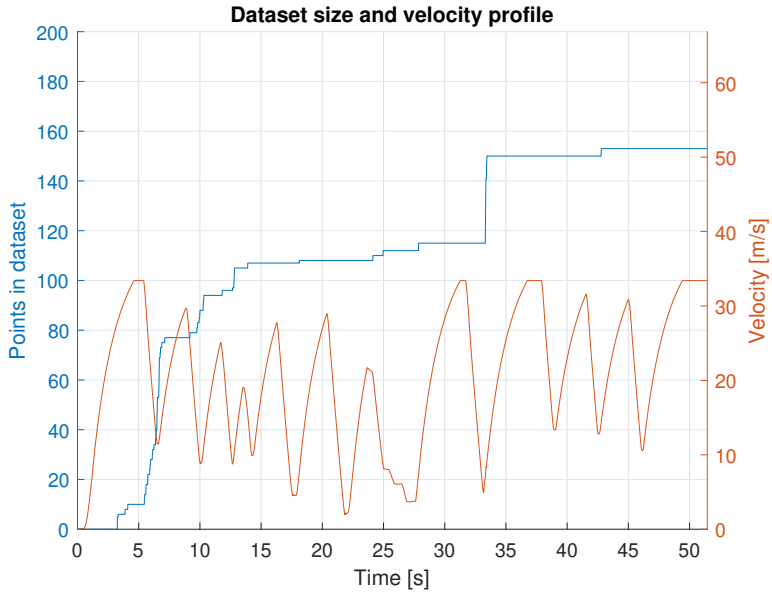

Figure 8.2: Data-set size and vehicle velocity.

$$\Gamma_{brush} = 2 \cdot 10^{-7} \begin{bmatrix} 1 & 0 & 0 & 0 \\ 0 & 0.4 & 0 & 0 \\ 0 & 0 & 0.4 & 0 \\ 0 & 0 & 0 & 0.4 \end{bmatrix} \tag{8.1}$$

$$\Gamma_{mf} = 9 \cdot 10^{-7} \begin{bmatrix} 2 & 0 & 0 & 0 & 0 & 0 & 0 & 0 \\ 0 & 7 & 0 & 0 & 0 & 0 & 0 & 0 \\ 0 & 0 & 3 & 0 & 0 & 0 & 0 & 0 \\ 0 & 0 & 0 & 1.7 & 0 & 0 & 0 & 0 \\ 0 & 0 & 0 & 0 & 120 & 0 & 0 & 0 \\ 0 & 0 & 0 & 0 & 0 & 200 & 0 & 0 \\ 0 & 0 & 0 & 0 & 0 & 0 & 100 & 0 \\ 0 & 0 & 0 & 0 & 0 & 0 & 0 & 4000 \end{bmatrix} \tag{8.2}$$

The initial estimate of the normalised parameters are given in Equation 8.3. These should be changed throughout the racing season, as the estimator has identified the values for a given road/tyre combination. The final estimates after testing days should be saved and labeled with track conditions and tyre type. They can then be used as good initial guesses when the conditions are similar at a later stage.

$$\theta_{0_{brush}} = \begin{bmatrix} 5 & 2 & 1.5 & -1 \end{bmatrix}^T \tag{8.3}$$

$$\theta_{0_{mf}} = \begin{bmatrix} 1 & 1 & 1 & 2 & -0.2 & 4 & 0 & 0 \end{bmatrix}^T \tag{8.4}$$

8.3 Tyre-road friction estimate

Achieving an accurate estimate of the tyre-road friction coefficient is the primary goal of this thesis. In this section, the parameter development and convergence will be presented, in addition to an evaluation of the accuracy of the final friction estimates. The same load dependency friction model, shown in Equation 8.5 is used in both models. For the brush tyre-model, the parameters are referred to as μ_a and μ_b, while for the magic formula they are D_a and D_b. The simulation environment uses an identical friction model, and is shown with coefficient values in Equation 8.6. F_{z_0} is chosen to be

$$f_z = \frac{F_z - F_{z_0}}{F_{z_0}}$$

$$\mu_x(F_z) = \mu_a + \mu_b \cdot f_z \tag{8.5}$$

$$\mu_{x,true}(F_z) = 1.9297 - 0.2397 \cdot f_z \tag{8.6}$$

8.3.1 Convergence

Before evaluating the final friction estimate, the parameter development over the course of the experiment will be presented. Both models were given the same data-set, and were ran in parallel. In addition to the parameter development, the true value is shown as reference.

8.3.1.1 Brush tyre model

The parameter development for the brush-model is presented in Figure 8.3. As the data-set size threshold is reached, the parameters quickly develop towards the final value. However, the first steps do overshoot. As the data-set increases in size, the parameters converge to their final value around $t = 34.5s$. Looking at the velocity profile and training set size in Figure 8.2, we see that this coincides with the last big jump in new training points. After this event, the parameters stabilize at their final values. The biggest change before the stabilization occurred in the μ_b parameter, which changed sign. As this parameter controls the tyre-load sensitivity of the tyre model, this can be explained with the braking manoeuvre that is performed at this time. This is the first hard braking from top speed all the way down to $5m/s$. This provides the model with low tyre load data for the rear wheels, as the load transfer releases the rear tyre load and the low speed reduces the aerodynamic downforce. After this braking event, the parameters have converged, and are unaffected by the final acceleration zones that follow, indicating that a local minimum has been found.

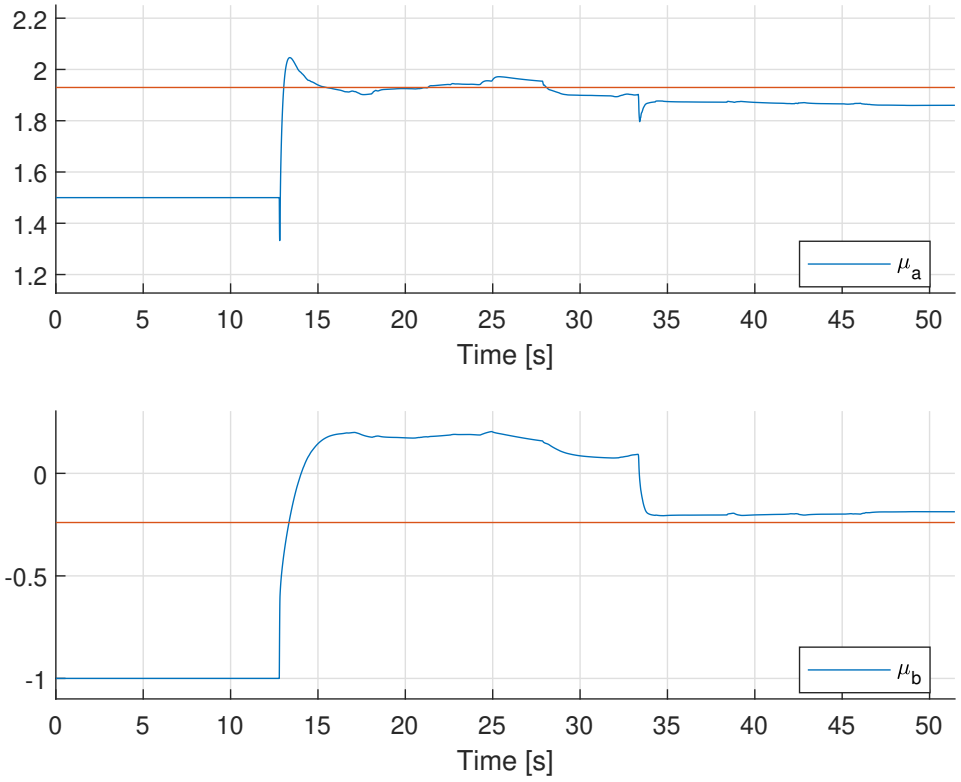

Figure 8.3: Friction parameter development for the brush tyre model

8.3.1.2 Magic formula tyre model

Compared to the parameter development of the brush tyre model, the magic formula friction parameters are less stable. The parameter development is presented in Figure 8.4. Like the brush model, the magic formula model also made a large step after the final hard braking event. Before this, only the D_a parameter showed signs of stability. This is another indication of lacking variety in F_z in the data-set. Unlike the brush model, that stabilized after the after $t = 34.5s$, the following accelerations still have an effect on the parameters. As the magic formula model has a higher amount of parameters, a lack of convergence for the remaining parameters can be the cause of this. This will be discussed in Section 8.4.2.1.

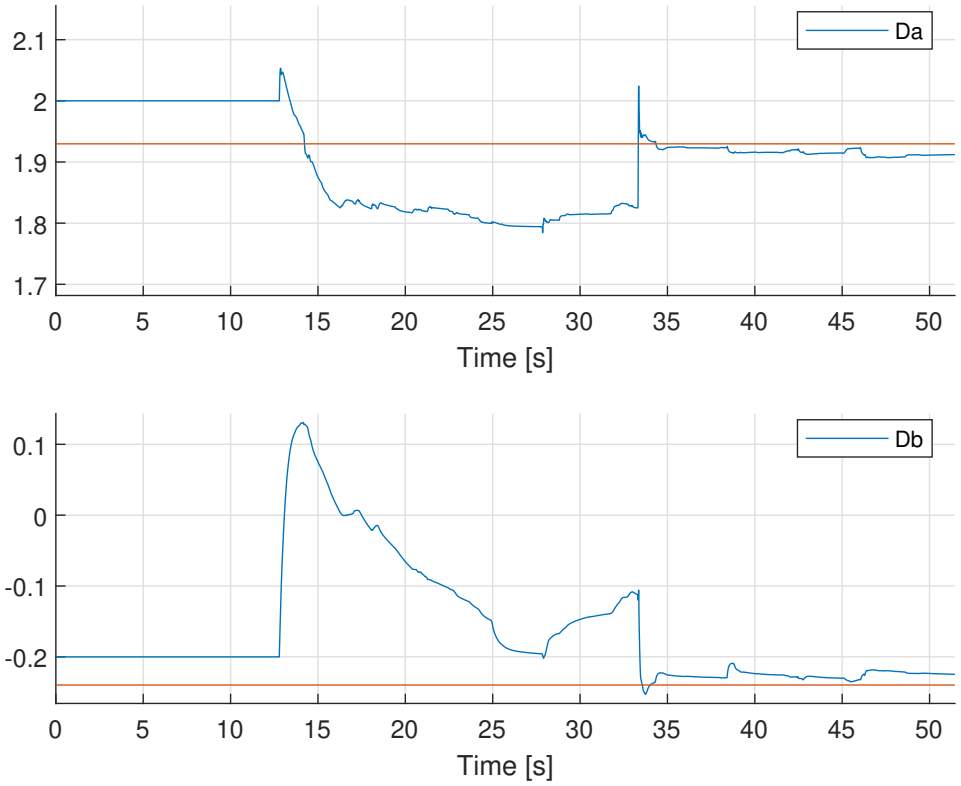

Figure 8.4: Friction parameter development for the magic formula tyre model

8.3.2 Final friction estimate

$$\mu_{x,brush} = 1.8602 - 0.1872 \cdot f_z \tag{8.7}$$

$$\mu_{x,MF} = 1.9121 - 0.2246 \cdot f_z \tag{8.8}$$

The final estimated friction models are given in Equation 8.7. Figures 8.3 and 8.4 showed that neither of the models found the perfect solution. The estimated models, together with the true friction coefficient are shown in Figure 8.5. In addition to the friction coefficient, the total time spent at a given F_z for a race on a full circuit lasting 76 seconds is shown. The purpose of the estimated friction coefficient is to provide the TV control system with an accurate force constraint for each wheel. This works as the traction control of the vehicle, aiming to maximise longitudinal tyre force, without excessive wheel-spin. Maximum available grip is given by $F_{x_{max}} = \mu F_z$. Underestimating the friction coefficient will make the controller less aggressive than possible, meaning performance is lost due to not utilising all available grip. An overestimated friction coefficient will lose performance from two phenomenon. Firstly, the longitudinal tyre force is smaller than at peak performance, and secondly performance is lost as the tyre goes from rolling to sliding. This

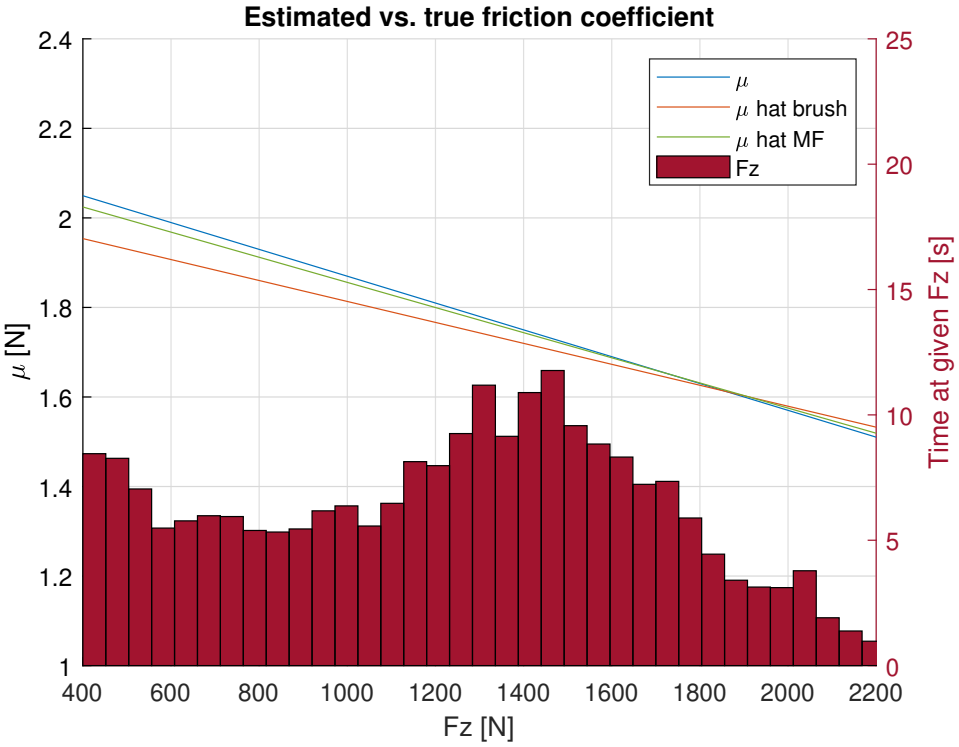

Figure 8.5: Estimated tyre-road friction coefficient vs. actual friction coefficient

causes extensive tyre wear and requires the driver to lift off the throttle to regain control. With this in mind, it might be favourable to have a slightly underestimated friction coefficient opposed to a slight overestimated. This safety factor should however be implemented in the control system, not in the parameter estimation scheme.

Figure 8.5 shows that both estimated models underestimate the friction coefficient. The magic formula is the closest to the true friction value, while the brush model lacks accuracy both in terms of scale and load sensitivity. For the lowest F_z values, the brush models underestimates with over 5%. The tyres experience tyre loads in the range $1200N$ to $1600N$ for the majority of the race. In this range, both models are pretty accurate, with the brush model underestimating the most. In addition to being constraint by the available grip for each tyre, there are other constraints like available motor force and the overall power limit from the accumulator that limit the vehicle performance. The grip is usually the limiting factor for lower F_z ranges. It is in this area that the brush model performs the worst, making the magic formula the favourable model with regards to friction estimation. This is to be expected, due to the simplifications in the brush model making it unable to capture the drop-off as the slip-ratio surpasses the peak value. Instead of bending down, the brush model stays level from peak slip and outwards. This means that datapoints gathered for slips beyond peak slip will contribute to the reduction of the friction coefficient in

order the minimize the least squares error for all datapoints. The magic formula is capable of dropping off after peak slip, meaning that the friction coefficient isn't required to be lowered.

8.4 Full tyre model accuracy

The secondary goal of this thesis is to acquire a longitudinal tyre model for the new Hoosier tyres. Besides the friction coefficient discussed earlier, the models contain parameters for tyre stiffness and the overall shape of the F_x curves. These will be evaluated in this section.

8.4.1 Brush tyre model

As the brush tyre model only consists of four parameters, it is expected to converge better than the magic formula tyre model. The four parameters consist of two pairs, one for the tyre friction coefficient, and one for the tyre stiffness. Both are affected by different slip ranges, meaning that in order for the model to converge, data from the range around zero slip ratio, and from the range around peak performance needs to be acquired. Since there is no capability to model the drop-off with the brush model, data from excessive slip conditions is less valuable and might even reduce the accuracy, as discussed in Section 8.3.2.

8.4.1.1 Convergence

The stiffness parameter of the brush tyre model has the same tyre load dependent model, shown in Equation 8.9 as the friction coefficient. The stiffness of the tyre mainly affects the linear section of the tyre model, around zero slip ratio. As the tyre model in the simulation environment is much more complex, no true value for the parameters could be extracted.

$$\begin{aligned} f_z &= \frac{F_z - F_{z_0}}{F_{z_0}} \\ Cx(F_z) &= C_{x_a} + C_{x_b} \cdot f_z \end{aligned} \tag{8.9}$$

The development of the stiffness parameters C_{x_a} and C_{x_b} is presented in Figure 8.6. Just like the friction parameters, a big jump towards the final value is made right as the data-set threshold is reached. As data around zero slip ratio is readily available, and not dependent on specific braking manoeuvres, the parameters converge faster than the friction parameters. Despite this, there is a small amount of drift left in the parameters. This can be because of the many simplification of the tyre model, meaning there is no constant value for these parameters to capture all dynamics it is encountering. The final value for $\hat{\theta}_{mf}$ is presented in Table 8.1.

Tyre parameter	Final estimate
C_{x_a}	8.0548
C_{x_b}	0.9449
μ_a	1.8602
μ_b	-0.1872

Table 8.1: Final parameter values for brush tyre model

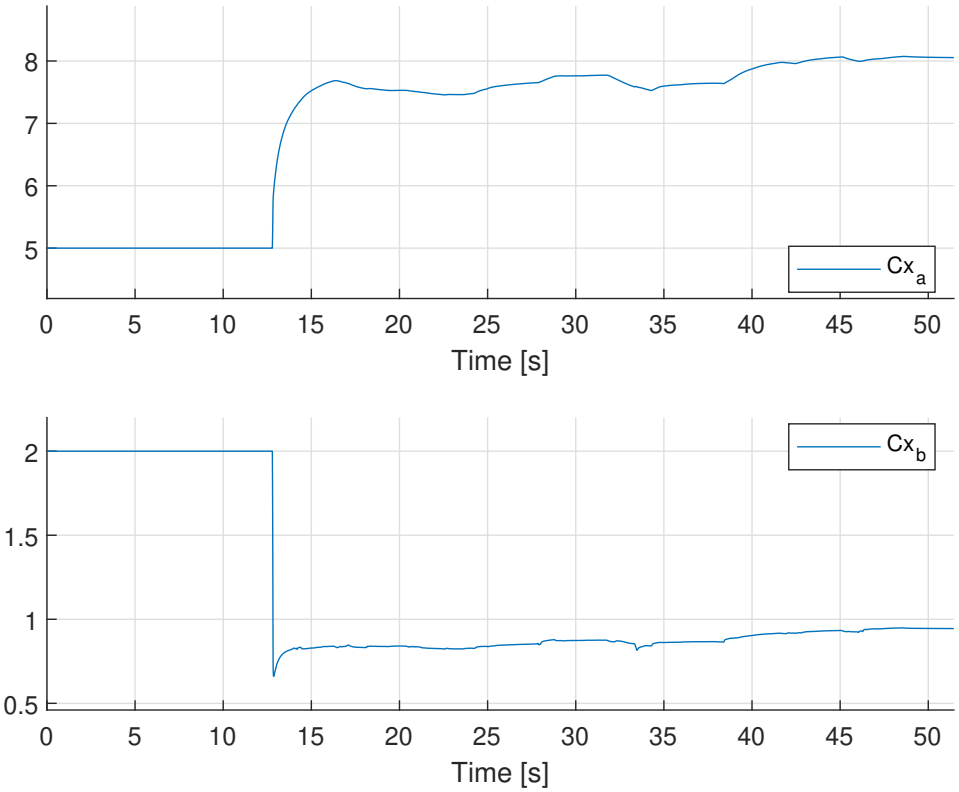

Figure 8.6: Brush tyre model stiffness convergence

8.4.1.2 Final tyre model

The final estimated brush tyre model, for a selection of tyre loads is presented in Figure 8.7. At first glance, the model's accuracy is a lot better than the results from the project thesis [12]. The lack of drop-off is visible, especially for positive slip ratios. The stiffness around zero slip ratio is matching well. Zooming in on the low and high slip area allows for better view of the model performance. Figure 8.8a shows the low slip range of the model. The estimated model matches the true model for the entire F_z range. The high slip range, both positive and negative, are shown in Figure 8.8b. A difference between

the positive and negative side is visible, with the model performing better under braking. This is because of the asymmetrical tyre model in the simulation environment. As the brush model is symmetrical, the friction coefficient will try to adjust for both braking and acceleration, and end up somewhere in between.

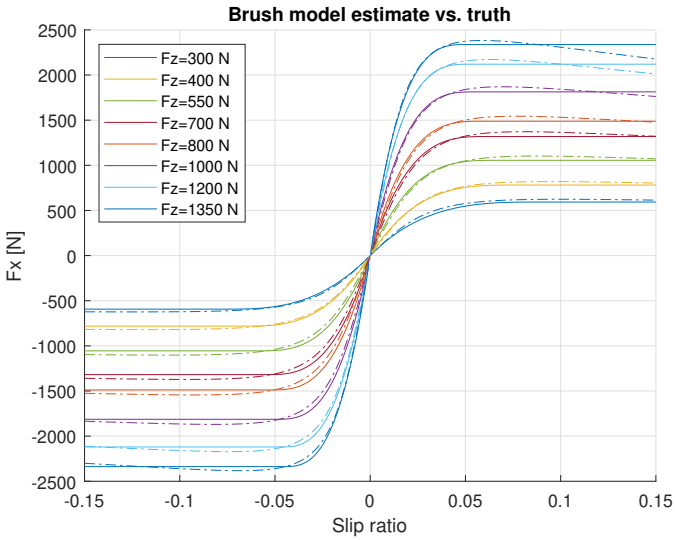

Figure 8.7: Final estimated Brush tyre model

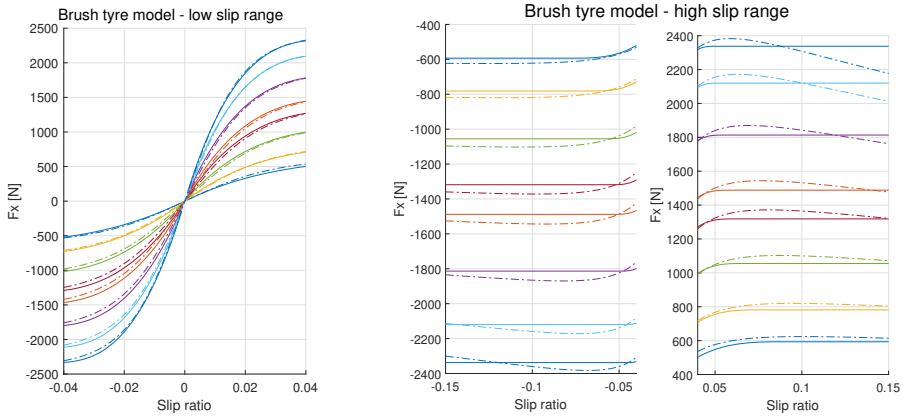

(a) Low slip accuracy

(b) High slip accuracy

Figure 8.8: Brush tyre model - Zoomed in on high and low slip ranges

8.4.2 Magic formula tyre model

The simplified magic formula used for the parameter estimation has the capability to capture the drop-off effects at higher slip that the brush model is not. It does however use twice as many parameters, that will increase the required amount of excitation to converge. The friction coefficient has already been discussed in Section 8.3.1.2. In this section, the full model convergence and accuracy will be discussed.

8.4.2.1 Convergence

Besides the friction parameters, there are six parameters included in the simplified magic formula tyre model. The B parameters are similar to the stiffness parameters of the brush model, and control the shape near zero slip ratio. The C and E parameters control the shape of the F_x curves, allowing for tyre drop-off. Figure 8.9 shows the parameter development for these six parameters.

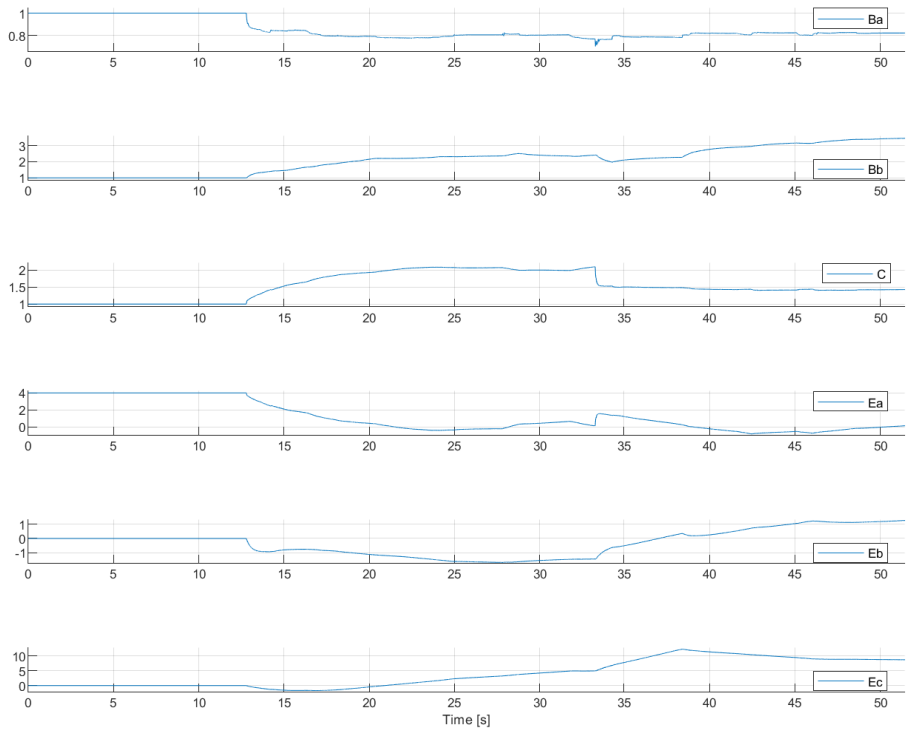

Figure 8.9: Tyre model parameter convergence - magic formula

Compared to the parameter development of the brush tyre model, these parameters are

Tyre parameter	Final estimate
B_a	0.8217
B_b	3.4496
C	1.4240
D_a	1.9121
D_b	-0.2246
E_a	0.1287
E_b	1.2696
E_c	8.7195

Table 8.2: Final parameter values for magic formula tyre model

taking longer to converge. The E parameters seem to struggle the most. One of the simplifications made to the MF 5.2 model was the removal of asymmetrical curves. As the drop-off for positive and negative slip ratios is different, the model won't be able to find a perfect solution, meaning it will struggle to converge. The only two parameter that, in addition to the friction parameters, have truly stabilized are B_a and C. The final value for $\hat{\theta}_{mf}$ is presented in Table 8.2.

8.4.2.2 Final tyre model

The final estimated model is presented in Figure 8.10. Overall, the model has a good accuracy. The drop-off is captured, although not perfectly. Positive high slip is more accurate than braking, which is as expected, as there are no high negative slip datapoints in the data-set. The estimated stiffness is a little higher than the actual stiffness, especially for higher tyre loads.

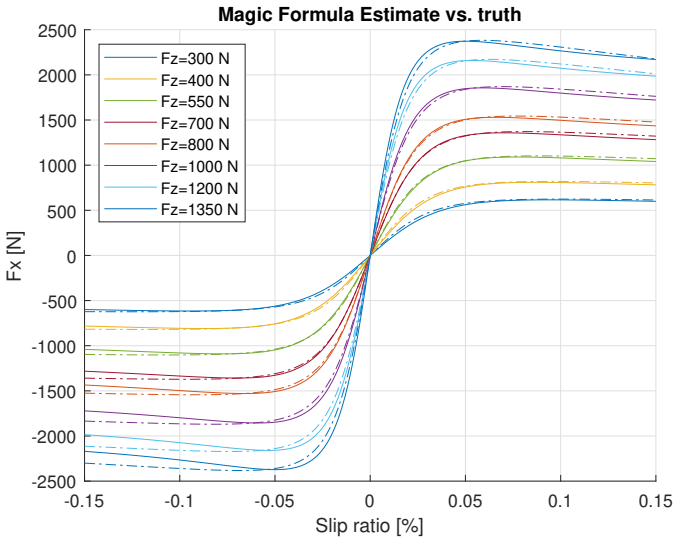

Figure 8.10: Final estimated magic formula tyre model

The low and high slip ranges are focused in Figures 8.11a and 8.11b. As stated earlier, the stiffness is overestimated slightly. The positive high slip range is a lot more accurate than the brush tyre model was able to achieve. The negative range is however a lot worse, especially for the high negative slip ratios. The lack of asymmetrical capability of the simplified model is the cause of this inaccuracy. As the drop-off is modeled as a second order polynomial including tyre load, and there are no high tyre load datapoints for negative slip, the positive high slip ratios will dictate the shape of the curve.

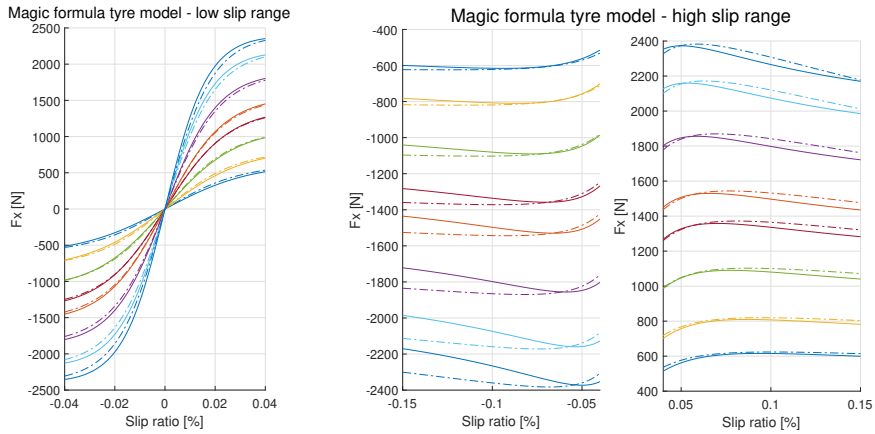

(a) Low slip accuracy

(b) High slip accuracy

Figure 8.11: Magic formula tyre model - Zoomed in on high and low slip ranges

8.5 Full circuit

As a tyre model has been found online, it needs to be tested during a race as well. As straight line accelerations are limited to pure longitudinal dynamics, it does not test the system in action on a full circuit. Therefor another experiment was carried out, using the fitted tyre models from Sections 8.4.1.2 and 8.4.2.2 as the initial guess. The road friction was increased by 10%, so that the online estimator has to adjust based on data gathered during the race. Two approaches were tested. The estimator using the brush tyre model was allowed to iterate on all parameters, both for stiffness and friction. The magic formula tyre model was only allowed to iterate on the friction parameters, using the assumption that the other parameters are unaffected by the changing track conditions.

8.5.1 Data selection algorithm

The operating conditions of a racecar are very different during a full circuit event or a straight line acceleration. The final data-set from the full circuit event is given in Figure 8.12. It shows that the bins for positive high slips are empty. The high negative slip bins have datapoints for low tyre loads. The estimation schemes have a lot less information available, especially for the positive slip range. The threshold for this simulation was set

to 100 datapoints. This was reached after $32.8s$. The final data-set contains 124 datapoints, with the last new bin filled after $188.3s$. The velocity profile and growth of the data-set is shown in Figure 8.13.

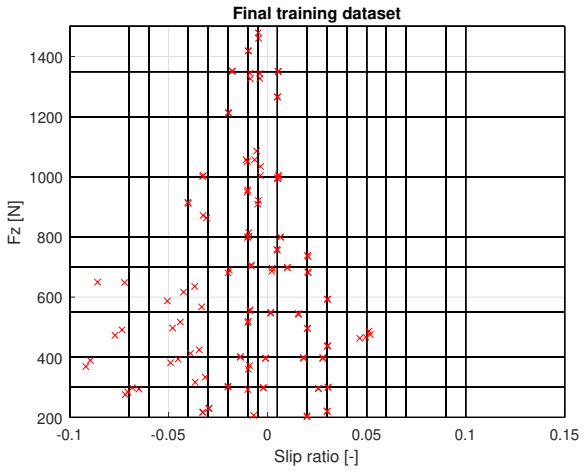

Figure 8.12: Final data-set for full circuit event

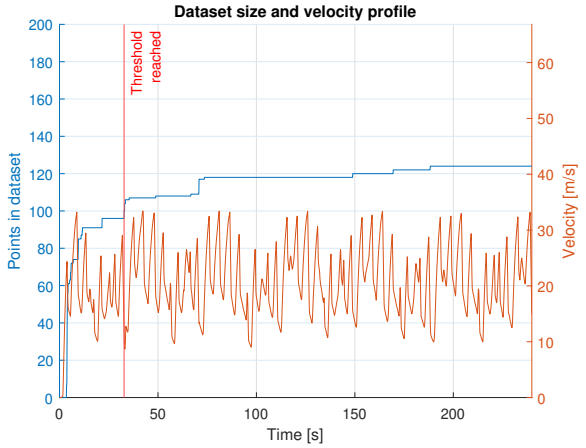

Figure 8.13: Velocity profile and data-set size for full circuit event

8.5.2 Full brush model iteration

The brush model used the same Γ as in Section 8.4.1 in the parameter update law. Using the results from the straight line acceleration experiment, the friction coefficient was only off by 10% as the simulation is started. The results are judged on convergence of the parameters and the accuracy of online estimated grip, which is defined in Equation 2.18, where the later is the most important.

8.5.2.1 Convergence

The development of the model parameters is presented in Figure 8.14. None of the four parameters are converging to a final value, and all are increasing and decreasing over time. The friction parameters are diverging from the true values. Instead of increasing the overall friction parameter, μ_a to capture the increased friction, the load sensitivity parameter μ_b is increased. The stiffness parameters should not be affected much by the change in road friction, but are also varying throughout the simulation.

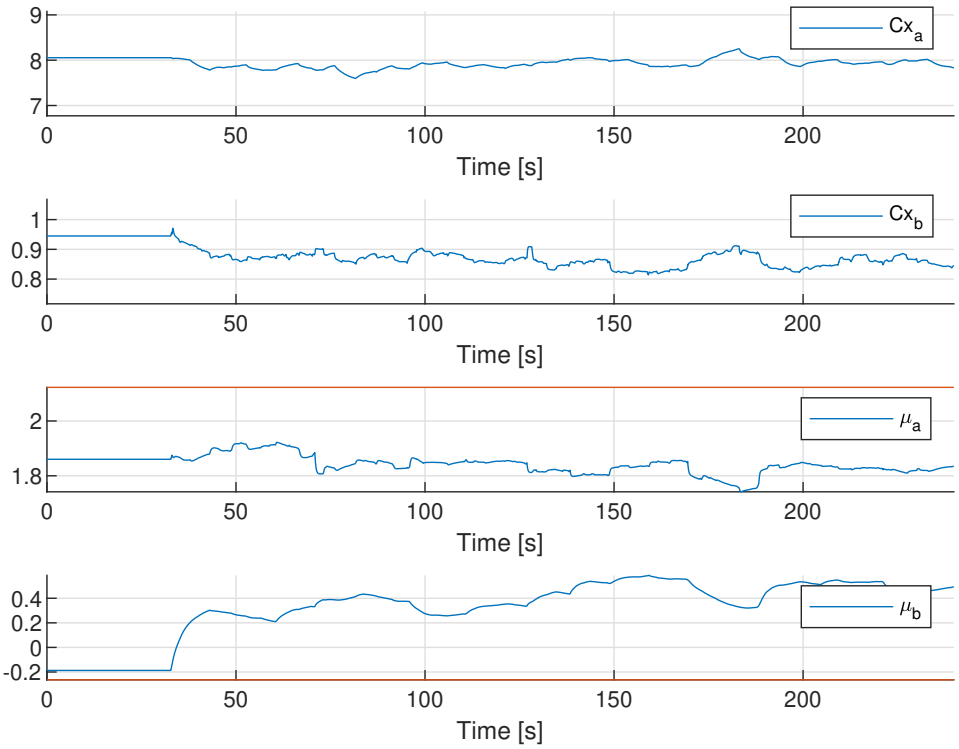

Figure 8.14: Parameter development for brush model parameters

There are two explanations for the lack of parameter convergence, a lack of excitation and the interference from the tyre slip angle. As there is no information about high slip at high tyre loads available for the estimation scheme, the model is over-fitted to fit low tyre loads. By changing the sign of μ_b, the friction coefficient is increased for lower tyre loads. Information about tyre behaviour for entire F_z range is crucial to get the load sensitivity parameters C_{x_b} and μ_b correct.

Over the course of a full circuit, the vehicle has to go through numerous corners. As the car turns, a slip angle in all four tyres is formed. This means that the tyre's longitudinal capacity is decreased due to the lateral force induced in the contact patch. This lowers the longitudinal force for a give slip ratio and tyre load. Higher slip angles decrease the

longitudinal force more than low slip angles. As the data selection algorithm does not take slip angles into account, the magnitude of F_x data gathered can vary drastically within the same bin. This phenomenon is especially in effect around zero slip ratio, as the corners with most slip angle are taken without any throttle input from the driver but is present every time the vehicle is turning.

8.5.2.2 Online friction estimate

The estimated parameters are used to give an online estimated of the grip for each tyre. This is calculated as shown in Equation 8.10.

$$F_{x_{max}} = (\mu_a + \mu_b \cdot f_z)F_z \tag{8.10}$$

Before the training threshold is reached, the initial guess is used to estimate the grip. Figure 8.15 shows that the estimated grip is underestimated for all four tyres. The increase is friction compared to the straight line track is clearly visible in the estimated grip.

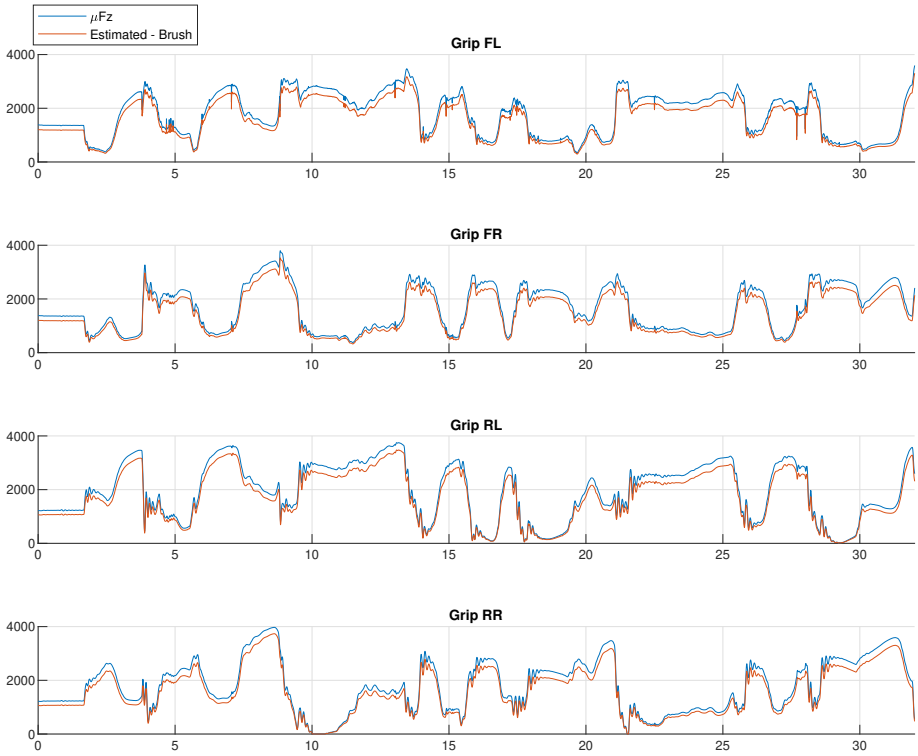

Figure 8.15: Estimated grip - Initial guess brush tyre model

As the estimation scheme reaches the data-set threshold, the online estimated grip is calculated with the latest available tyre model. The result of the online estimated grip after the estimation scheme has had some time to adjust is shown in Figure 8.16. A small improvement for lower grip conditions is visible, but the results are dominated by huge overestimation of grip for high tyre load conditions. This confirms that the estimation scheme failed to get the load-sensitivity parameters accurate. The initial estimate outperforms the online estimated grip for higher load scenarios.

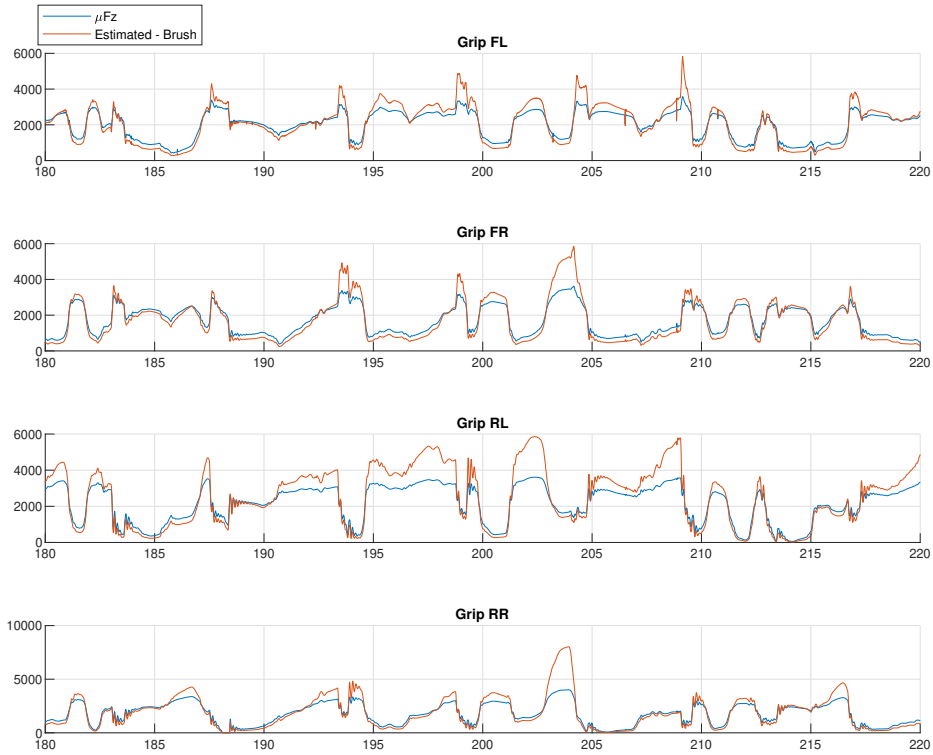

Figure 8.16: Estimated grip - Online estimated brush tyre model

8.5.3 Magic formula friction iteration

The nature of the magic formula, with the D parameter as a factor outside of the main sine function, allows for the assumption that all parameters besides the D parameter are unaffected by the tyre-road friction. The step-size for all parameters besides D_a and D_b were set to 0, and the initial guess for D_a and D_b was set to the final estimate from the straight line acceleration.

8.5.3.1 Convergence

The development of D_a and D_b over the course of the simulation is shown in Figure 8.17. As D_a decreases, the load sensitive parameter D_b increases. This is the main difference compared to the brush model development. Besides that, the overall behaviour of the magic formula model is very similar to that of the brush model. A lack of knowledge of tyre behaviour for high tyre loads means that the load sensitivity is estimated poorly and the effect of the lateral force using tyre capacity causes a lot of fluctuation, in the form of sharp steps, in the estimates as tyre forces for given bins vary over the course of the event.

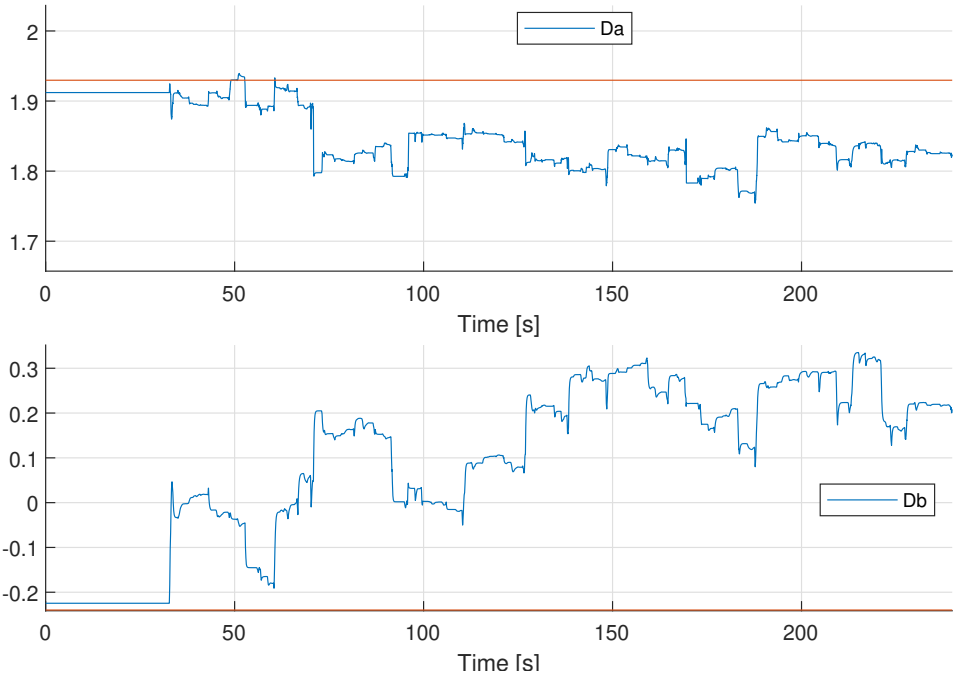

Figure 8.17: Parameter development for magic formula friction model parameters

8.5.4 Online friction estimate

Figure 8.18 shows the estimated grip using the initial estimate, and the grip is underestimated for all four tyres. Just like with the brush model, the increased grip on the track surface is clearly visible

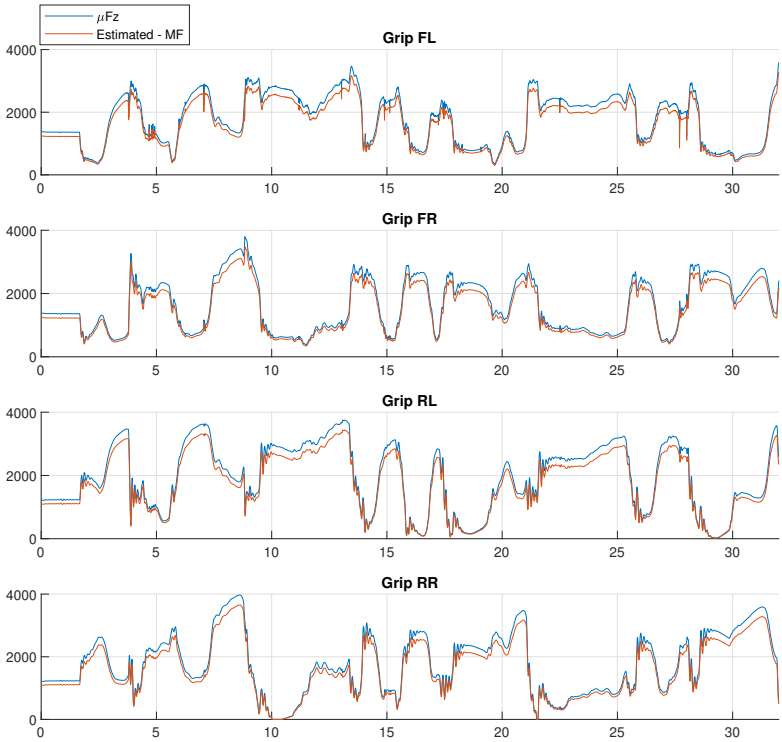

Figure 8.18: Estimated grip - Initial guess magic formula tyre model

As the estimation scheme reaches the data-set threshold, the friction parameters are updated online. The result of the same time-frame as shown for the brush model is presented in Figure 8.19. Here the online estimator has had time time adjust to the new track conditions. Just as for the brush model, we see an improvement for low grip conditions. The estimate for high grip conditions is hugely overestimated, caused by the inaccuracy of the load-sensitivity parameter.

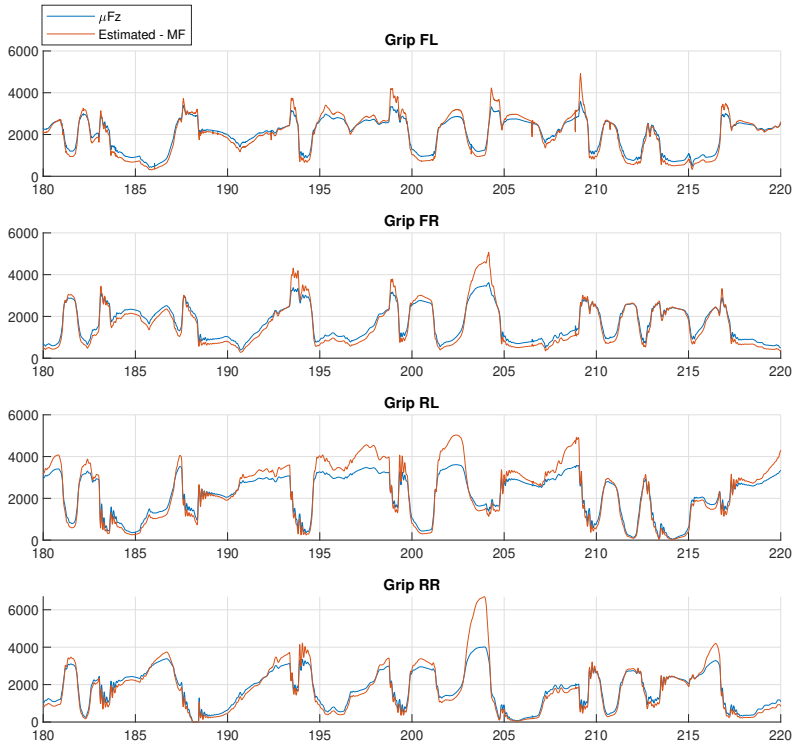

Figure 8.19: Estimated grip - Online estimated magic formula tyre model

8.5.5 Comparison of online estimated grip

The two approaches have achieved similar results. Both models failed to achieve converging parameters, even though the initial estimate only was off by 10%. Both results seemed to perform better for low tyre loads. Figure 8.20 shows the error in estimated grip against the tyre load. All four tyres are included. The error is defined in Equation 8.11, where a positive error is an overestimated grip.

$$\epsilon_{grip} = \hat{F}_{x_{max}} - F_{x_{max}} \tag{8.11}$$

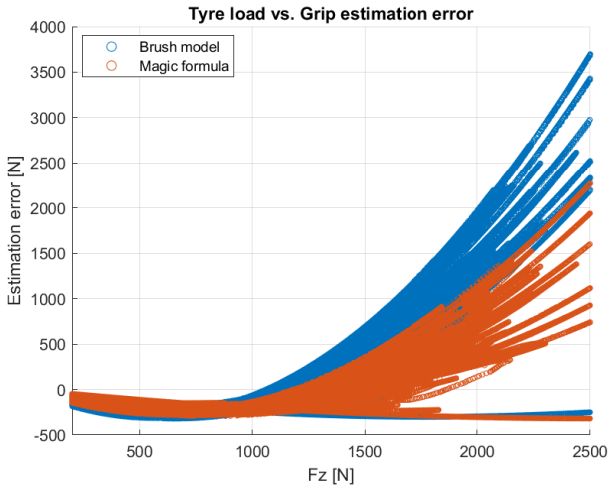

Figure 8.20: Grip estimate error vs. F_z

The results show that both estimators are performing a lot better for tyre loads up to $1000N$ than for higher tyre loads. The magic formula model slightly outperforms the brush model. Both models underestimate the available grip in this range, most likely due to neglecting the effects of slip angle in the friction model used for the reference. Figure 8.21 show the slip angles for the time period where the estimators have adjusted their parameters, showing the presence of a slip angle almost the entire period. This reduces the available grip.

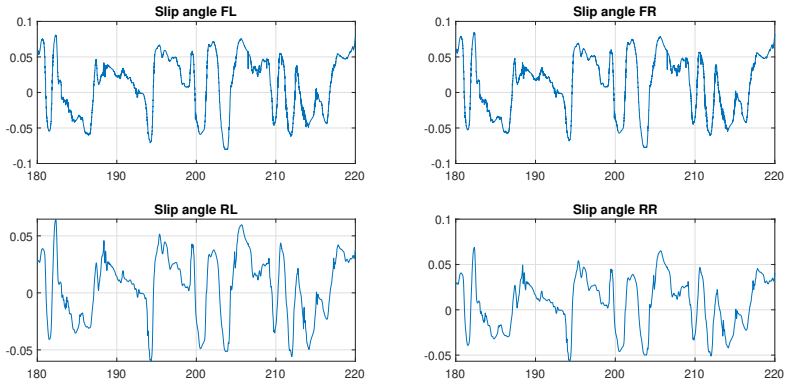

Figure 8.21: Slip angle for all tyres

One final aspect to take into consideration while looking at the online estimated grip is the maximum longitudinal tyre force that can be generated. As the only source of positive F_x

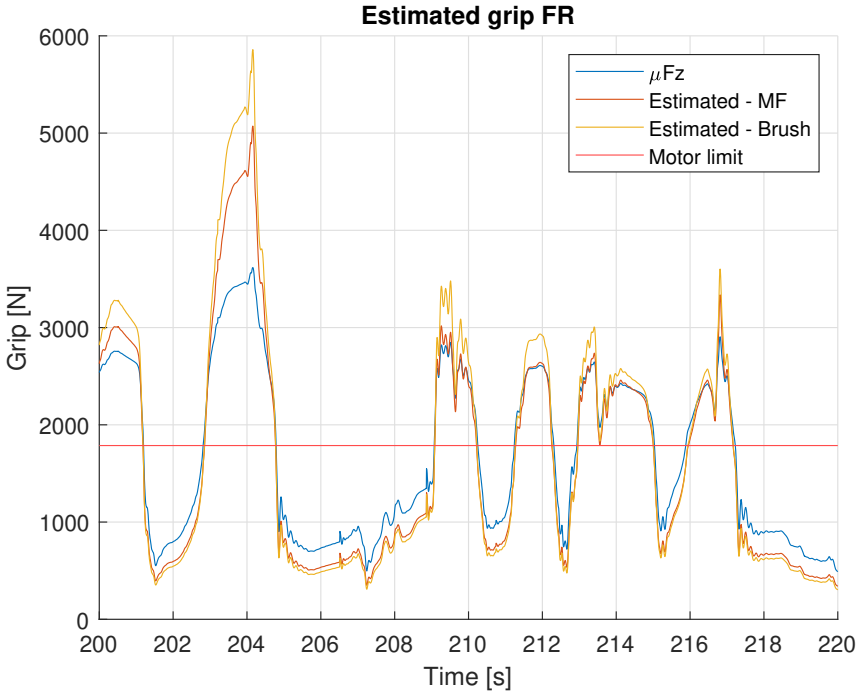

Figure 8.22: Estimated grip for front right tyre and motor limit

is the electric motor, it's output is the limiting factor. The maximum longitudinal force generated by the motor is given in Equation 8.12. As R_e varies during driving, $1800N$ is used as reference. As the friction of the road surface was increased for this experiment, less tyre load is required to handle the maximum motor output than when the initial guess was estimated.

$$F_{motor_{max}} = \frac{M_{motor_{max}} \cdot i_{gear}}{R_e} < 1800N \tag{8.12}$$

Figure 8.22 shows the motor limit together with the estimated grip for the front right tyre. Is is visible that the estimated grip is slightly underestimated when the tyre is the limiting factor, while the grip is overestimated when the motor is the limiting factor of the system. This also explains why there is no data available for high slip and high tyre loads, as the motor is not powerful enough to use all available grip.

8.6 Hardware-in-the-loop testing

The system developed in this thesis will be running on the 2021 Revolve NTNU racecar. In order to increase reliability, the system is tested on the target hardware before the vehicle

is tested on track.

8.6.1 CPU load

The primary concern regarding the target hardware is overloading the CPU core dedicated to the TV control system. Gradient calculation and the data selection algorithm requires a lot of floating point calculation, scaling with the data-set size gathered. Figure 8.23a shows the CPU load for an experiment with 1 datapoint per bin, and one with two datapoints. Until $t = 20$, the data selection threshold has not been reached yet, meaning that the gradient descent solver is not running yet. Until this point, both experiments require about 50% CPU load. As both experiments reach their data selection thresholds, the CPU usage increases. The gradient method with twice as many datapoints uses around 85% of the CPU capacity, while the smaller data-set experiment uses around 80%. Both solvers seem to have an upwards trend in CPU usage, even after the threshold is reached.

A longer experiment was conducted, where a data-set with a single datapoint per bin is used for the estimation. The CPU load for this simulation, together with the amount of datapoints gathered in the data-set is presented in Figure 8.23b. Again, the moment the gradient method is activated as the threshold is reached is clearly visible in the CPU load. As the size of the data-set keeps increasing, so does the CPU load. Once the data selection algorithm stops filling new bins, and only switches out old datapoints, the CPU load stabilizes as well.

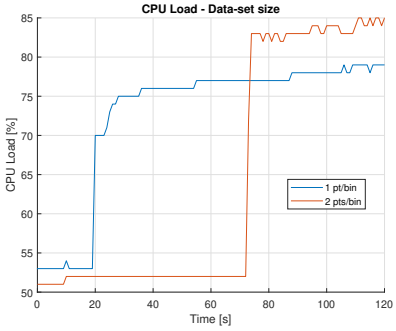

(a) CPU load for 1 and 2 datapoints per bin.

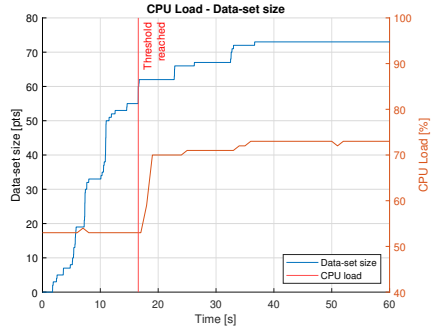

(b) CPU load before and after solver activation.

Figure 8.23: CPU loads for different scenarios

Chapter 9

Conclusion and Future work

9.1 Conclusion

Two goals were set out before the start of this thesis. The primary goal was to identify the friction coefficient between the tyre and road online. The secondary goal was to find a full longitudinal tyre model for the new Hoosier tyres, that Revolve NTNU is switching to this year.

In order to achieve the first goal, the complexity of the cost function was reduced by removing the race car dynamics, and using a Kalman filter for the tyre force estimation instead. The Kalman filter proved to be capable of estimating the longitudinal tyre forces accurately, despite no direct measurements of the tyre behaviour being available. The lateral forces were less accurate, as the estimates contained big spikes most likely caused by a lack of observability of these states.

The decreased complexity of the cost function, together with the developed online data selection algorithm to ensure excitation, increased the performance of the tyre friction estimation. For straight line acceleration events, both the brush and magic formula tyre model was able to identify the tyre-road friction coefficient. Simplifications in the brush model meant that it underestimated the friction coefficient by 5%, while the magic formula model was able to accurately estimate the friction coefficient for almost the entire tyre load range. Both models required approximately equal amounts of information about the system to converge, despite the magic formula containing twice as many parameters.

The results of the full circuit event, using the estimated θ from the straight line experiment as an initial guess showed that the simplification of using pure longitudinal tyre models causes the models to not converge. As the lateral forces generated by the slip angle reduce the longitudinal capacity of the tyre, F_x estimates for similar tyre load and slip can vary. This is not modeled, and the parameters therefor are unable to converge. This gives an inaccurate online estimate of the friction coefficient, underestimating the available grip in

situations where the tyre is the limiting factor.

The secondary goal of acquiring a full tyre model was achieved during the straight line acceleration experiment. As the models used in this thesis are pure longitudinal tyre model. Ensuring that enough model excitation is achieved is important, as the models can converge to false parameter values if not excited sufficiently. The models acquired in the simulation are shown in Figure 9.1.

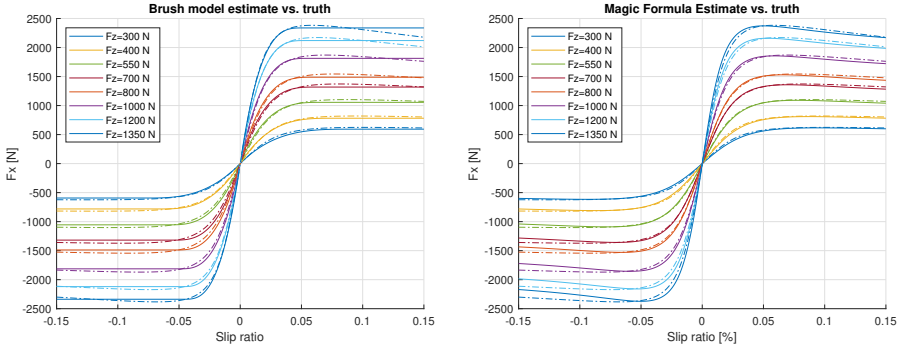

(a) Estimated brush tyre model

(b) Estimated magic formula tyre model from straight line accelerations

Figure 9.1: The estimated tyre models from straight line accelerations

9.2 Future work

There are both short term and long term continuations of the work performed in this thesis. The deployment of the system on the 2021 race car, and tuning and operating the system is the first step. After the season, post processing and improvement of the solver, estimation scheme and it's inputs should be prioritised by the next Revolve NTNU team.

9.2.1 Deploy system on race car

The results in this thesis were achieved in a simulation environment described in Chapter 6. The new Revolve NTNU race car, Luna, which is shown in Figure 9.2 is due to be completed before the end of June 2021. When the initial shakedown of Luna is completed, the system developed in this thesis will be activated. The design matrices $\boldsymbol{Q}$ and $\boldsymbol{R}$ will need to be tuned for the real life system. When the Kalman filter has been tuned sufficiently, the step-size for both online estimators will have to be tuned. After the tuning of the design parameters for the estimation scheme has been performed, the straight line acceleration experiment should be repeated in real life.

9.2.2 Post processing

Over the course of the 2021 summer, Luna will be tested extensively and used in competition. After the season, longitudinal tyre force estimates will be available for a wide

Figure 9.2: Render of the 2021 Revolve NTNU race car - Luna

range of car setups and track conditions. The estimated forces from the Kalman filter can therefor be used to fit a more complex tyre model offline. This model can then include car setup parameters like tyre pressure and inclination angle, for example with the use of the full Magic Formula 5.2 tyre model.

9.2.3 Improvement of online tyre parameter estimation scheme

The gradient descent method used in this thesis was chosen due to it's previous success from earlier works in Revolve NTNU, meaning that the used tyre models and system excitation were the limiting factor of the estimation scheme's success. The solver is not the most efficient, as a lot of data is processed at each time-step. To improve this, linearized recursive solvers should be investigated.

The results from the full circuit experiment showed that the pure longitudinal tyre models used in this thesis perform poorly when combined behaviour is present. Therefor, the next step for this estimation scheme is to upgrade the tyre models to a combined longitudinal/lateral tyre models. A good candidate for is the combined brush tyre model, derived in [3, Chapter 3]. This can improve both the online estimated grip, and increase the knowledge of tyre models in Revolve NTNU.

9.2.4 Improvement of estimator inputs

The input to the estimation scheme originates from the existing state estimation module developed in Revolve NTNU. Especially the estimated slip ratio and tyre loads should be improved, by looking into the use of the system dynamics instead of using raw measurements and definitions, for example through the use of an Extended Kalman Filter.

Bibliography

[1] E. Bakker, L. Nyborg, and H. B. Pacejka, "Tyre modelling for use in vehicle dynamics studies", in *SAE Technical Papers*, SAE International, Feb. 1987. DOI: 10.4271/870421. [Online]. Available: https://www.sae.org/publications/technical-papers/content/870421/.

[2] William F.Milliken and Douglas L. Milliken, *Race car vehicle dynamics*, 1994.

[3] H. B. Pacejka, *Tire and Vehicle Dynamics*. Elsevier Ltd, 2006, ISBN: 9780750669184. DOI: 10.1016/B978-0-7506-6918-4.X5000-X.

[4] J. Svendenius, "Tire Modeling and Friction Estimation", *Control*, 2007.

[5] T. I. Fossen, *Handbook of Marine Craft Hydrodynamics and Motion Control*, 1. Aufl. Hoboken: Wiley, 2011, ISBN: 1119991498.

[6] P. A. Ioannou and J. Sun, *Robust Adaptive Control*, ser. Dover Books on Electrical Engineering Series. Dover Publications, Incorporated, 2012, ISBN: 9780486498171. [Online]. Available: https://books.google.no/books?id=pXWFY%5C_vbg1MC.

[7] C.-T. Chen, *Linear system theory and design*, New York, 2013.

[8] M. Choi, J. J. Oh, and S. B. Choi, "Linearized Recursive Least Squares Methods for Real-Time Identification of Tire-Road Friction Coefficient", *IEEE Transactions on Vehicular Technology*, vol. 62, no. 7, pp. 2906–2918, 2013, ISSN: 00189545. DOI: 10.1109/TVT.2013.2260190.

[9] P. Morin, A. Eudes, and G. Scandaroli, "Uniform observability of linear time-varying systems and application to robotics problems", vol. 10589 LNCS, Springer Verlag, 2017, pp. 336–344, ISBN: 9783319684444. DOI: 10.1007/978-3-319-68445-1{_}39.

[10] Sondre Naess Midtskogen, "Trajectory Following for Formula Student Driverless Vehicle", Tech. Rep., 2018. [Online]. Available: https://ntnuopen.ntnu.no/ntnu-xmlui/handle/11250/2616059.

[11] D. Harsh and B. Shyrokau, "Tire model with temperature effects for formula SAE vehicle", *Applied Sciences (Switzerland)*, vol. 9, no. 24, Dec. 2019, ISSN: 20763417. DOI: 10.3390/app9245328. [Online]. Available: https://doi.org/10.3390/app9245328.

[12] L. van der Lee, "Online Tyre Parameter Estimation for a 4WD Formula Student Racecar", 2020.

[13] A. Albinsson, *THESIS FOR THE DEGREE OF DOCTOR OF PHILOSOPHY Online and Offline Identification of Tyre Model Parameters*, ISBN: 9789175977201. [Online]. Available: https://commons.wikimedia.org/wiki/File:Ice_on_Tire.jpg.

[14] *Enclustra FPGA Solutions — Mercury ZX5 — Xiliny Zynq 7000 All Programmable System-on-Chip (SoC) Module — System-on-Module (SOM) — XC7Z015 — XC7Z030*. [Online]. Available: https://www.enclustra.com/en/products/system-on-chip-modules/mercury-zx5/.

[15] *Estimate states of discrete-time or continuous-time linear system - Simulink - MathWorks Nordic*. [Online]. Available: https://se.mathworks.com/help/control/ref/kalmanfilter.html.

[16] *FSG: Rules & Important Documents*. [Online]. Available: https://www.formulastudent.de/fsg/rules/.

[17] *Handle transfer of data between blocks operating at different rates - Simulink - MathWorks Nordic*. [Online]. Available: https://se.mathworks.com/help/simulink/slref/ratetransition.html.

[18] *ISO - ISO 8855:2011 - Road vehicles — Vehicle dynamics and road-holding ability — Vocabulary*. [Online]. Available: https://www.iso.org/standard/51180.html.

[19] J. Jiang, F. Yu, H. Lan, and Q. Dong, "Instantaneous Observability of Tightly Coupled SINS/GPS during Maneuvers", DOI: 10.3390/s16060765. [Online]. Available: www.mdpi.com/journal/sensors.

[20] J. Nocedal and S. J. Wright, "Numerical Optimization Second Edition 4:1 Springer", Tech. Rep.

[21] *Symbolic Math Toolbox - MATLAB*. [Online]. Available: https://se.mathworks.com/products/symbolic.html.

Appendices

Appendix A

Magic Formula 5.2 Equations

Normalized normal load increment:

$$\mathrm{df_z} = \frac{\mathrm{F_z} - \mathrm{F'_{z0}}}{\mathrm{F'_{z0}}} \tag{A.1}$$

$$\mathrm{F'_{z0}} = \mathrm{F_{z0}} \cdot \lambda_{\mathrm{F}z0} \tag{A.2}$$

A.1 Pure lateral

A.1.1 Base Magic Formula

$$\mathrm{F_y} = \mathrm{F_{y0}}\left(\alpha, \gamma, \mathrm{F_z}\right) \tag{A.3}$$

$$\mathrm{F_{y0}} = \mathrm{D_y} \sin\left[\mathrm{C_y} \arctan\left\{\mathrm{B_y}\alpha_\mathrm{y} - \mathrm{E_y}\left(\mathrm{B_y}\alpha_\mathrm{y} - \arctan\left(\mathrm{B_y}\alpha_\mathrm{y}\right)\right)\right\}\right] + \mathrm{S_{Vy}} \tag{A.4}$$

$$\alpha_\mathrm{y} = \alpha + \mathrm{S_{Hy}} \tag{A.5}$$

$$\gamma_\mathrm{y} = \gamma \cdot \lambda_{\gamma\mathrm{y}} \tag{A.6}$$

A.1.2 Coefficients

$$\mathrm{B_y} = \frac{\mathrm{K_y}}{\left(\mathrm{C_y}\mathrm{D_y}\right)} \tag{A.7}$$

$$\mathrm{C_y} = \mathrm{p_{Cy1}} \cdot \lambda_{\mathrm{Cy}} \tag{A.8}$$

$$\mathrm{D_y} = \mu_\mathrm{y} \cdot \mathrm{F_z} \tag{A.9}$$

$$\mathrm{E_y} = \left(\mathrm{p_{Ey1}} + \mathrm{p_{Ey2}}\ \mathrm{df_z}\right) \cdot \left\{1 - \left(\mathrm{p_{Ey3}} + \mathrm{p_{Ey4}}\gamma_\mathrm{y}\right) \operatorname{sgn}\left(\alpha_\mathrm{y}\right)\right\} \cdot \lambda_{\mathrm{Ey}}(\leq 1) \tag{A.10}$$

$$\mathrm{S_{Hy}} = \left(\mathrm{P_{Hy1}} + \mathrm{P_{Hy2}}\mathrm{df_z}\right) \cdot \lambda_{\mathrm{Hy}} + \mathrm{P_{Hy3}}\gamma_\mathrm{y} \tag{A.11}$$

$$\mathrm{S_{Vy}} = \mathrm{F_z} \cdot \left\{\left(\mathrm{p_{Vy1}} + \mathrm{p_{Vy2}}\ \mathrm{df_z}\right) \cdot \lambda_{\mathrm{Vy}} + \left(\mathrm{p_{Vy3}} + \mathrm{p_{vy4}} \cdot \mathrm{df_z}\right) \cdot \gamma_\mathrm{y}\right\} \cdot \lambda_{\mu\mathrm{y}} \tag{A.12}$$

$$K_y = p_{Ky1}\, F_{z0} \sin\left[2 \arctan\left\{F_z / \left(p_{ky2}\, F_{z0} \lambda_{F_{20}}\right)\right\}\right] \cdot \left(1 - p_{Ky3}\, |\gamma_y|\right) \cdot \lambda_{F_{20}} \cdot \lambda_{Ky} \tag{A.13}$$

$$\mu_y = \left(p_{Dy1} + p_{Dy2} df_z\right) \cdot \left(1 - p_{Dy3} \gamma_y^2\right) \cdot \lambda_{\mu y} \tag{A.14}$$

A.2 Pure longitudinal

A.2.1 Base Magic Formula

$$F_x = F_{x0}\left(\kappa, F_z\right) \tag{A.15}$$

$$F_{x0} = D_x \sin\left[C_x \arctan\left\{B_x \kappa_x - E_x \left(B_x \kappa_x - \arctan\left(B_x \kappa_x\right)\right)\right\}\right] + S_{Vx} \tag{A.16}$$

$$\kappa_x = \kappa + S_{Hx} \tag{A.17}$$

$$\gamma_x = \gamma \cdot \lambda_{\gamma x} \tag{A.18}$$

A.2.2 Coefficients

$$B_x = \frac{K_x}{\left(C_x D_x\right)} \tag{A.19}$$

$$C_x = p_{Cx1} \cdot \lambda_{Cx} \tag{A.20}$$

$$D_x = \mu_x \cdot F_z \tag{A.21}$$

$$E_x = \left(p_{Ex1} + p_{Ex2} df_z + p_{Ex3} df_z^2\right) \cdot \left\{1 - p_{Ex4}\, \mathrm{sgn}\left(k_x\right)\right\} \cdot \lambda_{Ex}(\leq 1)\Big) \tag{A.22}$$

$$S_{Hx} = \left(p_{Hx1} + p_{Hx2} \cdot df_z\right) \lambda_{Hx} \tag{A.23}$$

$$S_{Vx} = F_z \cdot \left(p_{Vx1} + p_{Vx2} df_z\right) \cdot \lambda_{Vx} \cdot \lambda_{\mu x} \tag{A.24}$$

$$K_x = F_z \cdot \left(p_{Kx1} + p_{Kx2} df_2\right) \cdot \exp\left(p_{Kx3} df_2\right) \cdot \lambda_{Kx} \tag{A.25}$$

$$\mu_x = \left(p_{Dx1} + p_{Dx2} df_z\right) \cdot \left(1 - p_{Dx3} \cdot \gamma_x^2\right) \lambda_{\mu x} \tag{A.26}$$

Lars C. M. van der Lee

Online Tyre Parameter Estimation for a 4WD Formula Student Racecar

NTNU
Norwegian University of
Science and Technology

NTNU
revolve